OH AS AN ALTERNATE TRACER FOR MOLECULAR GAS: A STUDY IN THE W5 STAR-FORMING REGION

by

Philip David Engelke

A dissertation submitted to The Johns Hopkins University in conformity with the requirements for the degree of Doctor of Philosophy.

Baltimore, Maryland

July, 2019

Abstract

Tracing molecular H_2 gas in the Galactic interstellar medium is complicated by the fact that diffuse, cold H_2 is not detectable. The usual tracer for molecular gas is ^{12}CO(1-0); however, questions have been posed about the universality of CO for this purpose, and evidence has suggested reservoirs of undetected "CO-dark" molecular gas. This dissertation contributes to research into the use of OH 18 cm lines as an alternate tracer for molecular gas. The focus of this dissertation is a survey of the W5 star-forming region using the Green Bank Telescope to determine the structure and quantity of molecular gas in W5, and to compare the properties of W5 to those of a quiescent region according to both tracers. Calculating column densities of OH requires knowledge of the excitation temperature of the observed molecular transition. I have measured excitation temperatures of the OH 18 cm lines in W5 using two distinct methods: the traditional "expected profile" method, and a "continuum background method." The latter yields more precise results, and demonstrates that the excitation temperature is different for the two 18 cm main lines. Results of the OH survey in W5 are then presented. In W5, the OH and CO trace a similar mor-

ABSTRACT

phology of molecular gas, in contrast to quiescent regions which can contain CO-dark OH detections. The molecular gas mass traced by OH emission is slightly larger than that traced by CO, but the difference is not considered significant. I propose a volume density-based explanation for the presence or absence of CO-dark molecular gas, and estimate the average volume density for three regions using a diffuse cloud model. The CO-dark gas correlates with lower volume density portions of the quiescent region, and the highest average volume density occurs in W5. These results suggest that CO-dark molecular gas primarily exists in interstellar space outside of star-forming regions, and that volume density is the primary distinction between the molecular gas in W5 and the quiescent region. I also discuss a novel method based on excitation temperatures for estimating physical conditions in molecular gas without relying on CO.

Primary Reader: Ronald J. Allen

Secondary Reader: Colin A. Norman

Acknowledgments

I would like to thank my advisor Ron Allen for his steady guidance throughout this project. He has been an excellent mentor for me in my research and in my development as a scientist while in graduate school.

I am thankful to David Neufeld and Colin Norman, with whom I have had helpful and insightful discussions about my work.

I am grateful for the Grote Reber Fellowship program at the National Radio Astronomy Observatory for their funding and exposure to the field of radio astronomy, and especially to W. Miller Goss, who served as my sponsor and local advisor during my two-year stay in New Mexico for the Reber Fellowship. With expertise on the subject of OH 18-cm observations and VLA observations, he provided advice and assistance in this projectand his comments also helped improve my papers.

I am grateful to David E. Hogg, a collaborator and coauthor on much of our research program, for his contributions to the overall project as well as many discussions, especially regarding the details of GBT observing and data reduction. I also thank the staff at the Green Bank Observatory for their advice and assistance with

the operation of the GBT, and for the development and support of the GBTIDL data analysis software.

The staff at the VLA, especially Heidi and Drew Medlin, and Claire Murray, a former University of Wisconsin graduate student who worked with Miller Goss, were also helpful in providing assistance with VLA observating strategy and set-up.

The National Radio Astronomy Observatory is a facility of the National Science Foundation operated under cooperative agreement by Associated Universities, Inc. The Green Bank Observatory is a facility of the National Science Foundation operated under cooperative agreement by Associated Universities, Inc. The work reported here has been partially supported by the Director's Research Funds at the Space Telescope Science Institute. Support for this work was also provided by the NSF through the Grote Reber Fellowship Program administered by Associated Universities, Inc./National Radio Astronomy Observatory. The research presented in this work has used data from the Canadian Galactic Plane Survey, a Canadian project with international partners, supported by the Natural Sciences and Engineering Research Council of Canada. This research has benefited from the SAOImage software provided by the Harvard-Smithsonian Center for Astrophysics.

Dedication

To my family, whom I love very much.

Contents

CONTENTS

List of Tables

List of Figures

Chapter 1

Introduction

1.1 Background

The Milky Way Galaxy is the home to our Solar system, and yet the details of its structure and composition remain mysterious to some extent. Our location within the plane of the Galaxy makes it more difficult to observe the structure as a result of being inside of it; dust clouds obscure optical views towards the Galactic center, and the spiral structure must be discerned based on observations of kinematics as well as more precisely by parallax measurements towards masers and other such sources in the arms in order to estimate the distances to different features and piece together a picture of the Galaxy from within. In addition, our knowledge of the structure and composition of the Galaxy is limited to the sources that astronomers are able to observe directly. This inherent limitation produces a kind of self-selection in as-

tronomical study. Astronomers who observe the Galaxy for atomic hydrogen will find the structure of atomic hydrogen; astronomers who observe for CO will find the structure according to where CO signals are strong. Radio astronomy provides an excellent tool to study Galactic structure because it allows observers to look through the obscuring dust clouds that greatly limit optical observations, and allows study of certain key tracers of Galactic structure such as the famous 21 cm line for atomic hydrogen, as well as certain molecular tracers. Even so, the danger arises of becoming too attached to a particular method of tracing Galactic structure; focusing on observing with particular tracers reduces the richness of possible discoveries by placing familiar limits on what is possible to learn.

Keeping this idea in mind, we realize that modern astronomy reveals surprisingly little about the true nature of the Galaxy. On a grand scale, Galactic rotation curves suggest the presence of dark matter, or alternatively the possibility of new aspects to physics. The question as to what is the nature of the true explanation behind the flat Galactic rotation curves, and if it is dark matter, what that may be, remains one of the greatest mysteries in science today. On a less grandiose scale, even the baryonic mass component of the Galaxy, the part made out of "regular" materials that we ought to be able to understand, has ample room for new discovery. The aim of this dissertation is to contribute to a fresh study of the of the Galactic interstellar medium, using OH 18 cm lines as an alternate tracer for interstellar molecular gas as opposed to the usual ^{12}CO(1-0) tracer, with the possibility of shedding light on

the concept of "CO-dark" gas as well. This dissertation brings the techniques of OH 18 cm radio astronomy to the Westerhout 5 nebula, in order to expand this research program into the study of star-forming regions.

1.2 History

The hydroxyl radical OH was the first molecule to be detected in the Galactic interstellar medium (ISM) using radio astronomy, and the second major astronomical radio transition observed after the 21 cm line of atomic hydrogen. Although the primary component of molecular gas in the interstellar medium is molecular hydrogen, these molecules are not generally detectable in the conditions of the cold, diffuse interstellar medium (see Section 1.3 for an explanation of the physics). As such, other molecules mixed in in smaller abundances are needed as surrogates for the observation of molecular gas in the interstellar medium. OH was in fact one of the molecular radio lines that Charles Townes suggested might be detectable in space in 1957 when radio astronomy was just beginning (Townes 1957).

Weinreb et al. (1963) made the first OH 18-cm detection against Cassiopeia A in 1963 using the Millstone Hill Observatory in Westford, Massachusetts, operated by MIT Lincoln Laboratory. Shortly thereafter, Weaver et al. (1965) discovered an unexpectedly strong emission line at 1665 MHz while observing at the OH 18-cm frequencies towards HII regions. This strong emission line occurred in addition

to the expected OH absorption at 1665 MHz and 1667 MHz in W3. The authors labeled this surprise emission line "mysterium" until subsequent work determined that it consisted of OH maser emission (McGee et al. 1965). Though unexpected and not properly identified at first, this observation was the first detection of OH 18-cm emission in the interstellar medium. A few years later, Heiles (1968) also detected OH emission from high density interstellar dust clouds.

OH 18-cm absorption surveys were pioneered by Goss (1968a). These types of absorption surveys helped build an understanding of the distribution of interstellar OH, but contained the inherent limitation that absorption lines only occur in front of sources of sufficiently elevated background continuum. Early attempts at blind surveys for OH emission were not successful (e.g. Knapp & Kerr 1972; Penzias 1964). The general consensus began to emerge that non-anomalous OH emission was only detectable in high density, high dust content areas (Heiles 1968). This view was a natural result of the sensitivity limitations of radio astronomy at the time. Dickey et al. (1981) mentioned the possibility of widespread diffuse OH emission, but significant thought and study were not placed in this idea at the time, and in any case an observing program to search for widespread diffuse emission was not considered feasible.

Instead, OH 18 cm studies came to focus primarily on masers and anomalous excitation (e.g. Crutcher 1973; Dickey et al. 1981; Guibert et al. 1978; Nguyen-Q-Rieu et al. 1976; Turner 1973; Turner & Heiles 1971). The observations in these

studies were cases in which the OH 18 cm transition proved strong and useful, and allowed the study of the conditions and mechanisms of interstellar masers as well as precise parallax distance measurements to maser sources (Elitzur 1992; Reid & Moran 1981, for reviews, see).

In 1970, Wilson et al. (1970) of Bell Laboratories detected ^{12}CO(1-0) emission in the BN/KL region of the Orion nebula using the 36-foot antenna at Kitt Peak, Arizona. This observation was a turning point for the study of molecular gas in space, as ^{12}CO(1-0) emission was a strong, easily observable signal and became the molecular gas tracer of choice for the general interstellar medium. Since ^{12}CO(1-0) is generally an optically thick emission line, direct measurement of column densities from the signal strength and radiative transfer equations is not possible. The solution for CO was the "X-factor" method, in which a multiplicative factor, called the X-factor, is determined based on virial theorem arguments so that a ^{12}CO(1-0) signal strength may be converted into an estimate for total molecular gas column density (see Bolatto et al. 2013, for a review).

The many CO observational studies spurred by the Wilson et al. (1970) observation demonstrated that molecular gas was far more widespread in the interstellar medium than had been accepted up to that point, revealed large clouds of gas such as giant molecular clouds, and paved the way for new areas of astrophysics focusing on molecular gas and the processes that take place in star-forming regions and photo-dissociation regions. CO observations in external galaxies also brought about

the study of molecular gas outside of our own Galaxy for the first time (Rickard et al. 1975). CO studies led to the impression that molecular gas is located mainly in clumps and cloud structures, primarily near the Galactic plane, although some of these clouds can be massive (e.g. Scoville et al. 1974). Survey work during the 1980s and 1990s attempted to map the molecular gas content of the Galaxy, using CO as a surrogate tracer for the primary component of molecular gas, H_2 (e.g. Clemens et al. 1988; Dame et al. 2001, 1987; Heyer et al. 1998; Sanders et al. 1984).

Around the late 1970s and 1980s, radio receiver technology improved so that non-anomalous OH emission could perhaps be detected in the general ISM. An early OH survey was performed by Turner (1979). However, although the sensitivity of the Turner (1979) survey allowed detection of OH emission, the sensitivity was insufficient to detect widespread OH emission from lower density, diffuse gas. During the following years, if faint OH emission appeared unexpectedly in observations, people generally ignored it or fitted it out of baselines during data reduction and analysis. Although Dickey et al. (1981) suggested the possibility of an OH emission survey as early as 1981, Liszt & Lucas (1996) were pioneers in the newly feasible quantitative study of non-anomalous OH emission, which they observed using the NRAO 43-m telescope at Green Bank, West Virginia. These observations were targeted near continuum sources, and were taken along with OH absorption data in front of those sources. One of the goals of this work was to measure the excitation temperature of the OH lines, and despite subsequent work (Liszt and Lucas 2000), OH emission was not to

be treated as a widespread tracer for molecular gas, while CO(1-0) continued to be the standard for the field.

Questions have arisen, however, as to the universality of CO as a molecular gas tracer. An early hint that molecular gas could exist beyond the known reservoirs traced by CO was the 1986 finding of an offset between the dust lanes and atomic and ionized hydrogen content in an arm of M83 (Allen et al. 1986), which could be interpreted as indication of the presence of additional undetected molecular gas. A new mystery arose in 2005, with the announcement by Grenier et al. (2005) that unexplained excess of gamma rays as well as IR evidence of dust from vast swaths of the Galaxy indicated the presence of large amounts of "dark gas." This dark gas was as yet unidentified, and was not detected directly in any observations or surveys. In this case, the word "dark" is unrelated to the concept of non-baryonic dark matter, and was merely an indication that the gas itself had not been observed and its nature and composition was not unknown. The theory suggested was that the dark gas was undetected molecular hydrogen in the diffuse interstellar medium. Cosmic ray interactions with hydrogen nuclei could produce gamma-rays of the range of energies observed, and dust clouds producing the observed infrared signal are typically associated with molecular gas clouds. Knowing that molecular hydrogen in the cold, diffuse ISM is typically undetectable, and that hydrogen nuclei were most likely present in the mystery gas, the conclusion that the dark gas was likely to be undetected molecular gas was natural. The key difference from other clouds of molecular

gas in the ISM was that in this case, there was no ^{12}CO(1-0) signal associated with the gas. This led to the concept of "CO-dark molecular gas," which over the next several years became accepted by astrophysicists as a component of the interstellar medium. However, several problems remained. Firstly, the CO-dark molecular gas was only a hypothesis; a second molecular tracer would be needed to confirm that molecular gas was in fact present in these regions. Secondly, a molecular emission or absorption line would be essential for determining the kinematics of this gas, which would help locate where in the Galactic spiral structure this probable molecular gas was hiding. For these reasons, a molecular gas tracer alternative to CO was needed, although which molecular tracer would be ideal to use was not clear. Observations in formaldehyde and C^+ were among some of the early attempts to confirm and trace the CO-dark gas, but were not generally successful.

In 2005, Allen and collaborators found OH emission while working on a high sensitivity observational study of the large dust cloud Lynds 1204 using the 20 m telescope at the Onsala Space Observatory in Sweden (Rodríguez et al. 2007). OH observations indicated widespread faint emission near but outside of the dust cloud target. In order to find a region of sky free of OH to use as the "off" target observations to compare to the on target observations for baseline subtraction, the telescope was moved to a new coordinate farther from the dust cloud. However, faint OH emission was still present, and subsequent moves of the telescope to search for an empty area of the sky continued to reveal low level OH emission. Although the attempt at

finding an OH-free area to use as an "off" position for the original target failed, these observations revealed something perhaps more interesting: that faint OH emission was much more widespread than anybody had expected, and the observations became a serendipitous miniature OH emission survey. These results were published in Allen et al. (2012, 2013). In addition to demonstrating that OH emission is widespread in the Galactic ISM and can be detected in a blind survey, the Allen et al. (2012, 2013) data showed something else: when compared to the ^{12}CO(1-0) data from existing surveys, the majority of the OH detections did not have any corresponding features in the CO data!

A new lead was thus uncovered in the search for an alternate molecular gas tracer to study the CO-dark gas. In observations with sufficient sensitivity, the OH main lines at 1667 MHz and 1665 MHz appeared to be detectable in the cold, diffuse ISM, the detections were widespread, and they appeared to trace a larger component of the molecular ISM than did ^{12}CO(1-0). The Allen et al. (2012, 2013) results were, however, limited to the solar neighborhood by radio frequency interference. Meanwhile, the SPLASH survey of the OH 18 cm lines (Dawson et al. 2014), using the 64 m telescope near Parkes, Australia, focused on OH in the Southern hemisphere. This survey primarily covered regions of the Galactic plane near the Galactic center, causing the majority of OH detections to be absorption lines. Column densities would therefore be highly dependent on knowledge of the excitation temperatures as well as the ambient continuum radiation field when using the radiative transfer equations,

and the kinematic distance ambiguity inherent to observations towards the inner part of the Galaxy made the locations of OH detections and the relevant continuum temperature values more difficult to obtain. However, this survey did provide further evidence of the widespread nature of OH detections in the Galactic ISM.

We began the research program of which this thesis is a portion in 2013, inspired by the Allen et al. (2012, 2013) results. We chose to use the 100 m telescope in Green Bank, West Virginia with a cryogenic receiver in order to obtain high sensitivity OH observations in a blind survey towards a portion of the outer Galaxy, with limited radio frequency interference owing to the telescope's location in the National Radio Quiet Zone. The results of the survey were published in Allen et al. (2015), and demonstrated that OH 18 cm emission can trace the molecular components of Galactic arm structure, is widespread, and traces molecular gas in many locations where no CO(1-0) signal is present in the CfA survey data (Dame et al. 2001). In subsequent observation work with the Green Bank Telescope, we have performed a denser grid survey (Busch et al. 2019) and compared to the FCRAO CO survey data (Heyer et al. 1998), detected various Galactic arms, rolling motions of the Perseus Arm, and even hints of the possibility of low level diffuse OH emission between the Galactic arms, although work is still needed to support and confirm this last result. This thesis focuses on the study of OH as an alternate tracer for molecular gas in the W5 star-forming region, and includes the work of two published papers and two shorter papers to be submitted for publication. Chapters 2 and 3 are composed of

the published papers, and Chapters 4 and 5 contain text that is being prepared for publication. The remainder of the introduction will describe some of the physics involved in understanding the OH 18-cm lines and how these properties apply to the project of tracing molecular gas in the cold, diffuse interstellar medium.

1.3 Physics of H_2, CO, and OH Transitions

We now wish to understand the origin and physics behind the molecular radio signals on which this work depends. All of the molecules that we discuss are diatomic; this includes H_2, CO, and OH. At the low temperatures found in most molecular cloud regions, rotational energy levels are the only relevant energy levels to consider; electronic and vibrational energy levels are too high in energy to be often excited. In order to understand the rotational energy levels of a diatomic molecule, we will start with the simplified model of the rigid rotor. For a diatomic molecule with reduced mass μ and a separation between the two nuclei of R, the moment of inertia $I = \mu R^2$. Classically, the angular momentum of the system would be $I\omega$ where ω is the rate of rotation of the system. Using the old quantum theory approach, we then apply the postulate that angular momentum must be quantized, that is, only values of angular momentum that are integer multiples of $\hbar$ are allowed. Thus we have

$$I\omega = J\hbar \tag{1.1}$$

where J can be any positive integer. Solving for allowed rotational rates gives

$$\omega = \frac{J\hbar}{I} \tag{1.2}$$

which we can enter into the formula for rotational kinetic energy, yielding

$$E = \frac{1}{2}I\omega^2 = \frac{\hbar^2}{2I}J^2. \tag{1.3}$$

This result using the old quantum theory is helpful as a start, but it begins to break down for lower values of J. A better approximation of the rotational energy levels of a diatomic molecule can be obtained by applying Schrödinger wave mechanics to the rigid rotor model. The result is that

$$E = \frac{\hbar^2}{2I}J(J+1). \tag{1.4}$$

Unfortunately, detecting H_2 gas is not as simple as observing transitions between the ground state and first excited rotational state of H_2 molecules in space. The probability of a transition occurring between energy levels for a diatomic molecule is, to first order, related to the electric dipole moment of the molecule (see Herzberg 1950, for a thorough description of the physics). A symmetric diatomic molecule such

as H_2 has zero electric dipole moment, which means that the first order contribution to the Einstein A coefficients for its rotational transitions will be zero. There are also smaller contributions to the Einstein A coefficients that depend on the magnetic dipole moment and the electric quadrupole moment of the molecule, and these need not be zero for a symmetric diatomic molecule. In the case of H_2, quadrupole transitions do occur, but transitions between rotational energy levels of H_2 happen only over large time scales and thus generally do not produce observable radiation signals. The Einstein A coefficients are larger for higher frequency transitions. Energy spacing between rotational levels increases linearly with J, meaning that transitions from higher energy levels will produce stronger emission signals. Moreover, an especially high column density of H_2 will help increase the strength of an emission signal. Such H_2 emission has in fact been observed, but the reliance on high energy levels and high column densities inherently limits the utility of these observations for surveys of H_2 in the interstellar medium. The majority of molecular clouds are too low in kinetic temperature to allow direct observation of H_2.

Although H_2 is the most abundant molecule in molecular clouds, other molecules are found in these regions as well. Observing these less abundant molecules is in fact easier than directly observing H_2, and information about the total size and density of clouds can still be obtained from the details of the emission lines from these molecules. CO is an asymmetrical diatomic molecule, and as such it has a nonzero electric dipole moment. Therefore, the Einstein A coefficients for low energy rotational level

transitions are reasonably strong, and the transition from the first excited rotational level to the ground state in ^{12}CO, known as the ^{12}CO(1-0) transition, has become the most commonly used tracer for molecular gas. Despite its near-universal acceptance, there are some problems with using only CO as a molecular gas tracer.

A transition has a certain timescale associated with the amount of time it takes for an excited energy level to decay back down, and emitting a photon. This timescale for spontaneous emission is the inverse of the Einstein A coefficient. If the molecules are collisionally excited to the higher energy levels needed for the transition back down to later occur, then it follows that depending on the density of gas molecules in the cloud, there could be either enough collisions that the rate going up to excited energy levels exceeds the rate of decay, or there could be few enough collisions that the rate of decay exceeds the rate of excitation. Also noteworthy, is that stimulated emission can dominate over spontaneous emission at radio frequencies, even though it is negligible at optical frequencies. This occurs because the probability of spontaneous emission depends on ν^3, and frequency ν is much lower for the radio part of the spectrum (Wilson et al. 2013).

The density at which the collisional excitation rate equals the spontaneous emission rate, which is given by the Einstein A coefficient, is called the critical density n_{crit}. We find the collisional excitation rate from the product of the collisional cross

section σ, the velocity v, and the density n, using the following equation:

$$n_{crit} = \frac{A_{ul}}{< \sigma v >} \tag{1.5}$$

(Wilson et al. 2013). What happens to molecular transitions for densities above and below the critical density depend on the equation for emissivity (see Wilson et al. 2013). We can look at the emissivity dependence above and below the critical density as two different regimes, although the shift is continuous and falls somewhere in between for densities near the critical density. If the density is well above the critical density, the emissivity reaches a stable value. This is the larger value of the emissivity that the gas approaches as the density is elevated above the critical density.

If the density is well below the critical density, the emissivity depends on the radiation field because collisions are not important. This emissivity limit is smaller than the emissivity limit above the critical density, meaning that although emission lines can still be observed from gas below the critical density, the resulting emission will be much weaker. Above the critical density, signal strengths are reliably stronger. Thus the values of the critical densities for different gases allow comparisons to be made as to what gases are more or less likely to be detectable at lower densities. For the ^{12}CO(1-0) transition, the critical density is approximately 10^3 cm^{-3}. The OH radio transitions, by comparison, have critical densities near 1 cm^{-3}. Therefore, it is conceivable that although the ^{12}CO(1-0) transition is generally stronger than the

OH 18 cm transition, there may be densities well below the CO critical density of 1000 cm^{-3} for which CO is not detected or produces a weak signal implying lower quantities of CO than are truly present. OH, on the other hand, could still produce a signal of full strength until the density is reduced to the much lower value of 1 cm^{-3}. Comparing these two critical densities, OH appears likely to be a preferable tracer for lower density gas. As a result, it seems theoretically plausible that OH in some cases could trace regions and quantities of molecular gas that are not detected in CO emission. This prediction appears to be consistent with observational results by Allen et al. (2015), which found that some molecular features were traced by both CO and OH, whereas others were traced by OH even though they were not detected in CO.

There is another complication involving ^{12}CO(1-0) emission, which is that the ^{12}CO(1-0) line is optically thick. This means that any observed ^{12}CO(1-0) signal is only showing the outer layer of the cloud on the side first reached by the line if sight. Any three-dimensional structure along the line of sight into the cloud is undetectable. This poses a fundamental limitation to CO observations: the angular size of a cloud in the sky can be determined, but its three-dimensional total size cannot be determined. Thus one can only estimate the total mass of molecular gas in the cloud. OH is not optically thick, so a more direct measurement can be made of the three-dimensional total size of a molecular cloud and of its mass.

The optical thickness of the CO line does, in fact, bring the critical density for the CO line down somewhat. The photons emitted by CO are very likely to scatter

off of molecules that they encounter, which is what makes the cloud optically thick to photons of that particular energy. That means that an emitted CO photon will bounce around inside of the cloud for a while after it is emitted, before it escapes from the cloud. This process is similar to increasing the timescale at which the CO photons are emitted, and as a result, the critical density at which the emission timescale equals the collisional excitation timescale is reduced. The true critical density for the ^{12}CO(1-0) transition is $10^3/\tau$ where τ is the optical thickness of the cloud to the CO emission. However, as long as $\tau < 1000$, there could still be places where CO signals are weak, but OH could be used as a more reliable tracer for molecular gas.

1.4 Origin of the OH 18 cm Transitions

The radio transitions from OH that we observe are all within the ground state (see Figure 1.1), and arise from smaller scale energy level transitions within splitting of that ground state. For a more detailed discussion of the energy levels, see Townes & Schawlow (1955). The first splitting of energy levels is fine structure splitting. This splitting is independent of the rotation of the molecule, and occurs as a result of spin-orbit coupling of the unpaired electron. These two states are referred to as $^2\Pi_{3/2}$ and $^2\Pi_{1/2}$ where J = 3/2 and J = 1/2 respectively. The 18 cm transitions that we study are all within the $^2\Pi_{3/2}$ state and result from further splitting in the form of lambda doubling, and then hyperfine splitting.

A second splitting, called lambda doubling, occurs for the OH molecule as well as other molecules of diatomic structure with an unpaired electron. See Townes & Schawlow (1955) for a derivation of this phenomenon. We refer to the two lambda doubling states as as + and - because of their opposite parity. The lambda doubling produces a difference in energy levels corresponding to approximately 18 cm radio waves, allowing for a transition of radio frequency.

Lastly, we consider the coupling of the unpaired electron spin with the nuclear spin, which results in hyperfine splitting. The total spin of the oxygen nucleus is zero for the most common isotope because although each proton or neutron has spin 1/2, there is an even number of protons and of neutrons, and all of these spins cancel out. However, the hydrogen nucleus is just a simple proton (again, assuming the most common isotope), so its spin 1/2 is not cancelled. Thus the total relevant nuclear spin is 1/2, and this spin can either align with the unpaired electron spin or anti-align, creating a split into two different energy levels. Thus for the $^2\Pi_{3/2}$, J = 3/2 state, there will be a lambda doubling into a negative and a positive lambda state, and then each of these will be doubly split yet again into an F = 3/2 - 1/2 = 1 state and an F = 3/2 + 1/2 = 2 state. This final splitting of each of the lambda doubling states results in the four transitions within the $^2\Pi_{3/2}$: 1612 MHz, 1665 MHz, 1667 MHz, and 1720 MHz, as seen in the figure, at the bottom left corner.

We conclude this discussion of the four OH 18-cm lines by pointing out that the product of the Einstein B coefficients and the degeneracies of the energy levels for the

four lines are in the ratio 1:5:9:1 for the 1612, 1665, 1667, and 1720 MHz transitions respectively (Elitzur 1992). These weights determine the ratio of line strengths for the four 18 cm lines assuming that other factors such as enhanced emission or differences in the values of the excitation temperature, which will be discussed in the next section, are irrelevant.

1.5 Radiative Transfer, the Excitation Temperature, and Column Densities

The equations used to calculate column densities of OH from the observed line strengths are derived from the equation of radiative transfer for a uniform slab:

$$T_b(\nu) = (T_{ex} - T_C(\nu))(1 - e^{-\tau(\nu)}), \tag{1.6}$$

where $T_b(\nu)$ is the brightness temperature of the observed line profile emanating from the slab as a function of frequency ν, $T_C(\nu)$ is the continuum temperature resulting from the total continuum emission in the background of the slab, $\tau(\nu)$ is the optical depth of absorption on the line of sight through the slab defined by $\tau(\nu) = \ln(T_C/T_C + T_b(\nu))$, and T_{ex} is the excitation temperature of the transition, which is a measure of the partition function of energy level populations of the gas in

question. The excitation temperature is defined by the equation

$$\frac{n_u}{n_l} = \frac{g_u}{g_l} e^{-h\nu/k_B T_{ex}}, \tag{1.7}$$

where n_u and n_l are the populations in the upper and lower energy levels respectively, and g_u and g_l are degeneracies. The excitation temperature is not a real temperature, but is merely the value in the equation that mimics the role temperature plays in a Boltzmann distribution for the given distribution of energy level populations.

Our goal is to calculate column densities of OH from observable and measurable quantities, such as line profile integral, continuum temperature, and excitation temperature. Starting from Equation 1.6, we can derive equations for column densities of OH N(OH) to be calculated for both emission profiles and absorption profiles, where temperatures are measured in Kelvin and column densities are measured in cm^{-2} (see Liszt & Lucas 1996).

For emission lines, the column density is given by

$$N(OH) = C \frac{T_{ex}}{T_{ex} - T_C} \int T_b(\nu) d\nu \tag{1.8}$$

where the coefficient $C_{67} = 2.3 \times 10^{14}$ for the 1667 MHz line, and $C_{65} = 4.1 \times 10^{14}$ for the 1665 MHz line, which is 9/5 times the 1667 MHz coefficient.

For absorption lines, the column density is given by

$$N(OH) = CT_{ex} \int \tau(\nu) d\nu. \tag{1.9}$$

The optical depth τ is calculated from the continuum temperature and observed line brightness temperature above that continuum value as $\tau(\nu) = ln(T_C/(T_C + T_b(\nu))$. In the case of absorption lines, that T_b value is negative since the line dips below the continuum.

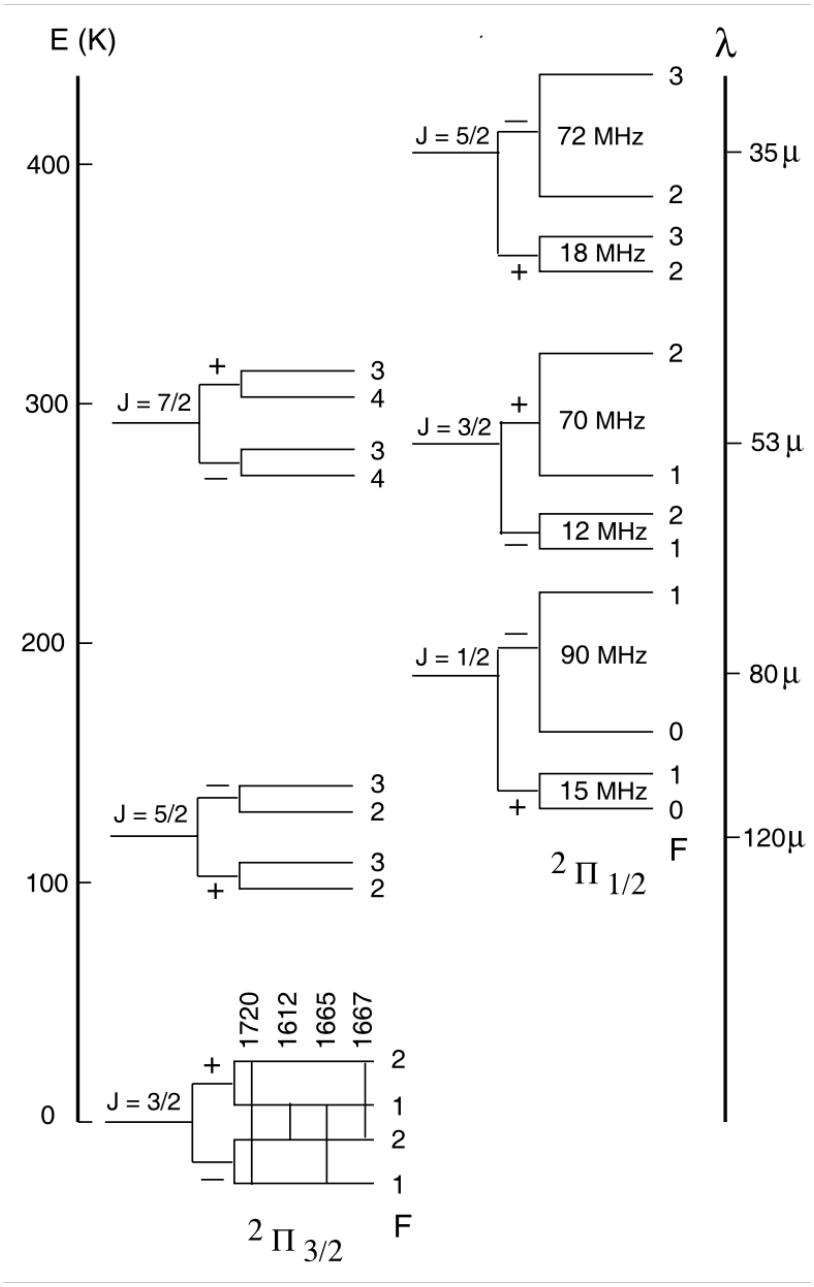

Figure 1.1: Diagram of the energy levels of the OH molecule, taken from Lockett & Elitzur (2008) Figure 1. The 18 cm transition results from the J = 3/2 level at the bottom left, and the four lines resulting from lambda doubling and then hyperfine splitting are shown.

Chapter 2

Excitation Temperatures of the OH 18 cm Lines in W5

2.1 Introduction

2.1.1 Background

This work is part of a broader project to study the suitability of the OH 18-cm transition as an alternate tracer for molecular gas in the Galaxy; see Allen et al. (2012, 2013) for the initial motivation and Allen et al. (2015) for first results from this project. Tracing the molecular gas component of the ISM is complicated by the fact that the primary component of this gas, H_2, is not itself usually detectable in the conditions of interstellar molecular gas clouds, so signals from other molecules must

be used as tracers. Despite its universal use as a tracer of cold molecular gas, the ^{12}CO(1-0) transition is not an ideal tracer for molecular gas below the critical density of $\sim 10^3$ cm$^{-3}/\tau$. Moreover, evidence from gamma-ray and IR surveys suggests the presence of undetected gas in the Galaxy, which is likely molecular and which likely contains a mass similar to the mass of known Galactic molecular gas (Grenier et al. 2005; Tibaldo et al. 2015). In our work, OH serves as an alternate molecular gas tracer with a critical density of ~ 10 cm^{-3}. We have found that for some molecular gas features, the OH and the CO traced the same amount of molecular gas and fell on a linear relation, whereas for other molecular gas features, the CO either under-predicted the molecular gas column density as compared to the OH results, or was not even detected above the noise. The conclusion in Allen et al. (2015) was that OH traces a larger component of the molecular ISM than CO does, providing a means to probe the "CO-dark" molecular gas, and also has the benefit of being an optically thin line so column densities can be calculated directly.

One closely-related goal is to determine the molecular gas content in a star-forming region using OH emission, and to compare the values so obtained with those inferred using the CO(1-0) tracer for the molecular ISM. It is widely accepted that star-forming regions in galaxies contain an abundance of interstellar gas, and furthermore it is this higher gas abundance which is itself the cause of the elevated rate of star formation. The evidence for a close association of CO emission with star formation is primarily based on studies of active star-forming regions in our own Galaxy. However,

we have described evidence that there is molecular gas in the ISM that is not traced by CO. Is there even more molecular gas hiding in star-forming regions, and could the 18-cm OH transition be used to find it? Or alternatively, is the molecular gas in star-forming regions adequately traced by CO emission because of the higher density of these regions, whereas it is only in quiescent regions in which a CO-dark component to the molecular gas exists? These questions motivate the application of the OH 18-cm transition as a molecular gas tracer to a star-forming region. To that end, a blind grid survey of the main OH lines at 1665 and 1667 MHz has been carried out over the star-forming region W5 with the Robert C. Byrd Green Bank Telescope (GBT).

W5 was chosen as a target for our grid survey because it is a star-forming region of modest angular size compared to the resolution of the GBT, allowing lengthy 2-hour observations in a dense grid of $\sim$ 75 pointings over the nebula to be carried out in a feasible amount of observing time. In addition, extensive results on this nebula are available in the literature including radio continuum data provided by the Canadian Galactic Plane Survey (Taylor et al. 2003) and used in a detailed study of the properties of the W3-W4-W5 complex (Normandeau et al. 1997). That study shows that the brightness of the radio continuum emission emanating from W5 has values small enough to allow OH emission as well as absorption to be detected in the foreground gas. Finally, W5 is sufficiently simple in structure and activity so as to be tractable for analysis, and does not contain large numbers of masers or copious IR radiation which might adversely affect our ability to analyze the OH L-band emission

in terms of column density in the ISM.

However, before column densities of OH can be computed from those observations, accurate values for the excitation temperatures T_{ex} of the OH 18-cm lines in W5 must be known. Knowledge of T_{ex} is particularly important when the OH emission is found in regions with star formation activity, because the excitation temperature of the L-band lines is known from previous work to be only a few degrees above, or comparable to, the background value established by the sum of the Cosmic Microwave Background (CMB), the Galactic non-thermal radio continuum emission, and the thermal radio continuum emission from the star-forming region itself. The difference between the total ambient L-band radiation field and the excitation temperature is one factor that determines the intensity of the observed emission lines, and hence the column density of OH obtained from the observations. This chapter focuses on measurements of T_{ex} for the two main OH lines in order to permit accurate determinations of OH column densities in the ISM. The column density results will be reported in Chapter 3 (Engelke & Allen 2019).

2.1.2 OH Excitation Temperatures

The two main 18-cm lines of OH at 1665 MHz and 1667 MHz were first detected in absorption in the ISM by Weinreb et al. (1963) in front of the continuum source Cas A. OH in emission was first reported by Weaver et al. (1965) in an HII region, and then by Heiles (1968) in interstellar dust clouds. An extensive survey of northern

hemisphere radio sources for OH absorption in the Galaxy was carried out by Goss (1968b). At first, it was generally assumed that T_{ex} was the same for the two main lines at 1665 MHz and 1667 MHz; Heiles (1969) reported that his observations did not show evidence for a difference between the main-line excitation temperatures.

During the next few years, it was unclear if T_{ex} was the same at the two main lines, or if there were differences. Some evidence for T_{ex} differences was found by Manchester & Gordon (1971), and Turner (1973), although those results were disputed (Heiles & Gordon 1975). Moreover, these results varied from finding evidence that T_{ex} was larger at 1667 MHz to finding that T_{ex} was larger at 1665 MHz. Nguyen-Q-Riu et al. (1976) found evidence that $T_{ex}^{65} - T_{ex}^{67}$ of approximately 1.5 K, but with sufficient uncertainty as to claim that the difference was "not significant." Crutcher (1977, 1979) found more definitively that $T_{ex}^{65} > T_{ex}^{67}$ in dust clouds in front of several continuum sources at a number of LSR radial velocities between -10 km/s and 10 km/s, all closer to the sun than in the present study of W5. Crutcher (1979) reported that $T_{ex}^{65} - T_{ex}^{67} = 1 - 2$ K, and also described an observation in which OH emission was detected at 1665 MHz while absorption was detected at the same position at 1667 MHz, providing a 4σ qualitative result that $T_{ex}^{65} > T_{ex}^{67}$ at that location in the sky near 3C 154 and at -1 km/s LSR radial velocity. Such a difference was not, however, reported by Liszt & Lucas (1996). Li et al. (2018) provide a distribution of T_{ex} measurements, with a peak near 3.4 K but an average value of the measurements ranging from approximately 4.8 K to 7.0 K, their exact average value depending on whether the measurements are

weighted by the errors when averaging, and with an excitation temperature main line difference no greater than 2 K. A table of T_{ex} measurements from the literature is assembled in Section 3.11.

2.1.3 Another Approach

The measurement of excitation temperatures has traditionally employed what we shall call the "expected profile" method, where an estimate of the expected emission profile at the sky position of the distant source of continuum emission is provided by interpolating from the emission profiles recorded at offset positions around the location of the continuum source. This method is subject to several uncertainties caused by spatial gradients in the foreground absorbing gas and differences in the effective solid angle covered by the distant radio continuum source and the telescope used to determine the expected profile. This method has nevertheless been used by many researchers dating back to the early observations (Crutcher 1972; Manchester & Gordon 1971; Nguyen-Q-Riu et al. 1976); see Liszt & Lucas (1996) for a more detailed description of the method.

In the course of analyzing the GBT W5 data, we have implemented an alternative method for measuring the excitation temperatures of the OH lines. We make use of the natural variations in the 18-cm radio continuum brightness over W5 and the fact that the values of the continuum brightness temperature T_C in this nebula are close to the excitation temperature of the main OH lines in the foreground gas. The

key is that if T_C is less than T_{ex}, lines will appear in emission, if T_C is greater than T_{ex}, lines will appear in absorption, and if $T_C = T_{ex}$, the lines will disappear. Some aspects of this approach were also used by Neufeld et al. (2002), and the reasoning that T_C where an emission line disappears and then switches to absorption indicates T_{ex} was discussed by Tang et al. (2017). This method, which we call the "continuum background" method, unequivocally shows that the OH molecular gas in front of the W5 continuum source has $T_{ex}^{65} > T_{ex}^{67}$.

In order to compare these results with the traditional expected profile method, we have supplemented the GBT observing program with OH absorption measurements on extragalactic radio sources seen through the radio image of W5; these absorption observations have been done with the Karl G. Jansky Very Large Array (VLA). In the following section we describe both of these interconnected observing programs.

2.2 Observations

Observations for this work made use of the 100-m Green Bank Telescope (GBT) in West Virginia and the Very Large Array (VLA) in New Mexico. The GBT was used for both methods of determining the OH excitation temperatures; the VLA data was used only for the expected profile method. The grid of GBT pointings and the locations of the 3 NVSS sources observed with the VLA are shown in Figure 2.1 superposed on a drawing from Karr & Martin (2003) Figure 2 of the distributions of

radio continuum (gray scale) and CO(1-0) emission (contours) in the region of W5.

All GBT observations were performed with the VEGAS spectrometer in L-band, with 2 hours of exposure per pointing in frequency-switching mode. All four OH 18-cm transitions at 1612 MHz, 1665 MHz, 1667 MHz, and 1720 MHz, plus 1420 MHz HI were recorded simultaneously; however, only the 1665 MHz and 1667 MHz "main-line" spectra were used in this work. The beam size of the GBT at 1667 MHz was 7.6' FWHM, and the spectrometer channel spacing was 0.515 kHz, corresponding to 0.0926 km/s at 1667 MHz. The GBT spectra were smoothed off-line to a Gaussian FWHM resolution of 1.0 km/s. The RMS noise level in the final smoothed spectra was 0.0028 K per channel. A total of 80 GBT pointings was made in the W5 grid survey between February 2016 and April 2017, and an additional eight GBT observations were made between February 2017 and August 2017 in order to construct the expected profiles near 2 of the 3 compact continuum sources from the NVSS catalog (Condon et al. 1998) observed with the VLA in the immediate area of W5. The third NVSS source turned out not to be suitable for the expected profile method because its surroundings contained $T_C > T_{ex}$.

VLA observations of three compact continuum sources NVSS J030317-602752 (Source 1), NVSS J030723-604522 (Source 2), and NVSS J025947-604325 (Source 3), in or near the radio image of W5 were performed in the D configuration as well as the DnC hybrid configuration with the L-band receiver, providing a resolution of 62". The channel separation in the spectrometer was 10.845 kHz corresponding to

1.95 km/s at 1667 MHz. These three sources were observed in April 2017 and May 2017, with different exposure times depending on the flux density of the source. Unfortunately, owing to limitations on the observing time available, only the brightest source received the full intended exposure times of 3.3 hours; Source 2 received 17.6 hours, and Source 3 received 18.7 hours.

2.3 Results and Analysis

Both of the methods we use to measure excitation temperatures begin with the simplest form for the equation of radiative transfer for a uniform slab:

$$T_L = (T_{ex} - T_C)(1 - e^{-\tau}), \tag{2.1}$$

where T_C is the spectrum of the total continuum emission incident on the back of the slab, T_{ex} is the excitation temperature of gas in the slab for the level under study, T_L is the observed emission profile exiting the slab, and τ is the absorption line optical depth through the slab. This equation immediately suggests the solution for the phenomenon described in Section 1.3; if $T_{ex} > T_C$ the spectral line exiting the slab will be seen in emission, but if $T_{ex} < T_C$ it will be seen in absorption. Crucially, if $T_{ex} = T_C$, the emerging profile will disappear. If the value of $T_C = T_{CMB} + T_{Gal} + T_{W5}$ at that point is known to some precision, the value of T_{ex} can be determined with the same precision. Furthermore, the difference in the values of T_C where the two

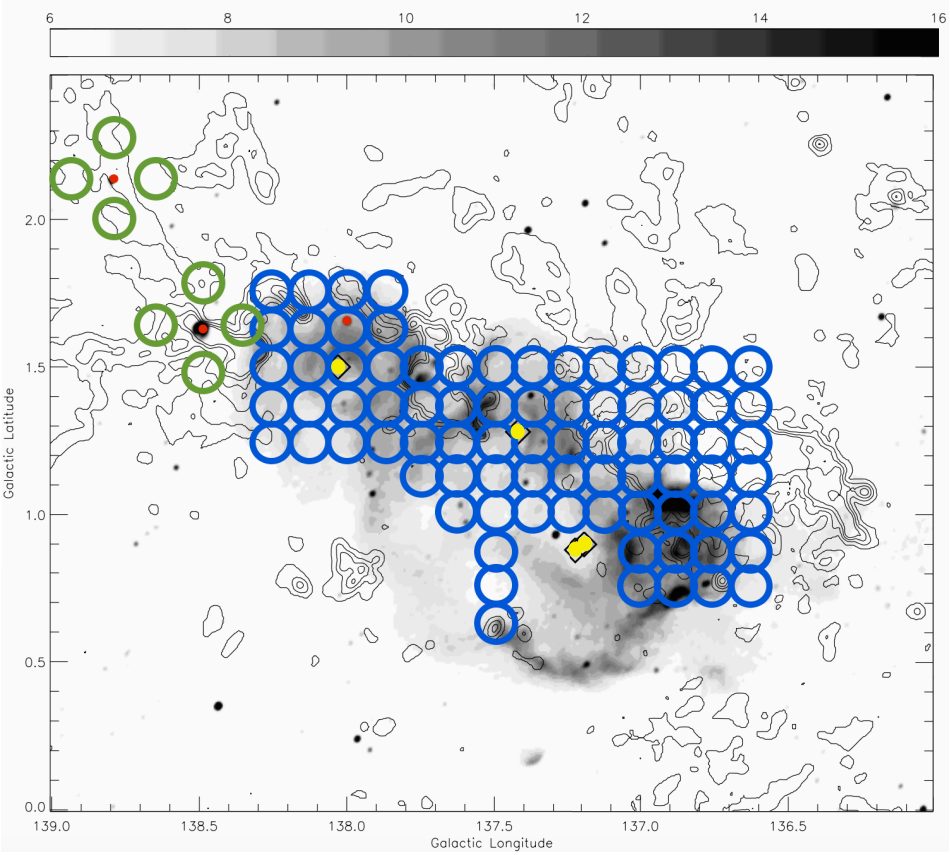

Figure 2.1: Positions of our GBT and VLA observations overlaid on the map of the W5 region taken directly from Karr & Martin (2003) Figure 2. The gray scale indicates the 1420 MHz continuum, the contours indicate CO emission in the LSR radial velocity range of -49 to -31 km/s, and the 4 diamonds (which we have emphasized in yellow) indicate the locations of known O stars. On top of the map we have plotted a number of blue circles indicating the positions of our GBT observations in the grid survey, with the circle size equivalent to the point spread function FWHM of 7.6'. The 3 red dots indicate the positions of our VLA observations, and the two sets of 4 green circles indicate the positions of our GBT observations in the vicinity of two of the 3 VLA observations for expected emission profile detection (the third set of 4 pointings is already covered in the grid of blue circles).

main lines disappear is the difference in their excitation temperatures. Since the values of T_{CMB} and T_{Gal} are expected to vary only slowly over the radio image of W5, the difference in the excitation temperatures of the two main lines $T_{ex}^{65} - T_{ex}^{67}$ depends on the variations in T_{W5}, removing the necessity for an absolute measurement of continuum temperatures, but requiring an accurate relative continuum surface brightness distribution. This continuum image will be described next.

2.3.1 A Continuum Image of W5 at 1667 MHz

In order to maximize sensitivity, the GBT observations were made using frequency-switching instead of position-switching. Unfortunately, such observations do not provide information about the continuum temperatures. We have interpolated observations from the Canadian Galactic Plane Survey at 408 MHz and 1420 MHz (Taylor et al. 2003) and the Effelsberg survey at 2695 MHz (Fürst et al. 1990) from their observed frequencies to the main OH lines assuming a multi-component radio spectrum including background contributions and contributions from W5, and we smoothed the result to the spatial resolution of the GBT observations. However, it was first necessary to separate the free-free emission of W5 from the cosmic microwave background and the Galactic background. The Effelsberg data defined the background in the W5 vicinity as 0 K, so only the W5 free-free emission was included in that data. On the other hand, the Canadian Galactic Plane Survey data gives the absolute continuum temperatures, meaning that the background in the vicinity of W5 is not zero, and

includes contributions from the CMB and the Galactic background. Our estimates for the background at 408 MHz and 1420 MHz contribute some uncertainty to the results for T_C, estimated as ±7K at 408 MHz and ±0.25K at 1420 MHz. A linear fit was made to the logarithm of the T_C values plotted against the logarithm of the frequencies, yielding a spectral index of -1.8 ± 0.15, which is consistent with theoretical expectations for free-free emission. We then interpolated from 1420 MHz T_C data smoothed to the resolution of the GBT observations using the spectral index of -1.8 to find T_C at 1667 MHz. The uncertainty in T_C at 1667 MHz is ± 0.07 to 0.1 K, depending on the magnitude of T_C.

2.3.2 Difference in Excitation Temperature Between the Main Lines

One benefit of using the continuum background method is that this method demonstrates clearly that $T_{ex}^{65} > T_{ex}^{67}$. At five positions with the appropriate continuum temperature, the 1665 MHz line appears in emission while the 1667 MHz line at the same position, with the same continuum background and OH content, appears in absorption (see Figure 2.2 for an example). The observations make sense in the context of a difference in T_{ex} values between the two main lines. In that case, for the same T_C, $T_{ex}^{65} > T_C$ so the line appears in emission, and $T_{ex}^{67} < T_C$, so the line appears in absorption. Then, for a higher value of T_C, we find cases in which the 1665 MHz

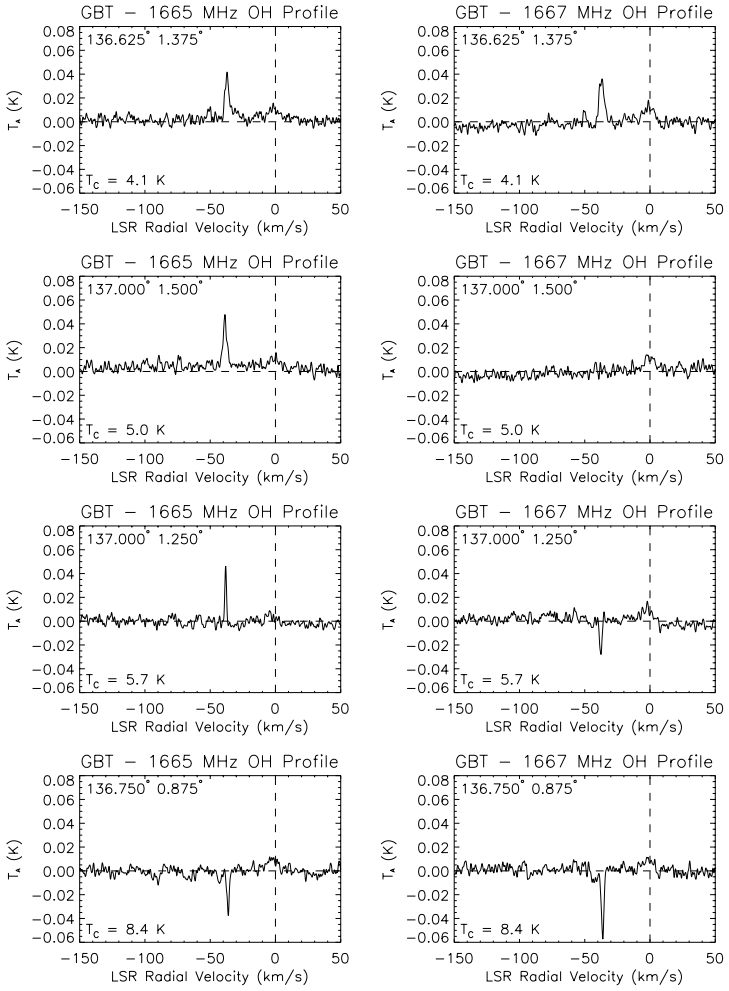

Figure 2.2: Illustration of excitation temperature estimation using the continuum background method with OH spectra from the GBT survey of W5. The spectra at each row are from different positions in W5 with a continuous increase in continuum temperature going downward in the figure. The spectra on the left are at 1665 MHz, and the spectra on the right are at 1667 MHz. As the continuum temperature gradually increases, OH features eventually change from emission to absorption. The continuum temperature at which the switch from emission to absorption occurs indicates the excitation temperature of the OH line. The excitation temperature is not the same at 1665 MHz and at 1667 MHz. This point is made clearly by the fact that whereas the 1667 MHz spectra change from emission to no apparent signal to absorption from the first to the third rows downward, the 1665 MHz spectra at these same positions (and with the same continuum temperatures) are all emission lines. Not until the bottom row does the 1665 MHz line change to absorption, which occurs at a higher continuum temperature.

line and 1667 MHz line are both absorption lines, indicating that T_C in these cases is greater than T_{ex}^{65}. Similarly, we find cases in which the 1665 MHz line and 1667 MHz line are both emission lines, indicating that T_C in these cases is less than T_{ex}^{67}.

Considering that the qualitative result that $T_{ex}^{65} > T_{ex}^{67}$ depends only on the emission and absorption nature of the line profiles, we can say that the confidence of this result is equivalent to the signal-to-noise of the line detections in the GBT observations. That means that in contrast to previous findings that $T_{ex}^{65} > T_{ex}^{67}$ in the literature, which depended on separate measurements of the values of T_{ex} for the two main lines and therefore was subject to the uncertainty in those measurements, we report a confidence that $T_{ex}^{65} > T_{ex}^{67}$ in the W5 region to 7σ, and we have observed five examples of this type of spectrum (see Figure 2.3).

2.3.3 Analysis using the Continuum Background Method

Whereas the major source of uncertainty for the expected profile method is unknown variation in OH distribution in the tangential direction, the major source of uncertainty for the continuum background method is the unknown distribution of OH emission along the line of sight. A simplifying assumption that can be made for the continuum background method is that OH must be located entirely in front of or behind the continuum emission in W5 because otherwise OH would be dissociated in

the HII region by high energy photons. This might be a reasonable assumption, but it is based on a simplified model of the geometry. In reality, HII regions and molecular clouds are not spherical, and fractal-like geometry paired with shielding effects could complicate this model significantly.

In order to determine values of T_{ex}^{65} and T_{ex}^{67}, we produce a map of the survey region and color code all coordinates with OH detections at W5 radial velocities based on the types of OH detections that were observed at those coordinates, as seen in Figure 2.3. We start by accepting the assumption that OH is located entirely in front of or behind the free-free continuum source along the line of sight. Looking at Figure 2.3, we identify four estimates of T_{ex} at 1667 MHz from the orange-circled coordinates, and taking the mean with standard deviation as the uncertainty, we obtain $T_{ex}^{67} = 5.1 \pm 0.2$ K. Uncertainty resulting from possible variation in T_{ex} along the lines of sight is unlikely to be greater, and if it were, a combination of emission and absorption in a single profile would probably be visually apparent. The uncertainty in T_C does not increase the total uncertainty by more than a few tenths of a degree when summed in quadrature. Determining T_{ex}^{65} is a bit more difficult because there are only two coordinates with observations of a non-detection at 1665 MHz and an absorption detection at 1667 MHz, and this OH is evidently located farther back along the line of sight than most of the other OH detections. We surmise that it is located farther back because T_C at these two brown-circled pointings varies by 0.8 K, and also both of these pointings have higher apparent T_C than some of the

purple-circled pointings. We already know that the assumption that OH is located in front of or behind the continuum source is not always true, so the following estimates are actually upper limits. Looking at the boundary between red- and purple-circled coordinates in Figure 2.3, we estimate a value of $T_{ex} = 6.0 \pm 0.5$ K, because it seems evident from the red-circled observation at 5.9 K and the purple-circled observation at 6.0 K ($l = 137.5°$, $b = 0.625°$) as well as various red-circled observations at lower T_C values and purple-circled observations at higher T_C values, that the boundary between red- and purple-circled positions occurs where T_C is around 6.0 K. On the other hand, there is a stray purple-circled observation at 5.5 K, so we choose an uncertainty value of ± 0.5 to cover this variation. The variation is most likely the result of a more pronounced absorption profile at the left edge of the GBT beam dominating over a weaker emission profile in the remainder of the beam, although the possibility that it is evidence of T_{ex} variation, uncertainty in T_C, or the presence of OH in shielded pockets within the HII region at other observed positions should be noted. Our estimates using this method are:

$$T_{ex}^{65} = 6.0 \pm 0.5 \text{ K},$$

$$T_{ex}^{67} = 5.1 \pm 0.2 \text{ K},$$

$$T_{ex}^{65} - T_{ex}^{67} = 0.9 \pm 0.5 \text{ K}.$$

Note that the blue-circled observation at $l = 138.25°$, $b = 1.5°$ can be understood by remembering that OH features may be found in front of or behind the HII region associated with W5. This case is probably simply one where the OH is behind the

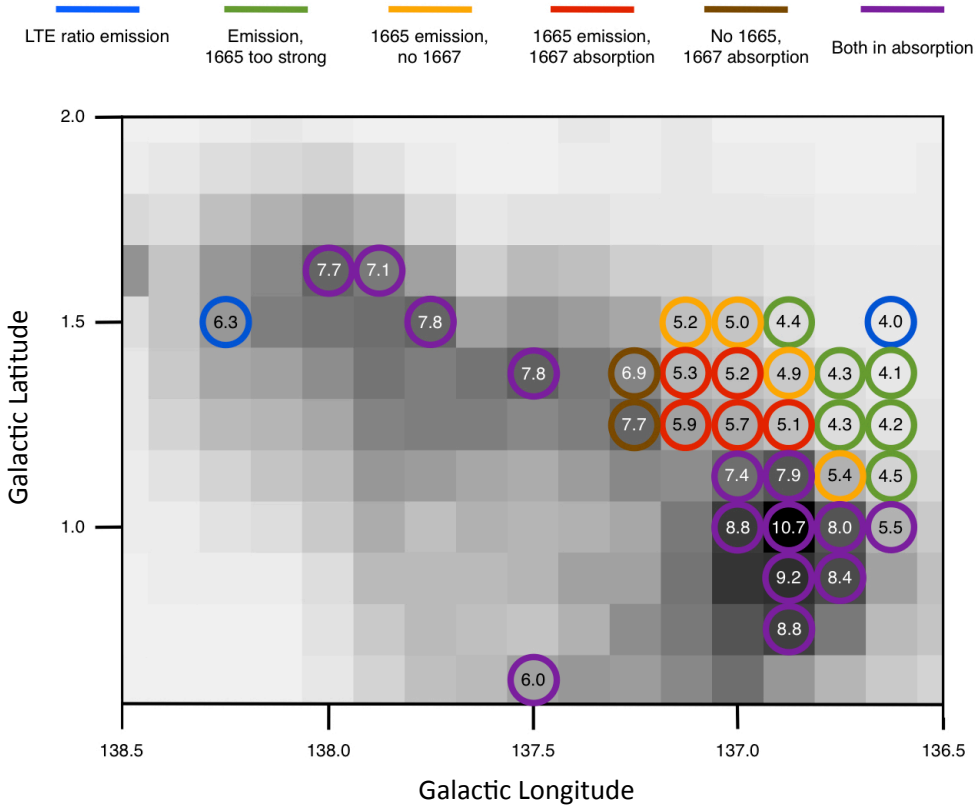

Figure 2.3: Map of 1420 MHz continuum in W5 smoothed to GBT survey resolution from the Canadian Galactic Plane Survey (Taylor et al. 2003) in gray, with all positions observed in the GBT OH survey that contain OH feature detections at W5 radial velocities indicated with colored circles. The colors refer to the types of OH features observed at 1665 and 1667 MHz, as indicated in the key, and the numbers written inside of the circles are the values of the continuum temperature at 1667 MHz for the GBT survey resolution. Excitation temperatures for the 1667 MHz and 1665 MHz lines can be estimated from the continuum temperatures at the orange-circled positions, and the boundary between red- and purple-circled positions, respectively.

HII region, so the T_C value behind the OH is actually about 4.1 K rather than 6.3 K.

More complicated line of sight geometry could result in greater uncertainties than reported in the estimates. If we cease to assume that all OH must be either in front of or behind the continuum emission (as we already know is not the case at the two brown-circled positions), then T_C behind the observations could be lower than we assumed. In that case, the estimates reported above are upper limits on T_{ex}. The lower limit would be the T_C background from the CMB and the Galaxy, which amounts to ~ 4 K in this region, giving us:

$$4 \text{ K} < T_{ex}^{65} < 6.5 \text{ K},$$

$$4 \text{ K} < T_{ex}^{67} < 5.3 \text{ K},$$

$$T_{ex}^{65} - T_{ex}^{67} \leq 0.9 \pm 0.5 \text{ K}.$$

2.4 The Expected Profile Method

The "continuum background" method described previously for measuring T_{ex} has an attractive simplicity for the specific case of OH measurements. However, it is clearly not applicable in general; suitable extended continuum sources are not available everywhere on the sky, nor do they always have continuum surface brightnesses similar to the excitation temperature of the ISM tracer in question. In any case, it is also important to establish that the results of the new method are in agreement with those obtained with the more common "expected profile" method. This section explores that comparison.

The "expected profile" method of measuring excitation temperatures proceeds as follows: if absorption and emission lines are both detected in close proximity, the emission line temperature profile T_L (i.e. the "expected profile") and the absorption line optical depth τ can be used to estimate T_{ex} of the OH lines in the region. Assuming small optical depth we can write Equation 2.1 as:

$$T_{ex} \approx \frac{T_L}{\tau} + T_C. \tag{2.2}$$

where T_L is the expected profile of the emission line at the location of the continuum absorber. This profile is obtained by averaging the emission profiles observed in regions immediately adjacent to the background radio continuum source, T_C is the continuum temperature in the observations of the emission expected profile, and τ is the absorption line optical depth in front of the background continuum source.

2.4.1 Analysis using the Expected Profile Method

We begin by noting the assumptions involved in using the expected profile method. We assume that T_{ex} for a given line is constant throughout the region. This may not in fact be true, but we have found no evidence for significant differences. A second assumption is that the OH column density does not vary tangentially over the region around each continuum (VLA) source where the GBT expected profile observations were performed. In reality, this assumption is almost certainly violated, as can be

inferred e.g. from the rapid variations in CO column densities in those regions shown in Figure 2.1, and is likely to dominate the uncertainties. We will estimate errors resulting from this variation as we perform the analysis. Given this complication, it is remarkable that Crutcher (1979) was able to detect that $T_{ex}^{65} - T_{ex}^{67} = 1 - 2$ K using the expected profile method; one possible reason is that he was observing OH features which are located closer to the sun, probably within ~ 0.5 kpc according to their radial velocities, and hence cover solid angles on the sky ten to twenty times that of ours. The Crutcher (1979) beam size of 22' diameter covered an area roughly comparable to the size of the region covered by our four GBT observations for the expected profile of each NVSS source, which has a diameter of 25.6', so it makes sense that there would be less variation in OH column density within the region observed by Crutcher (1979) than in ours.

Of the three NVSS extragalactic continuum sources observed with the VLA over the area of W5, only two were useful for the analysis because T_C turned out to be greater than T_{ex} in the vicinity of the third source. The two remaining sources are located at $l = 138.497°, b = 1.64°$ (Source 1), and at $l = 138.792°, b = 2.142°$ (Source 2). The absorption spectra of these sources observed with the VLA at 1665 and 1667 MHZ are shown in the top pair of panels in Figure 2.4 and Figure 2.5.

VLA observations of Source 1 as well as three of the four nearby GBT observations for the expected emission profile are shown in Figure 2.4. The fourth GBT observation was not used because T_C at that position was too high. The VLA obser-

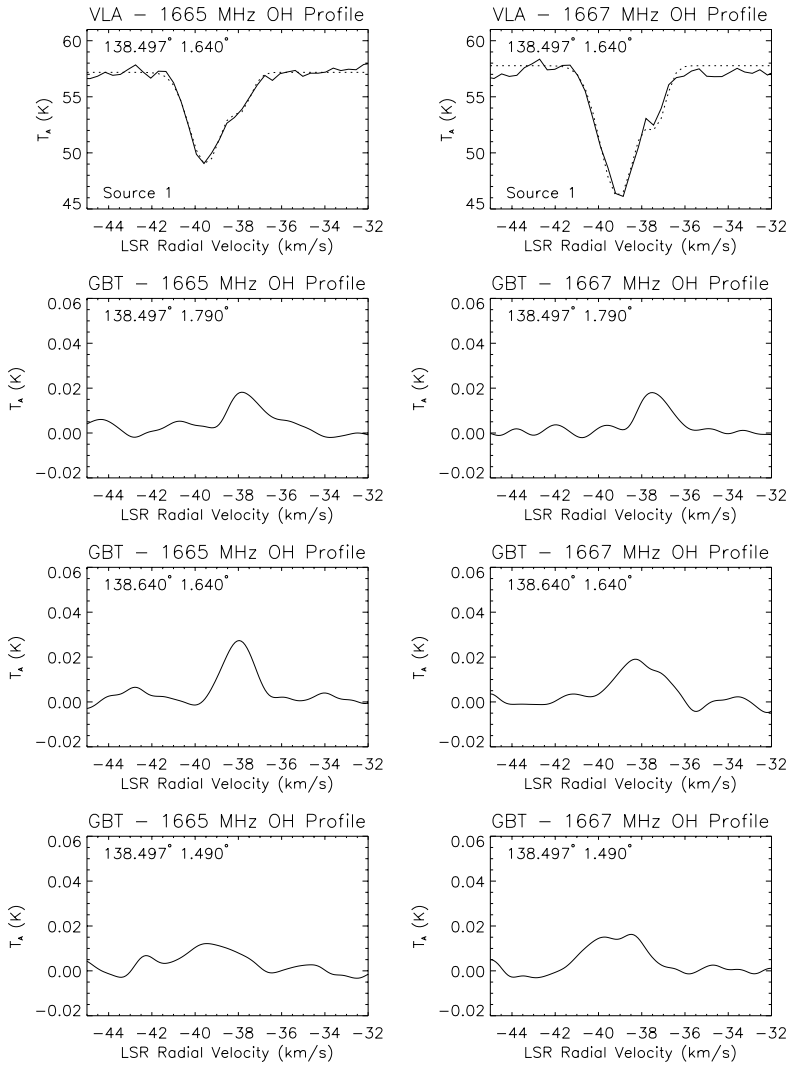

Figure 2.4: VLA absorption spectra from Source 1 and GBT emission spectra from its vicinity for the expected profile. The VLA absorption spectra are fitted with a two-component Gaussian, which is superimposed on each VLA spectrum as a dashed line. The two components of the fit are shown separately in the second row, as a dashed line, and the velocities at the centroids of these Gaussian fit components are marked on all rows as vertical dotted lines. Variation in GBT spectra among rows two, three, and four demonstrates some of the variations in OH content and distribution over the region that increases the uncertainty in T_{ex} determined with the expected profile method. Also worth noting is the unusual case in the fourth row in which the 1665 MHz line appears to be brighter than the 1667 MHz line and the secondary component appears to dominate. This deviation is within the uncertainty so it could be attributed to noise, or perhaps it is evidence of a localized anomaly in the secondary component.

vations at Source 1 reveal the presence of two OH components: a primary component centered near -39 km/s (called Component A), and a secondary component centered near -37.5 km/s (called component B). The expected profiles made by averaging the GBT spectra from observations surrounding Sources 1 and 2 respectively also display these two components, but in the case of the individual GBT spectra averaged, both components are not always detected together. As a result, it makes sense to treat the two components as separate OH features, fit the VLA absorption data as a sum of two Gaussian components, and compare the optical depth and line temperature values for the corresponding components when using Equation 2.2 to estimate the excitation temperatures. These T_{ex} values can then be averaged together after their separate determinations, but if the components of the OH features are not treated separately, the analysis will be faulty. The results of this exercise are given in Table 2.1. The uncertainties reported in this Table are calculated only from the error in the profile integral and the absorption optical depth measurements.

In order to estimate the error resulting from variation in OH, we look at some of the variation in OH profile integrals between adjacent pointings within our survey. We choose an example with background $T_C = 4.0$ K in order to best approximate the regions surrounding Sources 1 and 2, which have similar background T_C values, because we wish to avoid making assumptions about T_{ex} and how that would affect emission profile integral strengths. Between coordinates $l = 138.625°, b = 1.5°$ and $l = 138.75°, b = 1.5°$, the profile integral at W5 radial velocities varies between a

nondetection and a detection, thus providing what seems like a decent estimate of one of the more rapid OH profile integral variations at approximately the relevant angular scale and continuum temperature. Using this estimate of the spatial variation of OH, we find an uncertainty of roughly ±1.5 - 2 K.

Table 2.1: Excitation temperatures for the components of Source 1. Errors from profile integrals and optical depth measurements.

l	b	Profile Component	T_C (K)	T_{ex}^{65} (K)	T_{ex}^{67} (K)
138.497°	1.79°	B	4.1	4.9 ± 0.3	4.5 ± 0.2
138.647°	1.64°	A & B	4.1	4.3 ± 0.2	4.2 ± 0.2
138.497°	1.49°	A	4.2	4.4 ± 0.2	4.3 ± 0.2

Taking the weighted mean of the results from the three positions (using the initial uncertainties before considering possible OH content variation over the region for the weighting), we have for the "expected profile method" result for Source 1 as follows:

$$4.1 \text{ K} < T_{ex}^{65} < 6.5 \text{ K, and } 4.1 \text{ K} < T_{ex}^{67} < 6.3 \text{ K}$$

where $T_C = 4.1$ K is a lower limit for both T_{ex}^{65} and T_{ex}^{67}.

The VLA observations of Source 2 do not contain multiple detected OH components. The VLA absorption data were therefore treated as a single Gaussian component centered near -40 km/s. Three out of the four GBT observations used to create the expected profile for Source 2 contain OH features centered near -40 km/s; the other GBT observation, at $l = 138.792°, b = 2.0°$ contains a double OH emission

profile, neither peak of which is centered at -40 km/s (they are near -46 km/s and -38 km/s), so this spectrum was not used in the expected profile. Ignoring the uncertainty owing to unknown OH variation over the area, we obtain the results given in Table 2.2.

Table 2.2: Excitation temperatures for the components of Source 2. Errors from profile integrals and optical depth measurements.

l	b	T_C (K)	T_{ex}^{65} (K)	T_{ex}^{67} (K)
138.792°	2.284°	3.8	4.9 ± 0.4	4.7 ± 0.3
138.650°	2.142°	3.9	4.9 ± 0.4	4.9 ± 0.3
138.934°	2.142°	3.9	4.6 ± 0.3	4.4 ± 0.2

We again use the uncertainty of 2 K, and also recognize that $T_C = 3.9$ K is a lower limit on T_{ex}. Taking a weighted mean of the results, we find for Source 2 alone:

3.9 K $< T_{ex}^{65} <$ 6.8K, and 3.9 K$< T_{ex}^{67} <$ 6.6 K,

and the mean of the results from Sources 1 and 2 is:

4.0 K $< T_{ex}^{65} <$ 6.4 K, and 4.0 K $< T_{ex}^{67} <$ 6.2 K.

The results are consistent with those from the continuum background method. However, note that the expected profile method is unable to reveal a difference between the excitation temperatures of the two main OH lines in our data.

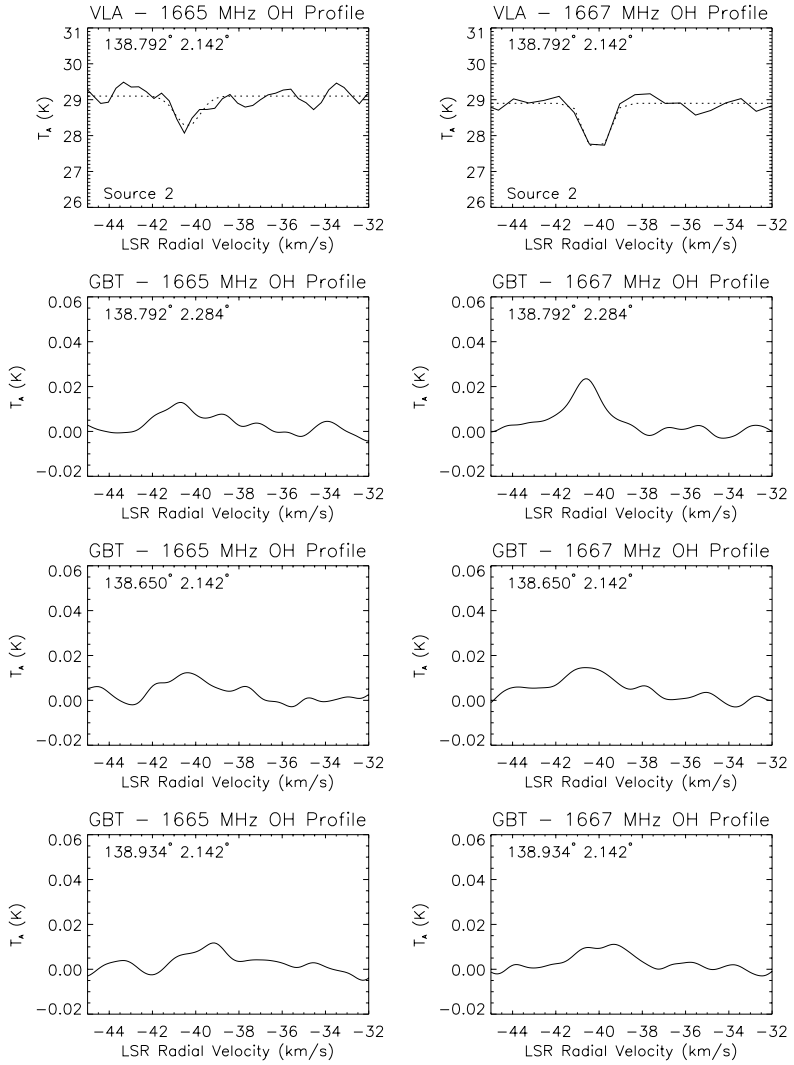

Figure 2.5: VLA absorption spectra from Source 2 and GBT emission spectra from its vicinity for the expected profile. Gaussian fits are performed on the VLA spectra and shown superimposed with a dashed line, and the centroid velocity of the Gaussian fit is displayed as a vertical dotted line on each spectrum.

2.5 Departures from the 5:9 ratio

A consequence of the differences which we have found in the main OH line excitation temperatures is that the ratio of the 1665:1667 main line intensities will differ from the value of 5:9, often referred to as the "LTE" value for optically-thin lines. Of course, high optical depth in the two lines would result in line ratios approaching 1:1. In this section we examine the GBT survey results in W5 for evidence of of such differences. Looking at the ratios of corresponding 1665 MHz and 1667 MHz OH emission lines in the GBT survey, for cases in which both lines occur as emission, one wonders if the emission is consistent with optically thin lines and a Boltzmann distribution energy level partition function. That is an assumption in the derivation of the equations for calculating OH column densities, so it is important to know if any pairs of 1665 MHz and 1667 MHz lines deviate from this partition function. In order to test whether the emission lines at a given coordinate are consistent with a Boltzmann distribution partition function, we start with Equation 2.3 (Liszt & Lucas 1996). This equation relates the column density of OH to T_{ex}, T_C, and the line profile integral. We can write this equation for either the 1665 MHz or the 1667 MHz line, each with its own set of parameters, but the version for 1665 MHz has a different coefficient from the version at 1667 MHz, and they each have a different value for T_{ex} as well. Since the analysis using either line should yield the same value for the

column density $N(OH)$, we can write:

$$\begin{aligned} N(OH) &= C_{67}\frac{T_{ex}^{67}}{T_{ex}^{67}-T_C}\int \phi_{67}(\nu)d\nu \\ &= C_{65}\frac{T_{ex}^{65}}{T_{ex}^{65}-T_C}\int \phi_{65}(\nu)d\nu \end{aligned} \tag{2.3}$$

where C_{65} and C_{67} are the coefficients for the equations at 1665 MHz and 1667 MHz respectively, and T_{ex}^{65} and T_{ex}^{67}, and ϕ_{65} and ϕ_{67} are the excitation temperatures and line profiles at 1665 MHz and 1667 MHz respectively. We know that $C_{65} = (9/5)C_{67} = 1.8C_{67}$, so that:

$$\frac{T_{ex}^{67}}{T_{ex}^{67}-T_C}\int \phi_{67}(\nu)d\nu = 1.8\frac{T_{ex}^{65}}{T_{ex}^{65}-T_C}\int \phi_{65}(\nu)d\nu. \tag{2.4}$$

This equation should be satisfied if the OH energy levels are populated according to a Boltzmann distribution partition function. We find that for the majority of the OH detections in the grid survey with emission at both main line frequencies, Equation 2.4 is satisfied, indicating that the difference in T_{ex} for the two lines is generally sufficient to explain why the lines are outside of the 1:1 - 5:9 ratio without invoking the possible additional effects of anomalous excitation, e.g. by IR photons.

Our observed absorption profiles are also in the 5:9 ratio with the exception of two profiles, which have more complicated structure. At $l = 136.875°$, $b = 1.125°$, there are two absorption lines at 1665 MHz and three at 1667 MHz, and at $l = 137.0°$, $b = 1.1256°$, there is one absorption line at 1665 MHz and two at 1667 MHz. This

curiosity can be explained by noting that one of these OH features could be located farther back along the line of sight, in a shielded pocket in the middle of the HII region. We already noted that this could be true of the two brown-circled coordinates on Figure 5. In the case of the absorption profiles, the explanation could be that the OH feature farther back along the line of sight has $T_C \approx T_{ex}^{65}$ so the line does not appear at 1665 MHz, whereas at 1667 MHz it is observed in absorption along with the other OH profiles. If that is assumed to be the case, the other absorption lines are in a ratio between 1:1 and 5:9, an anomaly that could be attributed to optical depth effects.

2.6 Conclusions

Two methods were used to determine the excitation temperatures of the OH 18-cm main lines in W5. The continuum background method provides the most precise determination yet of the main line excitation temperature difference $T_{ex}^{65} > T_{ex}^{67}$, a 7σ result, consistent with past findings (Crutcher 1979) but with greater significance. Absolute determinations of T_{ex} in W5 are subject to greater uncertainties dominated by the unknown geometry of the OH distribution in the region, but both methods provide consistent results within the uncertainties, and the continuum background method yields the more precise results. Best estimates of the values are $T_{ex}^{65} = 6.0 \pm 0.5$ K, $T_{ex}^{67} = 5.1 \pm 0.2$ K, and $T_{ex}^{65} - T_{ex}^{67} = 0.9 \pm 0.5$ K., although if we avoid

assumptions about simple geometry, these estimates are really upper limits with a minimum T_{ex} value greater than 4 K. These T_{ex} values are similar to those found in less active environments such as dark clouds by e.g. Nguyen-Q-Riu et al. (1976) or Liszt & Lucas (1996), and are also comparable to the average value of the distribution of T_{ex} measurements reported by Li et al. (2018). For a majority of the observed positions in the grid survey of W5, LTE line ratios between 1665 MHz and 1667 MHz hold if the differences in excitation temperatures for these two lines are first taken into account. The definitive confirmation of the result that $T_{ex}^{65} > T_{ex}^{67}$ using the continuum background method demonstrates the need for renewed consideration of possible physical explanations for this phenomenon, although providing such an explanation is beyond the scope of this paper.

2.7 Appendix: Previous Measurements of OH 18-cm Excitation Temperatures

Several measured values for the OH main line excitation temperatures are collected here from the literature. These values have all been determined using the "expected profile" method.

Values of OH Main Line Excitation Temperatures Reported in Selected Past Publications

Publication	$T_{\rm ex}^{65}$ (K)	$T_{\rm ex}^{67}$ (K)
Heiles (1969)	4.5–9.6	4.5–9.6
Manchester & Gordon (1971)	$T_C + 0.0 \pm 0.17$	T_C+0.45 ± 0.14
Turner (1973)	likely higher in six cases	3.71–12.03
Heiles & Gordon (1975)		T_C + (0.13 ± 0.02–1.40 ± 0.81)
Nguyen-Q-Rieu et al. (1976)	≈6.5	≈5.0
Crutcher (1977)	6.0 ± 0.3–7.0 ± 0.5	5.0 ± 0.3
Crutcher (1979)	4.2 ± 0.3 to > 6.7 ± 0.4	3.5 ± 0.2 to > 8.5 ± 0.4
Dickey et al. (1981)		4 K–8 K
Liszt & Lucas (1996)		$T_{\rm CMB}$+(0.2–2.2)
Li et al. (2018)		distribution ($T_{\rm ex}$) $\propto \frac{1}{\sqrt{2\pi}\sigma} \exp\left(-\frac{\ln(T_{\rm ex}) - \ln(3.4\ {\rm K})^2}{2\sigma^2}\right)$

Table 2.3: Value of OH Main Line Excitation Temperatures Reported in Selected Past Publications

Chapter 3

Quantity and Structure of Molecular Gas in W5

3.1 Introduction

3.1.1 Background

Molecular gas is an important part of the interstellar medium (ISM), but its primary component H_2 is difficult to detect in clouds of diffuse gas owing to insufficient collisional excitation of the lowest rotational levels and the lack of a dipole moment. As a result, radio signals from asymmetric molecules with larger moments of inertia are used as surrogate tracers for H_2. Since its discovery in 1970 (Wilson et al. 1970), the (1-0) transition of ^{12}CO near 115 GHz is almost universally used as a tracer of the

large-scale distribution of molecular gas in our Galaxy as well as external galaxies, and has produced a wealth of knowledge about interstellar molecular gas.

However, over the past several decades, numerous questions have persisted concerning the use of the ^{12}CO(1-0) line for accurate quantitative work. First, CO may not be an ideal tracer for measuring molecular gas below the critical density of $\sim 10^3$ cm$^{-3}/\tau$ for this transition, where τ is the optical depth of the gas. Additionally, when a CO(1-0) line is detected, its high optical thickness requires use of an indirect method (the "X-factor" method) to calculate column densities instead of a direct calculation using the equation of radiative transfer. The exact value of this "X-factor" is uncertain, and variations of up to an order of magnitude have been reported (see Bolatto et al. 2013, for a review). Additional information about CO content can be gleaned from other sources such as ^{13}CO(1-0), when such data are available. Finally, recent gamma-ray and IR surveys have provided evidence of undetected gas containing hydrogen nuclei in the Galaxy; this gas is believed to be molecular, and may contain a mass comparable to the currently known mass of molecular gas in the Galaxy (Abdo et al. 2010; Grenier et al. 2005; Tibaldo et al. 2015). Evidence for undetected gas is also provided by dust extinction and emission studies (e.g. Lee et al. 2015; Paradis et al. 2012), and from C^+ emission (Langer et al. 2014; Pineda et al. 2013; Tang et al. 2016). Unfortunately, the specific nature of this "CO-dark" gas is not provided by the gamma-ray and IR studies, nor is kinematic information or accurate structure and mass information available.

An alternative to ^{12}CO(1-0) as a tracer for the large-scale distribution and kinematics of diffuse interstellar gas is thus desirable. In this paper we continue to explore the use of the 18-cm lines of the OH molecule as one alternative tracer. These lines are optically thin, have low critical density ($\sim$ 10 cm^{-3}), and have been widely detected in the ISM when observations of sufficient sensitivity are made (see Allen et al. 2012, 2013, for early results and a brief historical review). The SPLASH survey (Dawson et al. 2014) using the Parkes telescope pointed towards the inner Galaxy also found widespread OH at all four 18-cm lines, in both emission and absorption. Allen et al. (2015) used the GBT (FWHM $\approx 7.6'$) to carry out a "blind" survey of 18-cm OH emission on a coarse grid of positions in the direction of a quiescent region in the outer Galaxy, with two hours of exposure at each coordinate. Widespread OH emission was detected from both main lines at 1665 and 1667 MHz as well as the 1720 satellite line, though observations of the 1612 satellite line of OH were compromised by radio-frequency interference. Within the sensitivity limit of the observations, the intensities of the two main lines were overwhelmingly in the ratio 5:9 as expected for LTE conditions. Compared to the ^{12}CO(1-0) data from the CfA survey (Dame et al. 2001), many OH features were identified that did not show any corresponding CO emission. All CO features, however, did have corresponding OH emission. A plot of profile integrals of the ^{12}CO features versus those of the corresponding OH features reveals a "bimodal" distribution, with approximately half of the pointings showing little or no ^{12}CO emission, and the remainder displaying a rough correlation

between the strengths of the OH and ^{12}CO lines. The conclusion was that OH traces a significantly larger component of the molecular ISM than does ^{12}CO.

These results suggest that OH observations may provide new insight in other situations where more precise estimates of the quantity and kinematics of molecular gas could shed light on large-scale astrophysical processes. In this paper we use OH as a tool to measure the quantity of H_2 in close proximity to a star forming region, and compare that result with the quantity of H_2 estimated using ^{12}CO emission and the X-Factor.

3.1.2 The W5 Star-forming Region

We chose W5 as a star-forming region to study with a GBT grid survey. As first mentioned in Engelke & Allen (2018), the reasons for this choice are as follows. First, W5 covers an angular size on the sky that is large enough for a grid survey with the GBT to reveal sufficient structural detail while also not requiring an inappropriately-long observing time. Second, there are several radio continuum maps in the literature covering the region, including the Canadian Galactic Plane Survey (CGPS) at 408 and 1420 MHz (Taylor et al. 2003), and a 2695 MHz survey with the Effelsberg telescope (Fürst et al. 1990). A radio continuum study focusing on the W3-W4-W5 complex associated with the CGPS is also available (Normandeau et al. 1997). These surveys show that the continuum temperatures associated with W5 are in the range of excitation temperatures typical for OH in the general ISM, implying that OH in front

of the nebula may appear either in emission or in absorption. This fortunate situation has permitted an accurate measurement of the excitation temperatures for both the 1665 and 1667 OH lines in close proximity to this star-forming region (Engelke & Allen 2018). Finally, W5 is relatively simple in structure; it does not contain large numbers of stars or abundant IR radiation (which is known to lead to enhanced OH emission, complicating the calculation of OH column density) in comparison to other star forming regions (Karr & Martin 2003; Miville-Deschênes & Lagache 2005). While minor peculiar motion is still present, the radial velocity ranges are not large enough to make it difficult to identify W5 features by a kinematic velocity range: -49 km/s to -31 km/s, which we adopt from Karr & Martin (2003).

In order to use an OH survey of W5 to study structure and mass of molecular gas clouds in the region, it is necessary to know the distance to W5. Finding the distance to W5 is not as simple as using kinematic distance calculations based on Galactic rotation models, as anomalous velocities are also involved (Deharving et al. 2012; Xu et al. 2006). OH maser parallax measurements using the Very Long Baseline Array (VLBA) reveal the distance to W3(OH), an OH maser feature within W3, to be 2.00 ± 0.05 kpc (Hachisuka et al. 2006; Xu et al. 2006), as mentioned by Deharving et al. (2012). This measurement could provide a distance to the entire W3-W4-W5 complex if we assume that all three HII regions are a correlated group and are the same distance away. As discussed by Deharving et al. (2012), distances to W4 and W5 have been provided by spectrophotometric measurements of OB clusters IC 1805

in W4 and IC 1848 in W5, both of which are 2.1 to 2.4 kpc (Becker & Fenkart 1971; Chauhan et al. 2009, 2011; Massey et al. 1995; Moffat 1972). These measurements are independent of the VLBI measurement of the distance to W3 and suggest that W3, W4, and W5 are all in close proximity and at the same distance. Deharving et al. (2012) suggest using a value of 2.0 kpc for the distance to W5, which we adopt for this paper.

3.2 Observing Program

3.2.1 The Survey

The goal for the design of our OH survey was to obtain OH column density results from a major part of any molecular clouds located in the direction of W5. In order to study the structure of W5 with sufficient detail while keeping the total observing time within reasonable limits, we chose a representative set of 80 positions covering a large fraction of the radio continuum image of the region. The choice of the specific pointings to observe was primarily informed by the brightness of the radio continuum and by the distribution of ^{12}CO(1-0) emission from the FCRAO survey (Heyer et al. 1998). Figure 3.1 shows the observed positions in our survey superimposed on a map taken from Karr & Martin (2003, their Figure 2) that displays the 1420 MHz continuum emission in gray scale and the integrated CO content in contours.

3.2.2 Observations

The observations for this work were made with the 100-m Robert C. Byrd Green Bank Telescope (GBT) in West Virginia. OH spectra were acquired with the VEGAS spectrometer in the L-band, with 2 hours of exposure per pointing. The system temperature was typically less than 20 K. We used frequency-switching mode because the ubiquitous nature of faint OH emission in the sky means that it is not always possible to find a nearby reference position for position switching (see Allen et al. 2015). We observed all four OH 18-cm transitions at 1612, 1665, 1667, and 1720 MHz, plus the 1420 MHz HI line in dual polarization. The spectrum at each IF band was approximately 12.8 MHz wide, so we were able to observe the 1665 and 1667 MHz lines simultaneously in a single IF band. The FWHM of the GBT point spread function at 1667 MHz is 7.6', and the channel step is 0.515 kHz corresponding to 0.0926 km/s at 1667 MHz. Each 2-hour pointing includes 12 "scans" each of 10 minutes integration. A total of 80 GBT pointings was observed between February 2016 and April 2017 in GBT programs 16A-354 and 17A-386. The maximum spectral dump rate was every 0.5 ms. Radio frequency interference was largely insignificant for the majority of scans at the observed frequencies except for 1612 MHz, which limited the utility of the data at that frequency.

3.2.3 Data Reduction

For data reduction of the two main OH lines near 1666 MHz, we averaged the twelve ten-minute scans for each pointing separately for XX and YY polarizations, excluding any scans containing RFI contamination. Then we averaged together the two polarizations. There is a large-scale baseline ripple of frequency 9 MHz, which is an instrumental effect of the GBT appearing at high sensitivity levels. We fit this baseline with a fifth-degree polynomial in the frequency range 1661.4 MHz to 1671.4 MHz and subtracted the fit from the entire spectrum. This baseline fit does not alter the OH spectral lines themselves because the scale of the baseline ripple is so much larger than the scale of any OH spectral features, and the baseline in the vicinity of spectral features will be defined as zero, as we describe later. Next, we identified the 1665 and 1667 MHz portions of the spectrum and saved the data separately for the two main line frequencies.

Each of the two main lines was then subjected to a final fit to a linear baseline over the immediate velocity range of any OH features visible in the spectrum. For an independent estimate of the velocity range boundaries of any spectral features in W5, we consulted the HI profiles from the Dominion Radio Astrophysical Observatory (DRAO) low resolution survey (Higgs et al. 2005; Higgs & Tapping 2000) in addition to a visual inspection of the OH spectrum. The velocity range of these baseline fits is approximately 10 km/s beyond the left and right edges of the spectral feature. Providing a good fit to the rest of the baseline is not necessary because we are not

concerned with parts of the spectrum located far from the W5 velocity range. Finally, we calculated the strength of each line by summing the signal in spectrometer channels covering the spectral line within the radial velocity range -49 to -31 km/s . The OH observations are of high sensitivity, with typical RMS noise levels of $\sim$ 3 mK, and typical line detections are of $\sim 7\sigma$.

3.3 Calculating Column Densities

3.3.1 OH Column Density Equations

For emission lines, the following equation relates the OH column density to the observed line profile integral $\int T_B(\nu)d\nu$, continuum temperature T_C, and excitation temperature T_{ex}, where temperatures are measured in Kelvins (see e.g. Liszt & Lucas 1996):

$$N(OH) = C\frac{T_{ex}}{T_{ex} - T_C}\int T_b(\nu)d\nu, \tag{3.1}$$

where the coefficient $C_{67} = 2.3 \times 10^{14}$ for 1667 MHz if the resulting N(OH) is to be in terms of cm^{-2}, and $C_{65} = 4.1 \times 10^{14}$ for 1665 MHz, which is 9/5 times the 1667 MHz coefficient.

If the OH lines are observed in absorption, the following equation can be used, where $\tau(\nu)$ is the line optical depth $\tau(\nu) = ln(T_C/(T_C + T_b(\nu))$ (see e.g. Liszt &

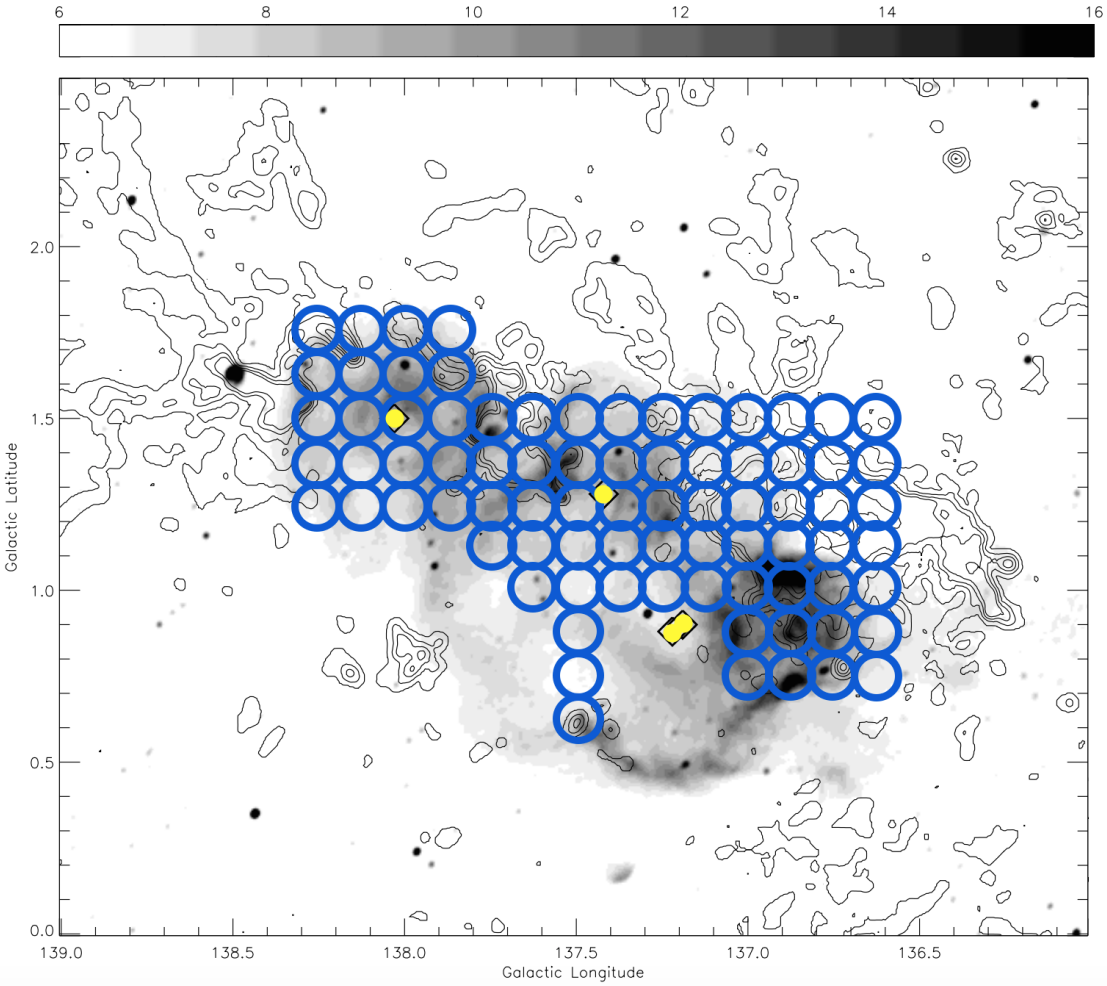

Figure 3.1: Positions of our GBT observations overlaid on the map of the W5 region taken directly from Karr & Martin (2003, Figure 2). The gray scale indicates the 1420 MHz continuum from the CGPS survey (Taylor et al. 2003), the contours indicate ^{12}CO(1-0) emission from the FCRAO survey (Heyer et al. 1998) integrated within the LSR radial velocity range of -49 to -31 km/s, and the 4 diamonds (which we have emphasized in yellow) indicate the locations of known O stars in W5 as plotted by Karr & Martin (2003). We have added a number of blue circles indicating the positions of the GBT pointings in our grid survey; the circle size indicates the $\approx 7.6'$ angular resolution FWHM of the GBT.

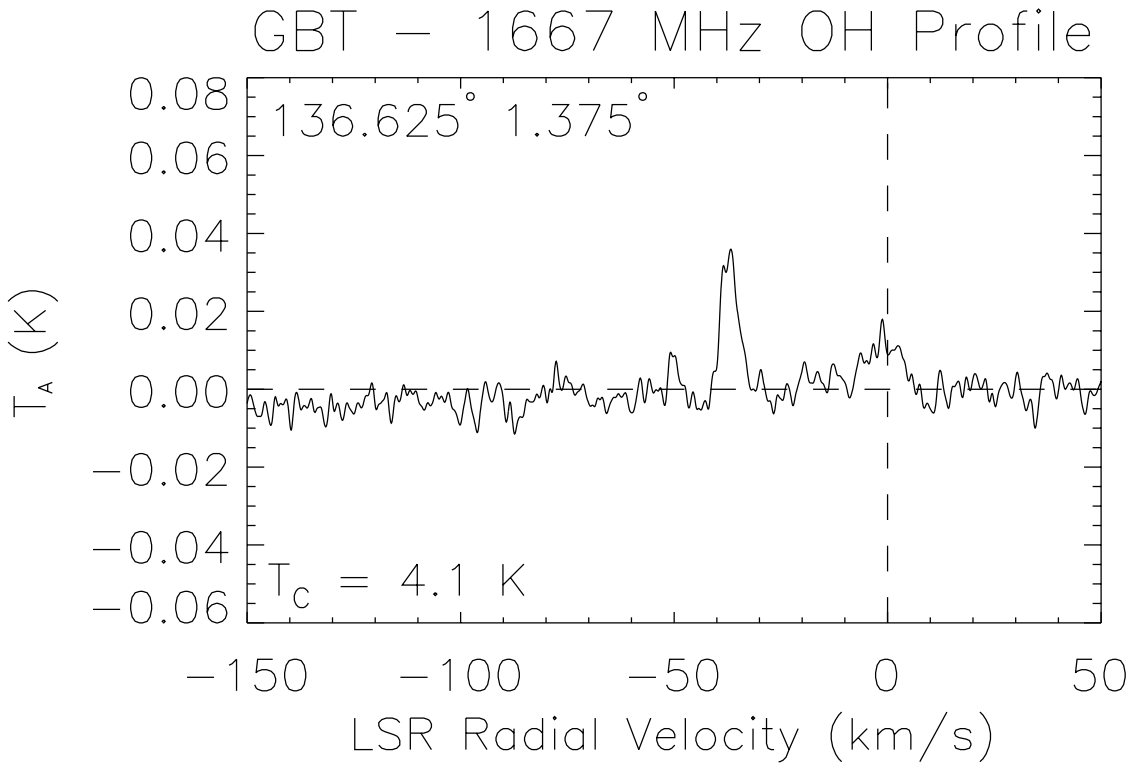

Figure 3.2: Example of a 1667 MHz OH spectrum from the W5 survey. This spectrum was taken at l = 136.625°, b = 1.375° with 2 hours of exposure time on the GBT. We consider any feature detected between -49 km/s and -31 km/s to be associated with W5. In this spectrum, the OH feature associated with W5 is located near -38 km/s. Regions of the baseline measuring 10 km/s on the immediate left and right of the OH feature associated with W5 are fitted to zero.

Lucas 1996):

$$N(OH) = CT_{ex} \int \tau(\nu) d\nu. \tag{3.2}$$

As noted in Engelke & Allen (2018), the majority of spectra from the GBT survey do not show evidence of enhanced OH emission; deviations do occur from the 9:5 main line ratio, but most of these deviations can be explained entirely as a result of the difference in excitation temperatures for the two main lines as measured in Engelke & Allen (2018). All emission features used in our column density analyses meet that criterion.

The GBT observations in the grid survey directly provide the line profile integral for any detected OH signals. When both main line frequencies are detected in emission, we take the mean of the profile integrals to calculate N(OH). However, we must find T_C and T_{ex} by other means.

Since the GBT observations do not provide the continuum temperature, we must calculate what the T_C value would be at 1667 MHz at the position of each GBT observation for a point spread function equivalent to that of the GBT observations. This process is described in Engelke & Allen (2018). We calculate T_C as would be observed at 1667 MHz with a point spread function like that of the GBT observations by interpolating radio continuum survey data at other frequencies (Fürst et al. 1990; Taylor et al. 2003), smoothed to the resolution of the GBT observations. The values of T_C specifically located behind the OH gas are made more precise in certain cases

(see Section 3.7.3).

Determining the excitation temperatures is more complicated and our use of the "continuum background method" to measure T_{ex} from our survey data and T_C values is described in detail in Engelke & Allen (2018) with further constraints discussed in Appendix 3.11. We note that in Engelke & Allen (2018), we found that the main line excitation temperatures have two distinct values, and that it is important in doing column density calculations to use the appropriate values for the corresponding lines.

Since beginning this work, we have become aware of a number of complications regarding the determination of the exact values of the continuum temperatures located behind the OH at 1667 MHz, using the available sources in the literature. We will discuss these complications and a more nuanced analysis of the continuum as part of a future publication. For the time being, however, we note that the method we used to measure the excitation temperature is based on the values we assume for the continuum temperatures, and thus the values of T_{ex} and T_C in our analysis are correlated. Although the exact values of the continuum temperatures and excitation temperatures are not known accurately, the value we use in our analysis of OH emission is the coefficient $T_{ex}/(T_{ex} - T_C)$, which means that any systematic error in our determination of T_C and T_{ex} will largely be irrelevant in our analysis. If our continuum temperature values were inaccurate by a factor A, then our T_{ex} values would be

off by approximately the same factor A. Then the coefficient is

$$\frac{AT_{ex}}{AT_{ex} - AT_C} = \frac{T_{ex}}{T_{ex} - T_C}, \tag{3.3}$$

the implication being that this coefficient will not be influenced by systematic error in T_C and T_{ex} beyond a negligible degree.

Details about the calculations and uncertainties in the column density determinations are provided in Section 3.7.

3.3.2 Total Molecular Gas Column Densities

In order to calculate N(H_2) as traced by OH, we start with our results for N(OH) and then multiply by the OH to H_2 conversion factor based on the abundance ratio for the molecules. Weselak et al. (2010) report an abundance ratio of $1.05 \pm 0.14 \times 10^{-7}$ determined using a combination of archival and new measurements of UV absorption from OH and H_2 in front of several O and B stars, which we adopt in this paper. This result is also consistent with the value of $1.0 \pm 0.2 \times 10^{-7}$ reported by Liszt & Lucas (2002), $\sim 1.3 \times 10^{-7}$, from Rugel et al. (2018), and $\sim 1.0 \times 10^{-7}$ from Nguyen et al. (2018). A thorough summary of the OH to H_2 ratio is provided by Nguyen et al. (2018), who also report that molecular gas content derived from dust reddening from Green et al. (2018) provides a more accurate result than that derived from infra-red data (Planck Collaboration et al. 2014). We follow the dust reddening

method of Nguyen et al. (2018) for measuring the OH to H_2 ratio on our own OH observations as an exercise to test the consistency the ratio in W5 with the values from elsewhere in the literature, using our HI measurements, OH measurements, and dust reddening from Green et al. (2018) as a proxy for total hydrogen nuclei to determine the OH to H_2 ratio. Although our optically thick HI data introduce sufficient uncertainty in the results as to deem them less useful than the Weselak et al. (2010) value, we do show that OH abundances in W5 are consistent with those reported elsewhere in the literature and show no evidence of spatial variation over orders of magnitude. Moreover, variations in OH abundance measured in the literature occur at smaller length scales than our observations resolve. For example, the variation in OH abundance found by Xu et al. (2016) near the edge of the Taurus molecular cloud occurs over a total of 2 pc, with each observation covering a 0.12 pc diameter. Our GBT survey has a resolution corresponding to 4.4 pc. The overall average OH abundance over that larger scale is what is relevant to our work.

Calculations of $N(H_2)$ determined from (1-0) data require use of the X-factor. CO column densities are not directly calculated as in the case of the OH analysis, and instead the CO profile integrals are multiplied by the X-factor to estimate the H_2 column densities. A thorough discussion of the CO X-factor is presented in Bolatto et al. (2013), and we note that finding a single high-precision, widely-applicable value for the X-factor is not realistic, as the X-factor can vary up to an order of magnitude depending on location and conditions. However, Bolatto et al. (2013) recommend

using a value of 2×10^{20} cm^{-2}(K*km/s)$^{-1}$ in the Galactic disk, plus or minus 30%, and we adopt this value for our analysis, while noting that the true uncertainties in molecular gas content derived from CO signals are larger.

The observational data as well as the calculated values for the column densities from both tracers are listed in Table 2.

3.4 Comparing Column Densities from OH and CO

Here we compare column densities of molecular gas as determined from our OH survey and from CO(1-0) data from the FCRAO survey (Heyer et al. 1998) smoothed to the resolution of the GBT survey. We include only features that were detected in emission for at least one of the main line frequencies in our survey, because we find that absorption lines systematically under-predict column densities as compared to emission lines (see Section 3.8).

We plot the data from those positions with N(H_2) as determined from OH on the x axis and N(H_2) as determined from CO(1-0) (Heyer et al. 1998) on the y axis. For 8 out of 15 cases, the OH-derived column densities are greater than the CO-derived column densities within the uncertainties. The OH-derived column densities are greater by a factor up to 7. These data are plotted in red in Figure 3.3. The two molecules trace the same column density within the uncertainties in the other 7

cases, which are plotted in black in Figure 3.3. In no cases containing OH emission detections are the CO-derived column densities greater than the OH-derived column densities within the uncertainty. Note that the results plotted in Figure 3.3 assume a particular uncertainty in the OH to H_2 conversion factor and make use of a standard CO X-factor; true error estimates could be larger than what we assume.

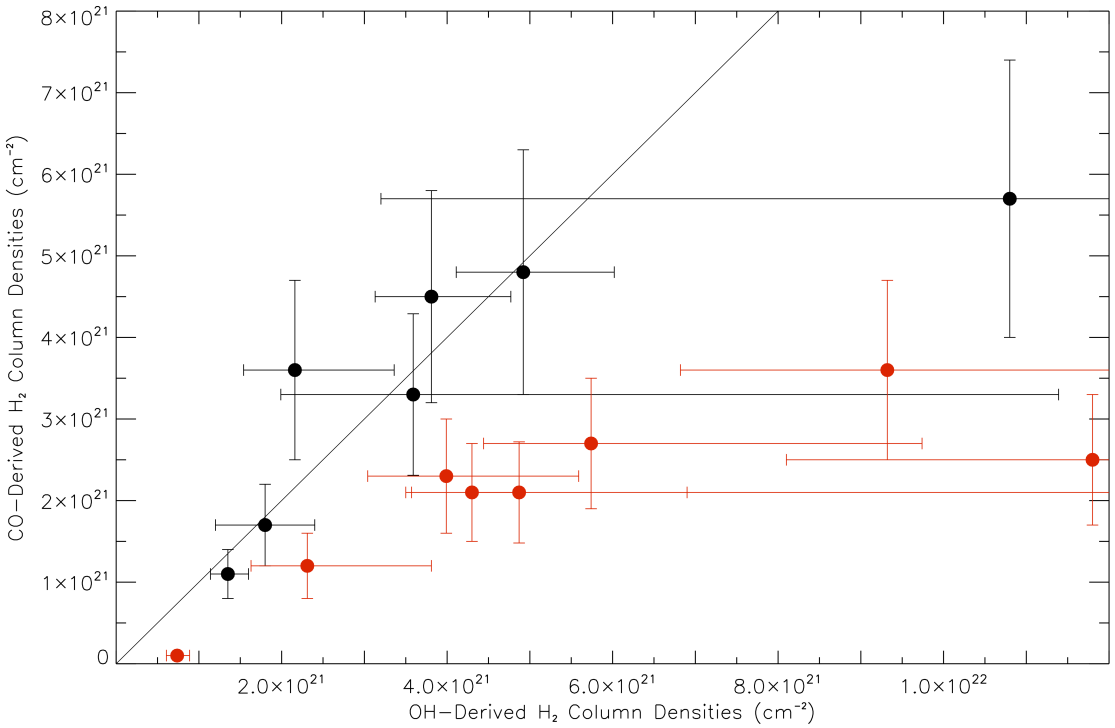

Figure 3.3: Derived column densities of H_2 in W5 for positions within the GBT survey containing OH emission lines at either 1665 MHz or at both main lines using our OH survey data (x axis) and the smoothed FCRAO CO(1-0) data (Heyer et al. 1998) (y axis) as tracers. The superimposed diagonal line represents the y = x relation. In 8 out of 15 cases, the OH traces a larger amount of molecular gas than does the CO; these detections are plotted in red. The CO-derived column densities assume the Bolatto et al. (2013) value for the Galactic disk. The OH-derived column densities assume the OH abundance reported by Weselak et al. (2010). A discussion of assumptions and uncertainties is provided in Sections 3.7.1 and 3.7.4.

3.5 Morphology of Molecular Gas from OH and CO

Positions in the survey containing OH detections in W5 within the radial velocity range are plotted in red on Figure 3.4, which also shows CO(1-0) detections in contours taken directly from Karr & Martin (2003). The morphology of molecular gas near W5 as traced by OH appears to be similar to that traced by CO, even though the column densities derived from the OH detections are in many cases greater than their CO-derived counterparts. All of 44 positions containing OH detections contain CO(1-0) signals, and all but two out of 44 positions containing CO contain OH detections in our survey. The remaining two cases, near the northeast corner of the survey, have T_C near but slightly above T_{ex}, which are equivalent within the uncertainties. As such, they are not true non-detections. These positions most likely contain OH that is not easily detectable due to a switch between emission and absorption within the GBT field of view (see Section 3.8 for an explanation), while the corresponding CO signals are relatively faint and negligible compared to the total gas content of W5.

The CO and OH data both display two major clouds containing molecular gas in our W5 survey region. These clouds do not conform to the classification of an east and west part of the HII region in W5 discussed by Karr & Martin (2003) into W5-E and W5-W. Rather, the molecular gas according to both tracers contains a large cloud on the west side of W5 that extends beyond the W5 continuum to the

north and west, and a smaller cloud closer to the eastern end of the W5 continuum, located near the boundary between W5-E and W5-W. The edge of another cloud extending outside of W5 exists at the easternmost boundary of the survey. There are voids containing no molecular gas detections near the centers of W5-E and W5-W, most likely resulting from ionization and wind produced by the O and B stars in the centers of those regions (see Figure 3.4).

3.6 Mass Estimates of Molecular Gas from OH and CO

We obtain mass estimates of molecular gas in the survey region from our column density data. However, more than half of the OH detections manifest as absorption lines, which are not suitable for inclusion in the mass estimate because they systematically under-predict column densities (see Section 3.8). Thus we only perform mass estimates where there is a usable OH emission detection at at least one main line frequency. Fifteen out of 42 pointings ($\sim 36\%$) with OH detections meet this criterion and are included in the mass estimate.

To estimate mass, we find the column density in each pixel in the survey containing an OH emission detection at either of the main line frequencies, and calculate the mass that would fit within each pixel if the majority of molecular gas particles are H_2 molecules at the distance to W5 of 2 kpc. Then we sum all of those pixels to find

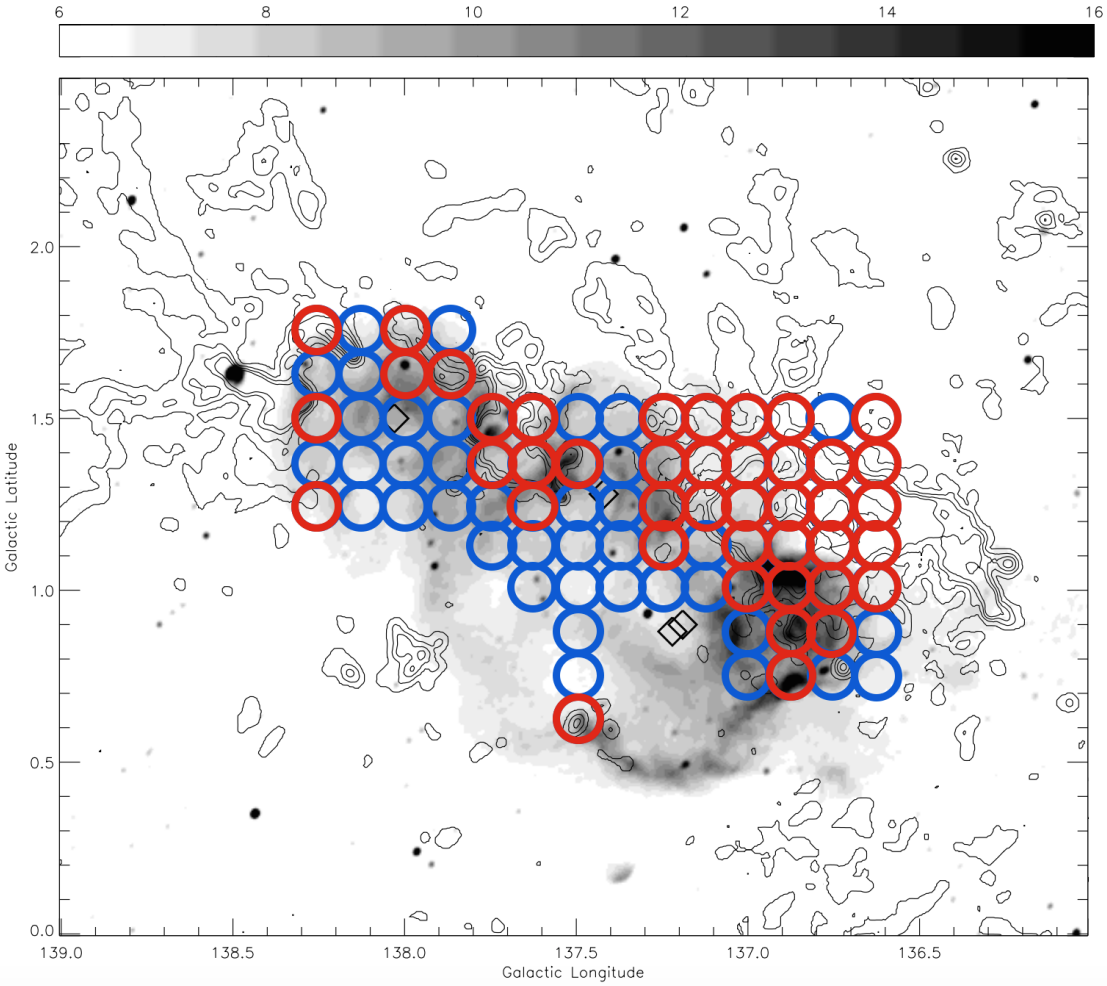

Figure 3.4: Positions of our our OH detections in the LSR radial velocity range -49 to -31 km/s in red, and positions of observations without detections in blue, overlaid on the map of the W5 region taken directly from Karr & Martin (2003, Figure 2). The gray scale indicates the 1420 MHz continuum from the CGPS survey (Taylor et al. 2003), the contours indicate ^{12}CO(1-0) emission from the FCRAO survey (Heyer et al. 1998) integrated within the LSR radial velocity range of -49 to -31 km/s, and the 4 diamonds indicate the locations of known O stars in W5 as plotted by Karr & Martin (2003). The circle size representing our observations indicates the $\approx$ 76 angular resolution FWHM of the GBT.

the mass of molecular gas in the portion of W5 being studied.

For the subset of the positions that contain OH emission detections in some form, we calculate a total mass of $1.7 \times 10^4 M_\odot$ + $0.6 \times 10^4 M_\odot$ or - $0.2 \times 10^4 M_\odot$. The corresponding CO data gives a total mass of $9.9 \times 10^3 M_\odot \pm 0.7 \times 10^3 M_\odot$.

Since fewer than half of the pointings containing OH detections at W5 radial velocities are able to be used in the mass estimate, the total mass in W5 could be roughly two to three times the mass that we calculated from column densities derived from OH emission lines.

3.7 Calculations and Uncertainties

3.7.1 Unknowns Involved

Here we consider the details, uncertainties, and assumptions in calculating N(OH) and N(H_2) for the simpler case of emission. First, we must assume a value of T_C in the background of any OH gas when calculating column densities from observations. The line of sight position of the OH feature and any uncertainty in that position are relevant because T_C depends on the position of the gas relative to the source of the continuum.

Second, the signal being measured is in fact the weighted integral of $\int T_b(\nu) d\nu$ over the GBT point spread function. Therefore, any high-resolution spatial variation of the signal within the telescope field of view cannot be detected and is an unknown

quantity. If the T_{ex} and T_C values were constant over the telescope beam, there would be no problem, but T_C at least certainly varies spatially at high resolution compared to the GBT point spread function. While T_{ex} in principle could vary as well, our results in Engelke & Allen (2018) show no evidence of variation in T_{ex} at scales comparable to the GBT point spread function above the uncertainty. Variation in T_C poses a considerable problem, because N(OH) as well as T_C can both vary within the GBT beam. The resulting spectral signal, which is the integral of $\int T_b(\nu)d\nu$ over the point spread function, depends on how the distributions of N(OH) and T_C overlap. Methods for addressing these unknowns and mitigating them when possible are discussed in Sections 3.7.2 and 3.7.3.

Lastly, we must point out that we are assuming the Weselak et al. (2010) value for the OH to H_2 ratio in W5 despite the fact that this value was not measured in W5. Although we have demonstrated in Section 3.3.2 that it is a reasonable value, it is important to remember that this value is nevertheless an assumption.

3.7.2 Line of Sight Geometry

Much of our analysis of the OH line profiles and calculations of excitation temperatures and column densities assumes that the OH gas is located in the foreground of the W5 continuum source. Naturally, not all of the OH in the vicinity of W5 will be located in the foreground. A good starting point is to assume that most of the OH will be either in the foreground or the background of the W5 HII region, because OH

gas located in the midst of the HII region would be photo-dissociated and ionized (e.g. Anderson et al. 2009). This may not in fact be entirely true, as we shall see, because a clumpy and irregularly shaped HII region may allow for pockets of molecular gas to exist partway through the HII region continuum source along the line of sight.

For the majority of positions in the survey at which OH was detected, it appears that there is OH in the foreground. This finding is clear for examples at which OH absorption was detected at either main line frequency since we know that T_{ex} is not low enough to allow for OH absorption when the W5 continuum is not in the background. There are also positions detected in emission at both main line frequencies at which evidence implies that the OH is located in the foreground. This evidence comes from examining the line ratios, the T_C values, and the T_{ex} values. Main line emission profile integral ratios departing from 5:9 could be a result of the fact that $T_{ex}^{65} > T_{ex}^{67}$. As described in Engelke & Allen (2018), our observed gradient of line ratio departures from 5:9 over the northwest part of the survey are consistent with a model for which the OH is in the foreground.

At several positions, there is evidence of OH in both the foreground and the background of the W5 continuum. This type of spectrum manifests as an emission line and an absorption line next to each other or even overlapping slightly, creating a complicated spectrum. Radial velocities and widths of the lines tend to vary enough within different parts of the survey that a perfect overlap, which would be difficult to separate, is unlikely. In cases containing OH in the foreground as well as the

background, we choose to include only the foreground features in our study to simplify the analysis, as T_C and T_{ex} values are known more accurately.

That accounts for all of the OH features used in our analysis, but there are two remaining cases evidenced in the survey. At a few positions in the eastern portion of the survey, we find that the OH is detected in emission at both main line frequencies at the 5:9 ratio, despite the fact that T_C at that position is is above the excitation temperature for both main lines. If the gas were in the foreground of the continuum, both lines would have been detected in absorption. Instead, we suppose that the gas is located entirely in the background, so that the value of T_C behind the gas is much lower.

There are three adjacent positions in the survey with evidence of OH located somewhere in the midst of the continuum along the line of sight. These positions contain absorption detections at 1667 MHz and no OH detection at 1665 MHz. This finding would imply that T_C behind the OH at those positions is equal to the T_{ex} at 1665 MHz. However, the T_C values at those positions are greater than that value. Our proposed explanation is that these are cases for which OH is located in a shielded pocket within the HII region producing the W5 continuum, neither in the foreground nor in the background. It is unlikely that T_{ex} variation could explain these spectra because those three positions are adjacent and yet would have T_{ex}^{65} values varying significantly more than T_{ex} was found to vary in Engelke & Allen (2018).

3.7.3 Effects of Structure Inside GBT Beam for Emission Lines

In Section 3.7.1, we described how the observed emission spectrum at a given position depends not simply on the beam-averaged values of N(OH) and T_C, but on the high resolution spatial distributions of N(OH) and T_C within the GBT field of view, and how those distributions overlap.

Thus, the relevant value to insert in Equation 3.1 is not the beam-averaged value of T_C, but rather the average value of T_C convolved with distribution of N(OH) within the GBT beam, which we call $T_C^{optimal}$.

We propose a method to determine $T_C^{optimal}$ for a subset of observations. For the rest, we will estimate the uncertainty posed by using the beam-averaged T_C instead of the unknown $T_C^{optimal}$. There are several positions in our survey at which OH emission was detected at both main line frequencies. These cases allow us to compare the column densities calculated independently from the two main lines at the same position in the sky. If the T_{ex} and T_C input parameters are correct, then the two main lines at the same position should yield equal column density results, within the statistical uncertainty. However, in general, there is some scatter in the column density comparison when the measured T_{ex} values (see Engelke & Allen (2018); Appendix 3.11) and the beam-averaged T_C are used as input parameters, as seen in Figure 3.5.

To find $T_C^{optimal}$ for these positions, we begin by assuming the T_{ex} values as given.

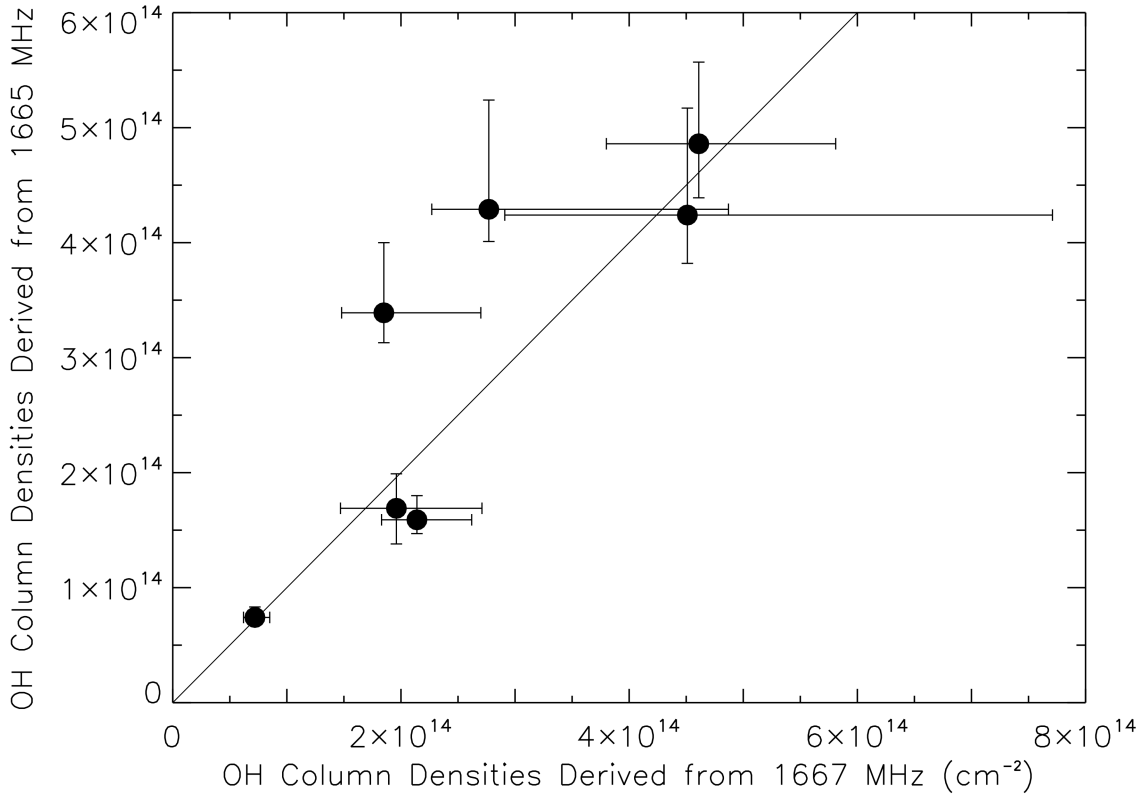

Figure 3.5: Column densities of OH as calculated from the 1667 MHz OH emission profiles compared to the OH column densities for the same positions as calculated from the 1665 MHz OH emission profiles for all observed cases in which both 1665 MHz and 1667 MHz contain emission profiles within the W5 radial velocity range. A diagonal y = x line is superimposed to indicate where the column densities as calculated from 1665 MHz and from 1667 MHz emission lines are the same. The error bars contain uncertainties in the profile integrals, continuum temperature, and the excitation temperature values from Engelke & Allen (2018). The plot demonstrates that the 1665 MHz and 1667 MHz emission lines yield generally consistent column density results when the two different values for the main line excitation temperatures are taken into account.

Then we can write Equation 3.1 for both 1665 MHz and for 1667 MHz at the same position, and set the equations equal to each other, with the goal of solving for $T_C^{optimal}$:

$$N(OH) = C_{65}\frac{T_{ex}^{65}}{T_{ex}^{65} - T_C^{optimal}} \int T_b^{65}(\nu)d\nu$$

$$= C_{67}\frac{T_{ex}^{67}}{T_{ex}^{67} - T_C^{optimal}} \int T_b^{67}(\nu)d\nu. \quad (3.4)$$

A similar line of reasoning leads to a method to constrain the excitation temperature values, as described in Section 3.11. These values are $T_{ex}^{65} = 5.87 + 0.43$ or - 0.37 K, and $T_{ex}^{67} = 5.13 + 0.17$ or - 0.22 K, though these values could still be subject to systematic error.

For the emission detections at 1665 MHz that do not contain corresponding emission at 1667 MHz, it is not possible to determine $T_C^{optimal}$, so we assume the beam-averaged T_C. To estimate this contribution to the uncertainty in N(OH), we implement Equation 3.1 with the minimum and maximum values of T_C within the GBT field of view at the CGPS resolution, scaling for 1-σ uncertainties.

3.7.4 Summary of Error Sources

Here we summarize the four error sources in N(H_2) calculated from OH emission observations. First, there is the statistical noise uncertainty in the profile integral measurements from the GBT. Second, there is uncertainty in the coefficient $\frac{T_{ex}}{T_{ex}-T_C}$. Recall from Section 3.1 that although there may be systematic error in our determi-

nation of T_C and T_{ex}, the systematic error largely cancels out when the coefficient is calculated. Therefore, the primary error sources in the coefficient come from the uncertainty in T_{ex} described in Appendix, Section 7.3, and the following two forms of uncertainty in T_C. Low level variations in the actual value of T_{ex} are possible over the cloud, though these variations are unlikely to be large, meaning that theoretically there could be another source of error in the calculations. Modeling of possible variation in excitation temperature will be described in a future publication. Third, there is uncertainty in T_C, which can come in two forms. For observations containing emission at both main line frequencies, an improved accuracy $T_C^{optimal}$, resulting from variation within the GBT beam of both N(OH) and T_C distributions, can be calculated as described in Section 3.7.3. The uncertainty in $T_C^{optimal}$ depends on the precision to which $T_C^{optimal}$ could be determined as constrained by uncertainty in the profile integrals and T_{ex}. For spectra containing emission only at 1665 MHz, $T_C^{optimal}$ cannot be calculated, and the resulting uncertainty in T_C is discussed in Section 3.7.3. Fourth, there is uncertainty in the conversion from N(OH) to N(H_2) provided by Weselak et al. (2010).

For corresponding CO-derived N(H_2) values, there are two sources of uncertainty: the statistical noise uncertainty in the CO profile integrals from the smoothed FCRAO survey data (Heyer et al. 1998), and the uncertainty in the value of the X-factor for gas within the Galactic disk, which is provided by Bolatto et al. (2013).

3.8 Discrepancies with Absorption Line Column Densities

We have not used spectra detected in absorption in our column density calculations. Here, we examine a subset of spectra that contain absorption at 1667 MHz and emission at 1665 MHz, and compare N(OH) as calculated from those two lines at each position. There are five such examples in the survey data.

We apply Equation 3.1 for the 1665 MHz emission line and Equation 3.2 for the 1667 MHz absorption line, with the appropriate coefficients for the respective line frequencies. The result is that the absorption line yields a column density one to two orders of magnitude lower than does the emission line. The absorption-derived column densities appear more likely to be the inaccurate ones, because the emission-derived column densities are mostly at the same order of magnitude as corresponding CO-derived column densities even though they are sometimes greater by a factor between 1 and 10. On the other hand, the absorption-derived column densities are always at least one order of magnitude below the CO-derived equivalents and sometimes more. Apparently, the absorption lines in our survey systematically under-predict the column densities by a factor of 10 to 100, as seen in Table 3.1.

We propose that absorption lines systematically under-predict the column density as compared to emission lines because two conditions must be met for an absorption line to occur: there must be OH present to absorb, and there must be a sufficiently

Table 3.1: OH Column densities as calculated from absorption at 1667 MHz and emission at 1665 MHz at the same coordinates

l	b	1667 Abs. N(OH) (cm^{-2})	1665 Em. N(OH) (cm^{-2})	Ratio
136.875	1.25	8.5×10^{12}	2.3×10^{14}	0.037
137.0	1.25	1.3×10^{13}	1.1×10^{15}	0.011
137.0	1.375	1.2×10^{13}	9.8×10^{14}	0.012
137.125	1.25	8.5×10^{12}	9.7×10^{14}	0.0089

strong background continuum present to be absorbed. Only where these two conditions overlap does absorption occur, and only the fraction of OH that overlaps with sufficiently strong continuum temperatures will be detected.

We have already established in Sections 3.7.1 and 3.7.3 that OH probably covers just a fraction of the GBT field of view. There is much evidence in the literature to support this claim. HI absorption interferometry observations have provided evidence of small-scale structure and variation in opacity from parsec scale down to a few AU (Brogan et al. 2005; Deshpande 2000; Faison & Goss 2001; Frail et al. 1994; Goss et al. 2008; Roy et al. 2010, 2012). Comparison to single-dish observations, moreover, suggests that the observed variation in opacities cannot result from variation in spin temperature and more likely results from structural variation (Brogan et al. 2005). There is also evidence of small-scale variational structure and clumpiness in molecular gas from absorption interferometry observations of H_2CO found by Goss et al. (1984); Reynoso & Goss (2002) in front of Cas A, and Marscher et al. (1993); Moore & Marscher (1995) in front of 3C111, BL Lac, and NRAO 150. In OH absorption, Bieging & Crutcher (1986) found similar structure in front of Cas A. These studies

all indicate the likelihood that the OH filling factor is low; filling factors of about 10 percent have been found at small scales for HI (Brogan et al. 2005) and could plausibly be similar or even smaller for OH. The small scale variation and clumping of OH, combined with higher resolution structure of the background continuum which can be viewed in the CGPS 1420 MHz continuum maps (Taylor et al. 2003), suggest that absorption will only occur for a fraction of the OH within a GBT field of view even if the beam averaged T_C is greater than T_{ex}. The result would be that absorption lines will systematically underestimate N(OH), just as we find in our data.

Additionally, OH from portions of the GBT field of view containing lower T_C values may exhibit OH emission profiles, despite the beam-averaged T_C being greater than T_{ex}. These emission components may not dominate the beam-averaged spectrum, but can diminish the strength of the absorption profile in the beam-averaged spectrum.

Thus there are two main reasons why absorption profiles will under-predict the column densities of OH: they only account for a fraction of the OH that is present, and the remaining OH may further reduce the signal strength by adding emission profiles on top of it.

In order to test the plausibility of these arguments, we create a simulation containing filaments of OH and independent variation of elevated continuum temperature over a square telescope beam, and calculate what the detected line profile would be at each pixel within the square. We calculate the total beam-averaged predicted line profile by averaging the results from all of the pixels, and we calculate the beam-averaged

T_C as well. Next, we compare the column density calculated from the beam-averaged predicted spectrum to the input column density value used in the simulation. We perform this simulation several times while varying the input parameters for the model. For a given beam-averaged column density of OH, the predicted detection results in lower OH column densities, which can be one to two orders of magnitude less for certain input parameter values, comparable to the observed results. Although the true telescope beam is not square, the difference in the model would be negligible. We conclude that our explanation for the reduced values of OH column densities calculated from absorption lines is plausible. A diagram of the model is shown in Figure 3.6.

For the two positions in the northeast corner of the survey where faint CO is detected without a corresponding OH detection, beam-averaged T_C values are just slightly above T_{ex} and T_C varies above and below T_{ex} within the field of view. At these two positions, we suggest that the OH absorption spectrum is so diminished in this way as to be undetectable above the noise level.

Future interferometry observations of OH 18-cm absorption at these positions could provide the data needed to accurately calculate column densities. Currently, we do not have this data, and owing to differences in structure at each position, there does not appear to be a way to correct for the column density discrepancies without introducing overwhelming uncertainties.

However, this exercise does allow us to estimate the size of the OH filling factors

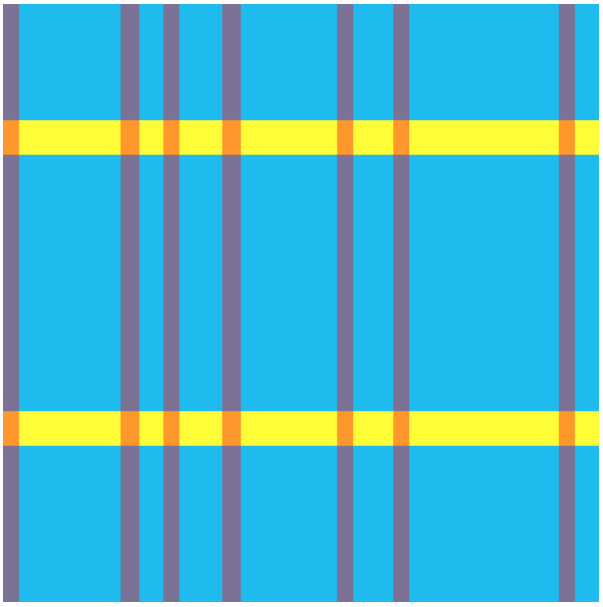

Figure 3.6: Diagram of the type of model used to simulate the effects of high resolution spatial structure of OH and T_C on resulting beam-averaged spectra. The blue regions represent relatively low values of T_C and N(OH), red regions represent higher values of T_C, and yellow regions represent higher values of N(OH). Absorption profiles occur at pixels containing an overlap of red and yellow regions, which only includes a fraction of the total OH content in the model. Moreover, pixels in the yellow regions containing high OH content but lower T_C values produce emission profiles, which contribute to the beam-averaged spectrum along with the absorption profiles from the overlapping red and yellow regions. The net effect is a beam-averaged absorption profile that predicts a lower value of beam-averaged N(OH) than is truly present in the model. This diagram does not necessarily display the ratios of blue, red, and yellow regions that produced results comparable to our measurements, but is simply intended to illustrate the model generally.

for these observations. The filling factor is probably roughly a few to 10 percent and varies between the observations.

We note that just as it is possible for absorption profiles to be mixed with some emission profiles when $T_C \approx T_{ex}$, it is also possible for emission profiles to be mixed with some absorption profiles when $T_C \approx T_{ex}$. Therefore, a few of the column densities calculated from emission lines may be lower limits on the true column density values.

3.9 Discussion

The results presented in this paper as well as past studies (e.g. Allen et al. 2015; Nguyen et al. 2018) imply that OH is a viable tracer for interstellar molecular gas. Although our results suggest that OH might trace more molecular gas in W5 than does CO, additional uncertainties regarding the CO X-factor and the OH abundance prevent the results from providing conclusive evidence for the presence of CO-dark molecular gas in W5. In any case, no position in the W5 survey containing OH is entirely CO-dark. The nearly one-to-one correspondence between OH and CO distributions in the W5 survey differs from the results found by Allen et al. (2015) for a quiescent region centered on $l = 105.0°$, $b = 1°$, where fewer than half of positions with OH detections contained CO counterparts detected in the Dame et al. (2001) CO data. Thus we do find conclusive evidence of CO-dark molecular gas in that quiescent region. One possible explanation for this difference could be as follows. The CO(1-0) signal only appears when the gas exceeds a critical volume density. Turbulence in the W5 star-forming region could lead to the formation of dense concentrations in portions of the molecular gas clouds, which may not be common in the quiescent region.

3.10 Conclusions

Our goal was to study the molecular gas content in a star-forming region using OH 18-cm lines as a tracer, and to compare it to the view as traced by CO(1-0). We calculated column densities of molecular gas in W5 using a GBT OH 18-cm main line grid survey of W5. From this survey, we conclude that OH traces a similar morphology of molecular gas as does CO near W5. At positions where at least one main line frequency is observed in emission, OH traces $1.7 \times 10^4 M_\odot$ ($+ 0.6 \times 10^4 M_\odot$ or - $0.2 \times 10^4 M_\odot$) of molecular gas, whereas CO traces $9.9 \times 10^3 M_\odot \pm 0.7 \times 10^3$.

During the course of the project, we also determined that the OH absorption lines in our survey systematically underestimate the column densities by 1 to 2 orders of magnitude. We are able to explain the this discrepancy by considering the extent to which the OH filling factor overlaps with areas of elevated continuum temperature, and modeling suggests an OH filling factor of a few to 10 percent for the survey region. Future interferometry observations could remove this discrepancy by providing higher spatial resolution OH absorption spectra. The total molecular gas content of W5 is probably about two to three times our reported mass estimates because only 36% of the OH detections contained emission lines and were used in the mass calculations.

3.11 Appendix: Further Constraints on Excitation Temperatures

The filling factor analysis in Section 3.7.3 assumed the excitation temperature values as input parameters, but it also provides a way to further constrain their values. In Engelke & Allen (2018), we measured the excitation temperatures to be $T_{ex}^{65} = 6.0 \pm 0.5$ K, $T_{ex}^{67} = 5.1 \pm 0.2$ K, and $T_{ex}^{65} - T_{ex}^{67} = 0.9 \pm 0.5$ K. If instead of using the Engelke & Allen (2018) excitation temperature values as inputs, we were to choose an arbitrary pair of values for T_{ex}^{65} and T_{ex}^{67}, then a different value of T_C would result. However, not any arbitrary value of T_C is physically possible. There is a range of T_C values that exists within the field of view of a given GBT observation, and only solutions for T_C that exist between the minimum and maximum value of T_C within the GBT field of view are possible solutions. Therefore, any combination of input T_{ex} values that leads to a solution for T_C outside of the extrema for that observation can be ruled out. We can use this principle to set up a system of inequalities, one for the maximum T_C and one for the minimum T_C for each observation containing OH emission at both main line frequencies. The solution of the system of inequalities is the phase space of possible values of T_{ex}^{65} and T_{ex}^{67}. Since the system of inequalities involved five observations covering an angular region of W5 greater than a single GBT point spread function, any potential low level variation in T_{ex} at that scale is still incorporated within the uncertainties on the new constrained values. We have

therefore constrained the values of T_{ex} in W5 to

$T_{ex}^{65} = 5.87$ (+ 0.43 or - 0.37) K,

$T_{ex}^{67} = 5.13$ (+ 0.17 or - 0.23) K, and

$T_{ex}^{65} - T_{ex}^{67} = 0.74$ + (0.26 or - 0.22) K.

These values are an improvement in precision over the Engelke & Allen (2018) values although the value of T_{ex} depends on our assumed T_C values and as such could be subject to systematic error.

l	b	1665 MHz (K km s^{-1} or τ)	1667 MHz (K km s^{-1} or τ)	$\frac{T_{ex}}{T_{ex}-T_C}$	N(OH) (cm^{-2})	^{12}CO Profile Integral (K km s^{-1})	N(H$_2$)$_{OH}$ (cm^{-2})	N(H$_2$)$_{CO}$ (cm^{-2})
136.°625	0.°750	···	···	65: >9	no upper limit	···	no upper limit	$<2 \times 10^{20}$
136.°625	0.°875	···	···	abs.	($<4 \times 10^{12}$)	···	($<4 \times 10^{19}$)	$<2 \times 10^{20}$
136.°625	1.°000	$\tau = 0.002 \pm 0.002$	$\tau = 0.007 \pm 0.002$	abs.	(6.6×10^{12})	6.2 ± 0.1	(6.2×10^{19})	$1.2 \times 10^{21} \pm 4 \times 10^{20}$
136.°625	1.°125	0.239 ± 0.003	0.241 ± 0.003	67: 7.2 $\pm$ 0.1	$4.01 \times 10^{14} + 8.5 \times 10^{13}$ or -4.6×10^{13}	22.2 ± 0.1	$3.81 \times 10^{21} + 9.6 \times 10^{20}$ or -6.8×10^{20}	$4.5 \times 10^{21} \pm 1.3 \times 10^{21}$
136.°625	1.°250	0.334 ± 0.003	0.363 ± 0.003	67: 6.2 $\pm$ 0.1	$5.17 \times 10^{14} + 8.5 \times 10^{13}$ or -4.7×10^{13}	24.2 ± 0.1	$4.92 \times 10^{21} + 1.1 \times 10^{21}$ or -8.1×10^{20}	$4.8 \times 10^{21} \pm 1.5 \times 10^{21}$
136.°625	1.°375	0.116 ± 0.003	0.187 ± 0.003	67: 5.0 $\pm$ 0.5	$1.9 \times 10^{14} \pm 5 \times 10^{13}$	8.3 ± 0.2	$1.8 \times 10^{21} \pm 6 \times 10^{20}$	$1.7 \times 10^{21} \pm 5 \times 10^{20}$
136.°625	1.°500	0.057 ± 0.003	0.069 ± 0.002	67: 4.9 $\pm$ 0.5	$7.75 \times 10^{13} + 1.1 \times 10^{13}$ or -9.0×10^{12}	0.5 ± 0.1	$7.37 \times 10^{20} + 1.5 \times 10^{20}$ or -1.3×10^{20}	$1.0 \times 10^{20} \pm 3.6 \times 10^{19}$
136.°750	0.°750	···	···	abs.	$<4 \times 10^{14}$	···	$<4 \times 10^{21}$	$<2 \times 10^{20}$
136.°750	0.°875	$\tau = 0.015 \pm 0.002$	$\tau = 0.017 \pm 0.002$	abs.	(2.8×10^{13})	4.8 ± 0.2	(2.7×10^{20})	$9.6 \times 10^{20} \pm 2.9 \times 10^{20}$
136.°750	1.°000	$\tau = 0.037 \pm 0.002$	$\tau = 0.059 \pm 0.002$	abs.	(8.0×10^{13})	16.4 ± 0.1	(7.6×10^{20})	$3.3 \times 10^{21} \pm 9.8 \times 10^{20}$
136.°750	1.°125	0.073 ± 0.003	···	65: 12 + 25 or -6	$3.77 \times 10^{14} + 8.0 \times 10^{14}$ or -1.6×10^{14}	16.4 ± 0.2	$3.59 \times 10^{21} + 7.8 \times 10^{21}$ or -1.6×10^{21}	$3.3 \times 10^{21} \pm 9.9 \times 10^{20}$
136.°750	1.°250	0.219 ± 0.003	0.130 ± 0.003	67: 17 $\pm$ 0.7	$5.12 \times 10^{14} + 7.7 \times 10^{14}$ or -1.2×10^{14}	10.3 ± 0.2	$4.87 \times 10^{21} + 7.3 \times 10^{21}$ or -1.3×10^{21}	$2.1 \times 10^{21} \pm 6.2 \times 10^{20}$
136.°750	1.°375	0.277 ± 0.003	0.195 ± 0.003	67: 13.5 $\pm$ 0.4	$6.03 \times 10^{14} + 4.1 \times 10^{14}$ or -1.1×10^{14}	13.6 ± 0.2	$5.74 \times 10^{21} + 4.0 \times 10^{21}$ or -1.3×10^{21}	$2.7 \times 10^{21} \pm 8.0 \times 10^{20}$
136.°750	1.°500	···	···	67: 5.5 + 1.5 or -0.5	$< 6 \times 10^{12}$	···	$< 6 \times 10^{19}$	$<2 \times 10^{20}$
136.°875	0.°750	$\tau = 0.004 \pm 0.002$	$\tau = 0.008 \pm 0.002$	abs.	(9.6×10^{12})	1.2 ± 0.2	(9.1×10^{19})	$2.4 \times 10^{20} \pm 8 \times 10^{19}$
136.°875	0.°875	$\tau = 0.023 \pm 0.002$	$\tau = 0.035 \pm 0.002$	abs.	(4.9×10^{13})	9.2 ± 0.2	(4.6×10^{20})	$1.8 \times 10^{21} \pm 6 \times 10^{20}$
136.°875	1.°000	$\tau = 0.054 \pm 0.002$	$\tau = 0.097 \pm 0.002$	abs.	(1.2×10^{14})	24.8 ± 0.2	(1.2×10^{21})	$5.0 \times 10^{21} \pm 1.5 \times 10^{21}$
136.°875	1.°125	$\tau = 0.050 \pm 0.002$	$\tau = 0.083 \pm 0.002$	abs.	(1.1×10^{14})	57.4 ± 0.2	(1.0×10^{21}	$1.1 \times 10^{22} \pm 3 \times 10^{21}$
136.°875	1.°250	0.052 ± 0.002 and $\tau = 0.007 \pm 0.002$	0.072 ± 0.003	65: 7.6 + 5 or -2	$2.27 \times 10^{14} + 1.2 \times 10^{14}$ or -5.7×10^{13}	18.1 ± 0.2	$2.16 \times 10^{21} + 1.2 \times 10^{21}$ or -6.2×10^{20}	$3.6 \times 10^{21} \pm 1.1 \times 10^{21}$
136.°875	1.°375	0.17 ± 0.003	···	65: 6 + 6 or -2	$4.26 \times 10^{14} + 2.8 \times 10^{14}$ or -8.3×10^{13}	10.6 ± 0.2	$4.3 \times 10^{21} + 2.6 \times 10^{21}$ or -8×10^{20}	$2.1 \times 10^{21} \pm 6 \times 10^{20}$
136.°875	1.°500	0.102 ± 0.003	0.121 ± 0.003	67: 5.0 $\pm$ 0.5	$1.42 \times 10^{14} + 1.8 \times 10^{13}$ or -1.1×10^{13}	5.5 ± 0.2	$1.35 \times 10^{21} + 2.5 \times 10^{20}$ or -2.1×10^{20}	$1.1 \times 10^{21} \pm 3 \times 10^{20}$
137.°000	0.°750	···	···	abs.	($<4 \times 10^{12}$)	···	(7×10^{19})	$<2 \times 10^{20}$
137.°000	0.°875	···	···	abs.	($<4 \times 10^{12}$)	···	($<7 \times 10^{19}$)	$<2 \times 10^{20}$
137.°000	1.°000	$\tau = 0.0231 \pm 0.002$	$\tau = 0.0364 \pm 0.002$	abs.	(4.9×10^{13})	3.8 ± 0.2	(4.7×10^{20})	$7.6 \times 10^{20} \pm 2.3 \times 10^{20}$
137.°000	1.°125	$\tau = 0.0464 \pm 0.003$	$\tau = 0.0113 \pm 0.002$	abs.	(6.2×10^{13})	26.6 ± 0.2	(5.9×10^{20})	$5.3 \times 10^{21} \pm 1.6 \times 10^{21}$
137.°000	1.°250	0.079 ± 0.003	$\tau = 0.0108 \pm 0.002$	65: 35 + 60 or -20	$1.13 \times 10^{15} + 1.9 \times 10^{15}$ or -7.8×10^{14}	28.7 ± 0.2	$1.08 \times 10^{22} + 1.8 \times 10^{22}$ or -7.6×10^{21}	$5.7 \times 10^{21} \pm 1.7 \times 10^{21}$
137.°000	1.°375	0.27 ± 0.003	0.0309 ± 0.002 and $\tau = 0.01 \pm 0.002$	65: 8.8 + 3.7 or -0.8	$9.79 \times 10^{14} + 6.4 \times 10^{14}$ or -2.3×10^{14}	17.8 ± 0.2	$9.32 \times 10^{21} + 6.2 \times 10^{21}$ or -2.5×10^{21}	$3.6 \times 10^{21} \pm 1.1 \times 10^{21}$

l	b	1665 MHz (K km s^{-1} or τ)	1667 MHz (K km s^{-1} or τ)	$\frac{T_{ex}}{T_{ex}-T_C}$	N(OH) (cm^{-2})	^{12}CO Profile Integral (K km s^{-1})	N(H$_2$)$_{OH}$ (cm^{-2})	N(H$_2$)$_{CO}$ (cm^{-2})
137.000	1.500	0.15 ± 0.003	···	65: 6.7 + 2 or −0.7	$4.19 \times 10^{14} + 1.6 \times 10^{14}$ or -8.2×10^{13}	11.6 ± 0.1	$3.99 \times 10^{21} + 1.6 \times 10^{21}$ or -9.5×10^{20}	$2.3 \times 10^{21} \pm 7 \times 10^{20}$
137.125	1.000	···	···	abs.	($<4 \times 10^{12}$)	···	($<7 \times 10^{19}$)	$<2 \times 10^{20}$
137.125	1.125	···	···	abs.	($<4 \times 10^{12}$)	···	($<4 \times 10^{19}$)	$<2 \times 10^{20}$
137.125	1.250	0.039 ± 0.003	$\tau = 0.005 \pm 0.002$	unknown	not foreground	16.7 ± 0.1	not foreground	$3.3 \times 10^{21} \pm 1 \times 10^{21}$
137.125	1.375	0.29 ± 0.003	0.026 ± 0.002 and $\tau = 0.001 \pm 0.001$	65: 10 + 6 or −1.4	$1.24 \times 10^{15} + 1.2 \times 10^{15}$ or -3.5×10^{14}	12.5 ± 0.2	$1.18 \times 10^{22} + 1.1 \times 10^{22}$ or -3.7×10^{21}	$2.5 \times 10^{21} \pm 8 \times 10^{20}$
137.125	1.500	0.067 ± 0.003	···	65: 8.8 + 3.7 or −2.1	$2.43 \times 10^{14} + 1.5 \times 10^{14}$ or -6.3×10^{13}	6.2 ± 0.1	$2.31 \times 10^{21} + 1.5 \times 10^{21}$ or -6.8×10^{20}	$1.2 \times 10^{21} \pm 4 \times 10^{20}$
137.250	1.000	···	···	abs.	($<4 \times 10^{12}$)	···	(4×10^{19})	$<2 \times 10^{20}$
137.250	1.125	···	··· and 0.003 ± 0.002	abs.	($<4 \times 10^{12}$)	···	($<4 \times 10^{19}$)	$<2 \times 10^{20}$
137.250	1.250	···	$\tau = 0.009 \pm 0.002$	unknown	not foreground	2.5 ± 0.1	not foreground	$5.0 \times 10^{20} \pm 2 \times 10^{20}$
137.250	1.375	···	$\tau = 0.029 \pm 0.002$	unknown	not foreground	6.0 ± 0.2	not foreground	$1.2 \times 10^{21} \pm 3 \times 10^{20}$
137.250	1.500	0.041 ± 0.003	···	>12	undetermined	5.3 ± 0.2	undetermined	$1.1 \times 10^{21} \pm 3 \times 10^{20}$
137.375	1.000	···	···	65: 22 + 12 or −10	($<4 \times 10^{12}$)	···	($<4 \times 10^{19}$)	$<2 \times 10^{20}$
137.375	1.125	···	···	abs.	($<4 \times 10^{12}$)	···	($<4 \times 10^{19}$)	$<2 \times 10^{20}$
137.375	1.250	···	···	abs.	($<4 \times 10^{12}$)	···	($<7 \times 10^{19}$)	$<2 \times 10^{20}$
137.375	1.375	···	···	abs.	($<4 \times 10^{12}$)	···	($<4 \times 10^{19}$)	$<2 \times 10^{20}$
137.375	1.500	···	···	abs.	($<4 \times 10^{12}$)	···	($<4 \times 10^{19}$)	$<2 \times 10^{20}$
137.500	0.625	$\tau = 0.0034 \pm 0.002$	$\tau = 0.0031 \pm 0.002$	abs.	(5.4×10^{12})	3.7 ± 0.2	(5.2×10^{19})	$7.4 \times 10^{20} \pm 2.3 \times 10^{20}$
137.500	0.750	···	···	65: 6.7 + 0.3 or −5.5	$< 1 \times 10^{13}$	···	$<1 \times 10^{20}$	$<2 \times 10^{20}$
137.500	0.875	···	···	65: >8.7	no upper limit	···	no upper limit	$<2 \times 10^{20}$
137.500	1.000	···	···	65: 12.5 + 9 or −3.8	$< 6 \times 10^{13}$	···	$< 5 \times 10^{20}$	$<2 \times 10^{20}$
137.500	1.125	···	···	65: >16	no upper limit	···	no upper limit	$<2 \times 10^{20}$
137.500	1.250	···	···	abs.	($<4 \times 10^{12}$)	···	($<4 \times 10^{19}$)	$<2 \times 10^{20}$
137.500	1.375	$\tau = 0.0061 \pm 0.002$	$\tau = 0.0131 \pm 0.002$	abs.	(1.5×10^{13})	2.6 ± 0.1	(1.4×10^{20})	$5.2 \times 10^{20} \pm 1.6 \times 10^{20}$
137.500	1.500	···	···	abs.	($<4 \times 10^{12}$)	···	($<4 \times 10^{19}$)	$<2 \times 10^{20}$
137.625	1.000	···	···	65: >10	no upper limit	···	no upper limit	$<2 \times 10^{20}$
137.625	1.125	···	···	abs.	($<4 \times 10^{12}$)	···	($<4 \times 10^{19}$)	$<2 \times 10^{20}$
137.625	1.250	···	$\tau = 0.003 \pm 0.002$	abs.	(3.5×10^{12})	4.5 ± 0.2	(3.4×10^{19})	$9.0 \times 10^{20} \pm 3 \times 10^{20}$
137.625	1.375	···	$\tau = 0.003 \pm 0.002$	abs.	(3.5×10^{12})	26.9 ± 0.2	(3.4×10^{19})	$5.4 \times 10^{21} \pm 2 \times 10^{21}$
137.625	1.500	0.026 ± 0.003	0.5 ± 0.003	unknown	not foreground	17.0 ± 0.2	not foreground	$3.4 \times 10^{21} \pm 1 \times 10^{21}$
137.750	1.125	···	···	abs.	($<4 \times 10^{12}$)	···	($<4 \times 10^{19}$)	$<2 \times 10^{20}$
137.750	1.250	···	···	abs.	($<4 \times 10^{12}$)	···	($<4 \times 10^{19}$)	$<2 \times 10^{20}$
137.750	1.375	0.027 ± 0.003	0.063 ± 0.003	unknown	not foreground	23.5 ± 0.2	not foreground	$4.7 \times 10^{21} \pm 1.4 \times 10^{21}$
137.750	1.500	$\tau = 0.003 \pm 0.002$	0.007 ± 0.002	abs.	(7.3×10^{12})	28.4 ± 0.2	(6.9×10^{19})	$5.7 \times 10^{21} \pm 1.7 \times 10^{21}$

l	b	1665 MHz (K km s^{-1} or τ)	1667 MHz (K km s^{-1} or τ)	$\frac{T_{ex}}{T_{ex}-T_C}$	N(OH) (cm^{-2})	^{12}CO Profile Integral (K km s^{-1})	N(H$_2$)$_{OH}$ (cm^{-2})	N(H$_2$)$_{CO}$ (cm^{-2})
			and $\tau = 0.002 \pm 0.001$					
137.875	1.250	···	···	abs.	($<4 \times 10^{12}$)	···	($<4 \times 10^{19}$)	$<2 \times 10^{20}$
137.875	1.375	···	···	abs.	($<4 \times 10^{12}$)	···	($<4 \times 10^{19}$)	$<2 \times 10^{20}$
137.875	1.500	···	···	abs.	($<4 \times 10^{12}$)	···	($<4 \times 10^{19}$)	$<2 \times 10^{20}$
137.875	1.625	$\tau = 0.0063 \pm 0.002$	$\tau = 0.0124 \pm 0.002$	abs.	(1.4×10^{13})	9.3 ± 0.1	(1.4×10^{20})	$1.9 \times 10^{20} \pm 6 \times 10^{20}$
137.875	1.750	···	···	65: >7	no upper limit	···	no upper limit	$<2 \times 10^{20}$
138.000	1.250	···	···	abs.	($<4 \times 10^{12}$)	···	($<4 \times 10^{19}$)	$<2 \times 10^{20}$
138.000	1.375	···	···	abs.	($<4 \times 10^{12}$)	···	($<4 \times 10^{19}$)	$<2 \times 10^{20}$
138.000	1.500	···	···	abs.	($<4 \times 10^{12}$)	···	($<4 \times 10^{19}$)	$<2 \times 10^{20}$
138.000	1.625	···	$\tau = 0.0024 \pm 0.002$	abs.	(3.6×10^{12})	1.4 ± 0.1	(3.4×10^{19})	$2.8 \times 10^{20} \pm 9 \times 10^{19}$
138.000	1.750	···	$\tau = 0.006 \pm 0.002$	abs.	(7.1×10^{12})	6.7 ± 0.1	(6.8×10^{19})	$1.3 \times 10^{21} \pm 4.0 \times 10^{20}$
138.125	1.250	···	···	65: >10	no upper limit	···	no upper limit	$<2 \times 10^{20}$
138.125	1.375	···	···	abs.	($<4 \times 10^{12}$)	···	($<4 \times 10^{19}$)	$<2 \times 10^{20}$
138.125	1.500	···	···	abs.	($<4 \times 10^{12}$)	···	($<4 \times 10^{19}$)	$<2 \times 10^{20}$
138.125	1.625	···	···	abs.	($<4 \times 10^{12}$)	···	($<4 \times 10^{19}$)	$<2 \times 10^{20}$
138.125	1.750	···	···	65: >7	no upper limit	6.8 ± 0.1	no upper limit	$1.4 \times 10^{21} \pm 4 \times 10^{20}$
138.250	1.250	···	0.011 ± 0.003	unknown	not foreground	0.5 ± 0.1	not foreground	$1.0 \times 10^{20} \pm 3.6 \times 10^{19}$
138.250	1.375	···	···	65: >21	no upper limit	···	no upper limit	$<2 \times 10^{20}$
138.250	1.500			abs.		7.5 ± 0.2		$1.5 \times 10^{21} \pm 5 \times 10^{20}$
138.250	1.625	···	···	abs.	($<4 \times 10^{12}$)	6.9 ± 0.1	($<4 \times 10^{19}$)	$1.4 \times 10^{21} \pm 4 \times 10^{20}$
138.250	1.750	0.01 ± 0.003	0.014 ± 0.003	unknown	not foreground	10.7 ± 0.1	not foreground	$2.1 \times 10^{21} \pm 6 \times 10^{20}$

Table 3.2: Chart of W5 survey data. Listed for each position in the survey are the galactic longitude, galactic latitude, 1665 MHz profile integral, 1667 MHz profile integral, the coefficient $\frac{T_{ex}}{T_{ex}-T_C}$, calculated column density of OH, ^{12}CO profile integral from Heyer et al. (1998), calculated molecular gas column density from OH, and calculated molecular gas column density from CO. In the OH 1665 and 1667 MHz profile integral columns, if the feature was detected in absorption rather than emission, then instead of a profile integral, the integral of the optical depth is listed preceeded by "$\tau =$". In cases for which only absorption features were detected at both OH main line frequencies, we provide parentheses around the calculated column density values because these values are systematically underestimated. If no detection was made above the noise level of the spectra, we list upper limits for column densities at that position. In the column for the coefficient $\frac{T_{ex}}{T_{ex}-T_C}$, we list first either 65 or 67 to indicate whether the coefficient was calculated using T_{ex}^{65} or T_{ex}^{67}, then after the colon we list the value of the coefficient. In cases where $T_C > T_{ex}^{65}$, we instead list "abs." to indicate that an absorption line would occur at both frequencies if OH were detected. If a W5 feature was determined to be somewhere other than the foreground, we indicate this in the table because then the listed value of T_C may not be accurate for that feature.

Chapter 4

A Comparison between Physical Properties of Gas in W5 with a Quiescent Region in the ISM

4.1 Introduction

In a series of papers (Allen et al. 2015, 2012, 2013; Busch et al. 2019; Engelke & Allen 2018, 2019), we have explored the use of OH 18 cm lines as an alternate tracer for molecular gas in the Galaxy. These papers, along with others such as Dawson et al. (2014) and Nguyen et al. (2018), have presented a case that OH is a viable tracer for molecular gas including CO-dark components. In this chapter, we begin an initial exploration of the effects of volume density on the collisional excitation of

the OH and ^{12}CO(1-0) lines in surveys of two regions: a star-forming region, W5 (Engelke & Allen 2019), and a quiescent region in the Perseus Arm towards the outer Galaxy Busch et al. (2019). We apply a diffuse cloud model Neufeld & Wolfire (2016) to predict the volume densities and brightness temperatures of OH and CO, in order to gain insight into the physical conditions in the two surveyed regions. We find that W5 contains the greatest average volume density, while the CO-bright portions of the quiescent region contain intermediate average volume density values, and the CO-dark portions of the quiescent region contain the lowest volume densities. These findings suggest a picture in which CO-dark gas in the interstellar medium may be explained as resulting from regions of lower gas volume density and hence a lower rate of collisional excitation. The primary distinction between molecular gas in W5 as compared to the quiescent region appears to be the volume densities, rather than the total quantity and mass of molecular gas. We suggest further that the reason for such differences in volume density between the two regions may result from shock waves caused by activity in the star-forming region. Such shock waves could create regions of higher density in the ambient molecular gas, which in turn would provide more favorable conditions for the production of ^{12}CO(1-0) emission. Molecular gas in the quiescent region may be more difficult to detect from ^{12}CO(1-0) emission simply as a result of lower average volume density and fewer density fluctuations in a less active environment.

The OH abundance is similar to that of CO in the molecular ISM, and OH pro-

duces optically thin lines that are ammenable to direct calculation of column densities using radiative transfer equations and a minimum of assumptions. Notably, the OH 18 cm lines have a lower critical volume density required for collisionally excited emission than does ^{12}CO(1-0). The critical density for ^{12}CO(1-0) is near 10^3 cm^{-3} divided by the optical depth τ, whereas the critical density for the OH 18 cm transition is near 1 cm^{-3}. Hence it seems plausible that lower volume density regions of the molecular ISM may be well-traced by OH, even though they may be undetectable or only weakly detectable through ^{12}CO(1-0) observations.

A second explanation is provided by Wolfire et al. (2010), which is the hypothesis that the CO-dark gas results from molecular gas near photodissociation regions in which the CO is photodissociated and the carbon becomes C or C^+ while the H_2 is self-shielded against the UV flux and thus remains intact. While OH would also be photodissociated from the UV flux, it is a precursor to CO formation so CO abundance would still be lower than OH abundance in these regions for strong UV fields. OH abundance would depend on the inverse of the UV field while CO abundance would depend on the square of the inverse of the UV field. Both of these mechanisms to produce observationally CO-dark molecular gas may exist in the ISM, but perhaps they apply for different components and size scales. In the case of this work, we focus on the influence of volume density on CO-dark gas, and large size scales of several parsecs per telescope beam.

4.2 Data

4.2.1 W5 Survey

Survey data from two regions of the sky are used in this study. The first survey is a grid survey in the W5 star-forming region. The observations for the OH 18-cm survey are described in detail in Engelke & Allen (2019). This survey consists of eighty 2-hr observations made using the Robert C. Byrd Green Bank Telescope in the L-band using the VEGAS spectrometer in frequency-switching mode, between February 2016 and April 2017. At each position, we observed all four OH 18-cm transitions at 1612, 1665, 1667, and 1720 MHz, plus the 1420 MHz HI line in dual polarization. The FWHM of the GBT point spread function at 1667 MHz is 7.6'. The grid separation of the survey was 0.125°. The survey follows a somewhat irregular shape intended to roughly cover the spatial distribution of W5, including regions with a range of continuum temperature values. Engelke & Allen (2019) provides a map of the survey and a description of the data reduction process.

We compare the OH observations with ^{12}CO(1-0) data from the Five College Radio Astronomy Observatory (FCRAO) Outer Galaxy survey (Heyer et al. 1998), which we smooth to the resolution of the GBT OH observations, at 7.6'.

4.2.2 One Square Degree Survey

The second survey is a GBT grid survey in a quiescent region covering one square degree towards the Perseus Arm in the Outer Galaxy. This region was part of the subject of a pilot survey in Allen et al. (2015) and then a grid survey in Busch et al. (2019) with the same grid separation as the W5 survey of 0.125°. This one-square-degree region is centered on $l = 105.0°$, $b = 2.5°$, and the survey results are presented in Busch et al. (2019). The survey consists of 81 observations performed with the GBT between September 2015 and January 2016, with a repeat of one observation made in February 2019. The details of the observing strategy and data reduction are similar to those for the W5 survey, and are described in detail in Busch et al. (2019).

As with the W5 survey, we compare the OH observations with ^{12}CO(1-0) data from the FCRAO survey (Heyer et al. 1998), which we smooth to the resolution of the GBT OH observations, at 7.6'.

4.2.3 Column Densities of OH

The OH and CO surveys provide data on profile integrals of OH and CO signals, respectively. We wish to calculate the column densities of OH as traced by the OH signals. For CO, use of profile integrals is sufficient for the study because the optically thick CO profile integrals are assumed to be proportional to CO column densities when using the X-factor method (Bolatto et al. 2013) based on virial theorem arguments.

The equations for the OH column density calculations are described in detail in Engelke & Allen (2019). Since for the purposes of this paper, we are only concerned with OH emission lines (see Engelke & Allen (2019) for an explanation of the difficulties of calculating column densities from OH absorption lines in the W5 survey), we use the following equation (see e.g. Liszt & Lucas 1996):

$$N(OH) = C\frac{T_{ex}}{T_{ex} - T_C}\int T_b(\nu)d\nu, \tag{4.1}$$

where the coefficient $C_{67} = 2.3\times10^{14}$ for 1667 MHz, T_{ex} is the excitation temperature, T_C is the continuum temperature, and $\int T_b\nu d\nu$ is the observed line profile integral, where all temperatures are measured in Kelvin, and ν is in km/s. The methods of determining continuum temperature and excitation temperature as well as their values for the W5 survey are provided in Engelke & Allen (2018) and Engelke & Allen (2019). For the One Square Degree quiescent region survey, we use the same methods described in Engelke & Allen (2018) and Engelke & Allen (2019), but we determined the values of the continuum temperatures for the One Square Degree survey separately.

4.3 The Diffuse Cloud Model

In order to make theoretical predictions of the volume densities for the regions observed in the two OH surveys, we use a diffuse cloud model developed by Hollenbach

et al. (2012) and modified by Neufeld & Wolfire (2016). If in addition to OH column density data, ^{12}CO(1-0) profile integral data are supplied, the model is able to predict volume densities of hydrogen nuclei in the gas. The model is based on a two-sided slab with an isotropic radiation, and calculates gas kinetic temperature and chemical abundances as a function of depth into the cloud (Neufeld & Wolfire 2016). Gas phase abundances, collision rates, heating rates, and chemical reaction rates, are gleaned from various sources in the literature, as described in Neufeld & Wolfire (2016).

Following the example of Busch et al. (2019), we assume a cosmic ray ionization rate of 2×10^{-16} s^{-1} (Neufeld & Wolfire 2017), an ultra-violet radiation field from Draine (1978), and a 1667 MHz OH excitation temperature of 5 K (Engelke & Allen 2018).

4.4 Volume Density Results from the Model

The results of the diffuse cloud model are plotted in Figures 4.1, 4.2, 4.3; and 4.4. Three plots are made for different combinations of T_C and T_{ex} (see Section 4.8 for an explanation of the uncertainties involved in estimating T_C and T_{ex} including aspects that were not yet discussed Engelke & Allen (2018) and only touched upon in Engelke & Allen (2019)). The observations from the One Square Degree quiescent region using one choice of T_C and T_{ex} values are plotted on top of the diffuse cloud

model curves in Figures 4.1, 4.2, and 4.3, taken from our paper on the One Square Degree survey, Busch et al. (2019). A representative range of the plausible T_C and T_{ex} values is shown in Table 4.1, and shown in Busch et al. (2019). Figure 4.4 shows the W5 survey data plotted on top of the model curves. Next, we calculate the average value of the volume density predicted by these models for three groups of data points based on where the data fall on the model curves: the observations containing OH emission in the W5 star-forming region, the CO-bright portion of observations in the quiescent One Square Degree region, and the CO-dark portion of the observations in the quiescent One Square Degree region. For the W5 observations, the average value of volume density is 890 ± 130 cm^{-3}. The median value of volume density for these same observations in W5 is 750 ± 250 cm^{-3}.

The average volume density for the One Square Degree quiescent region can be found for the portion of the survey containing CO-bright OH detections, as well as an upper limit on the average volume density for the portion of the survey containing CO-dark OH detections. The average volume densities for three different combinations of input parameters representative of the range of plausible values are listed in Table 4.1, taken from Busch et al. (2019). Note that for all three cases of input parameters, the volume density of the CO-bright gas in the quiescent region is less than that in the W5 star-forming region, but greater than that in the CO-dark gas in the quiescent region.

Table 4.1: Volume Density of H Nuclei for Molecular Gas in the One Square Degree Survey.

T_C (K)	T_{ex}^{67} (K)	F	CO-Bright Mean H Volume Density (cm^{-3})	CO-Dark Mean H Volume Density (cm^{-3})
4.0	5.0	5.0	400 ± 70	$<210 \pm 20$
5.0	6.0	6.0	280 ± 40	$<200 \pm 20$
5.0	5.5	11	160 ± 15	$<120 \pm 10$

4.5 Comparison of Volume Densities in W5 and the One Square Degree

The volume density predictions using the diffuse cloud model suggest that the majority of the gas in molecular clouds in front of W5 has greater volume density than that of the molecular gas clouds in the One Square Degree quiescent region. Moreover, the CO-bright portion of the One Square Degree region has a lower volume density than the molecular clouds near W5, but a greater volume density than the CO-dark portion of the One Square Degree region. These results support the idea that CO-dark gas at large scales results from lower volume densities which do not create optimal conditions for observing strong CO excitation below the CO(1-0) critical density, whereas OH signals continue to be adequately detected well above the OH 18 cm critical density. No CO-dark gas was detected in front of W5 (Engelke & Allen 2019), and one possible explanation for this difference between W5 and the quiescent regions surveyed in Allen et al. (2015) and Busch et al. (2019) could be differences in the molecular gas volume density. While chemical depletion of CO at the edges

of molecular gas clouds may play a role as well in CO-dark gas, the diffuse cloud model, which incorporates this effect, suggests that the volume density effect is a contribution to the CO-dark gas phenomenon as well. This contribution is perhaps more important on larger scales, while chemical depletion of CO is more important on smaller scales such as the edge of a photo-dissociation region.

We note that the W5 star-forming region appears to be fairly well-traced by CO, with no CO-dark portions in the Engelke & Allen (2019) survey. On the other hand, the quiescent One Square Degree survey includes numerous positions containing CO-dark molecular gas, and these are the portions of the gas that appear to have the lowest volume density. The implication is that CO-dark molecular gas may be primarily located in the vast regions of the ISM outside of star-forming regions, whereas star-forming regions are generally likely to be already well-traced by ^{12}CO(1-0) data.

4.6 Enclosed Mass Comparisons and Density Fluctuations

We now analyze the total mass of molecular gas contained in the two regions, and compare these results to the results for volume densities. The total mass of molecular gas in W5 is roughly 4 ($\pm$2) $\times$ $10^4 M_\odot$ (Engelke & Allen 2019) if we incorporate the positions that contained OH absorption rather than emission in the W5 survey, where we take 2 to 3 times the 1.7 ($\pm$0.6) $\times$ $10^4 M_\odot$ estimated for the portion of the W5

survey containing OH emission (Engelke & Allen 2019). The survey region contains 80 observations in a grid structure covering W5, which is 2.0 kpc away, whereas the One Square Degree survey region contains 81 observations of the same full width at half maximum in a grid structure, making it similar in scope. However, the features in the Perseus Arm in the One Square Degree survey are 3.2 kpc away (Busch et al. 2019), which is 1.6 times farther than W5. As a result, the One Square Degree survey covers an area 2.6 times greater than does the W5 survey. The sum of the column densities of molecular gas estimated from OH column densities in the One Square Degree survey is 4 (+ 3.5 or -1) $\times 10^4 M_\odot$, and dividing this by 2.6 for a comparable region size, we have 2 (+ 2 or -1) $\times 10^4 M_\odot$.

First, we note that the mass contained in the One Square Degree survey for a similar sized region of sky to the W5 survey is slightly less than the mass contained in the W5 survey. However, this is not surprising, considering that the W5 survey was partially intended to target known gas clouds, whereas the One Square Degree survey was entirely blind. What seems more remarkable is how similar the values are for the mass enclosed by two regions of comparable size. Considering the uncertainty involved in the total mass in W5 when extending the estimate to the portions containing absorption lines, as well as the uncertainty for the One Square Degree region resulting from the unknown values of T_{ex} and T_C, the two regions contain surprisingly similar masses of molecular gas.

This result raises the question as to what is the major distinction between the star-

forming region and the quiescent region that we have studied. The supposition that the star-forming region contains significantly more molecular gas does not appear to explain the differences since the quantity of molecular gas is not so different between the two regions. However, we know that the volume densities are notably greater in W5 than in the quiescent region by a factor of about 4, and that the CO-dark portions of the quiescent region contain the lowest volume densities. These results point toward the idea that density fluctuations may be of importance when determining which regions are detected in CO and which are CO-dark. The densities of the observed regions are certainly not constant. A simple look at the CO contour maps from Heyer et al. (1998) and Dame et al. (2001) indicates complex structure in the molecular gas clouds. Our OH results continue to support the idea of complex structure. Moreover, regions smaller than the telescope field of view most likely contain further complex structure at a smaller scale, that is simply more difficult to map out. The discrepancy in column densities measured from emission lines and absorption lines at the same coordinate in Engelke & Allen (2019) is direct evidence of this fact; we estimated an OH filling factor of a few to ten percent from modeling the absorption. It is only natural, then, to suppose that regions of elevated volume densities exist alongside less dense regions within our observed regions. Observations will pick out the regions of higher density because that is where the majority of the gas lies; regions of lower density exist between the majority of the gas and are not well represented by the observations. The fact that the volume density is not constant throughout the survey

regions becomes evident by simply taking the total mass estimate of molecular gas in each region and dividing by an estimate of the volume of the surveyed region. Although we do not know the line of sight depth of the molecular gas clouds in the surveys, we note that only a depth of less than 1 pc allows the volume densities to come out comparable to the modeled values. However, each telescope beam covers several pc diameter in the surveys (4.4 pc for W5 and 6 pc for the One Square Degree), and molecular cloud structure appears to take up multiple telescope beams in the tangential portions of the surveyed regions. Especially in the One Square Degree region, where there are no hot stars to dissociate molecular gas beyond a thin shell layer, there is no reason to suppose that the gas is all confined to a 1 pc depth. A far better assumption is that the depth of the clouds is comparable to the cloud size scale of tens of parsecs in the tangential direction, but that density fluctuations exist within the region.

We now suggest a hypothesis to explain the major distinction between W5 and the One Square Degree region, as well as between CO-bright and CO-dark portions of the One Square Degree region. Both the star-forming region and the quiescent region contain roughly similar amounts of molecular gas, but the star-forming region, which contains hot stars whose UV produces ionized material and stellar winds leading to shock waves in the gaseous medium. Supernova remnants could also produce shock waves; OH 1720 MHz maser emission could point to possible C-shocks (Lockett et al. 1999) although most types of shock waves in W5 would not be revealed in this way.

These shock waves cause an increased amount of variation in volume density of the gas, including pockets of relatively high density as compared to the quiescent region. These higher density regions contain the majority of the gas in the cloud. The quiescent region, which does not contain many hot stars, lacks the shock waves that are present in the star-forming region. As such, its level of density variation is lower, although there are still regions of somewhat higher and lower density, as appears to be the case generally for gas clouds. Regions of sufficient density to lead to detectable CO signals appear in the CO-surveys as CO-bright molecular gas, while the remainder of the molecular gas, at lower densities, does not produce sufficiently strong CO signals to appear in CO surveys, as it is likely below the critical density for CO(1-0) emission and hence produces only weak emission. Since the critical density for OH 18 cm emission is lower, these regions are still detected in sensitive OH surveys. They comprise the CO-dark portions of the Allen et al. (2015) survey and the One Square Degree region (Busch et al. 2019).

4.7 Conclusions

We have modeled the physical properties of molecular gas as traced by OH 18 cm data as well as CO(1-0) data Heyer et al. (1998) in the W5 star-forming region Engelke & Allen (2019) and in a quiescent One Square Degree region (Busch et al. 2019) using a diffuse cloud model. The results of this modeling predict that average

volume densities are greatest in the W5 star-forming region, intermediate in the CO-bright portions of the One Square Degree quiescent region, and least in the CO-dark portions of the One Square Degree region. These results bolster the claim that CO-dark gas appears to be largely a result of low gas volume densities on large scales. The comparison between gas densities and CO-dark gas content in W5 and the One Square Degree region also suggests that CO-dark gas most likely exists primarily outside of star-forming regions, in the diffuse interstellar medium. We find that the total mass is similar for clouds near W5 and in the One Square Degree region even though the densities are greater for W5. We suggest that the major distinction between the two regions could be that the star-forming region contains larger variation in density leading to higher density pockets. Lower density gas in the quiescent region would produce weak-emissivity CO signals while being fully detected in OH at high sensitivity, thus contributing to the observational phenomenon of CO-dark molecular gas. The higher density regions could result from shock waves produced by stars.

4.8 Appendix: The Continuum and Excitation Temperatures

Before we can calculate column densities of OH and proceed to the main analysis of this paper, we must obtain values for the continuum and excitation temperatures to go into Equation 4.1. Determining the continuum temperatures and excitation

temperatures for the regions behind our observations is subject to several complications, some of which we did not fully appreciate at the start of our work on OH as a molecular gas tracer. For example, in the the Engelke & Allen (2018) paper where we determine the excitation temperatures for the OH main lines, our values for T_C may be subject to systematic error. While this systematic error does not affect the results of OH column densities reported in Engelke & Allen (2019) for reasons explained in that paper, the actual values of T_{ex} reported in Engelke & Allen (2018) will be subject to the same systematic error as the values of T_C. This possible error source, which we shall discuss in detail in this section, affects the results of the study of the One Square Degree region even if it does not affect the results for the W5 star-forming region in the same way. As such, we must address these complications, and find a range of suitable parameters for input into the model.

The first complication arises from the fact that the continuum temperature is composed of three parts: the contribution from the cosmic microwave background T_{CMB}, the contribution from the Galaxy containing synchrotron emission, T_{gal}, and the contribution from sources such as the W5 star-forming region, T_{source}. The spectral index of each of these components need not be the same; in the case of W5, the source component consists of free-free emission, with a spectral index when plotted logarithmically of approximately -2, T_{gal} has a spectral index of approximately -2.7 (Reich & Reich 1988), and T_{CMB} is constant over frequency as a blackbody spectrum. While we attempted in Engelke & Allen (2018) to separate the continuum into a free-

free component and a background, we did not fully understand the complexity of the situation as well as the correct interpretation of the data sets in the literature. As such, we may have introduced a systematic error or underestimated the uncertainty involved in finding the exact value of T_C behind an OH feature. This situation becomes more of a problem for the One Square Degree region, however, because in that region we do not even have a dominating source component such as W5 to provide a well-understood spectral index. For the Engelke & Allen (2018) and Engelke & Allen (2019) papers, we used the Canadian Galactic Plane Survey (CGPS) (Taylor et al. 2003) smoothed to the appropriate resolution at both 408 MHz and 1420 MHz, as well as the Fürst et al. (1990) Effelsberg survey at 2695 MHz to interpolate linearly on a logarithmic plot and estimate T_C at 1667 MHz. While this strategy seems appropriate, we did not correctly understand the presentation of the Fürst et al. (1990) data, since they separated the continuum into a "source" component and a "diffuse" component, and we only used the source component in that calculation. It is difficult to decide exactly how to best proceed when using the CGPS data and the Effelsberg data together, since the CGPS data set is not separated into a source component and a diffuse component, whereas the Effelsberg data set is. Moreover, whereas the source component is of primary importance when studying OH in front of W5, the diffuse component is the most relevant part of the continuum for study of the One Square Degree quiescent region. The question arises for the One Square Degree region as to whether the source component is relevant at all. The source component could be

located either in front of or behind the OH features in the Perseus Arm, and it is unclear whether this sparse component of the continuum temperature contributes to T_C behind the OH features, or by how much. Clearly, a more careful study of the source and diffuse contributions to the continuum and the spectral indices involved is necessary before we perform our analysis in this paper.

For the purposes of this paper as well as Busch et al. (2019), we interpolate to 1667 MHz without making any assumptions about the value or nature of the spectral index, since the spectral index might vary over frequency or could have been measured inaccurately. Instead, we fit a quadratic equation to the natural logarithm of the three T_C values at 408, 1420, and 2695 MHz respectively, as a function of the natural logarithm of the frequency:

$$T_C(\nu) = e^{a(ln\nu)^2 + bln\nu + c}, \tag{4.2}$$

evaluating the equation at $\nu = 1667$ MHz. These values need not be exactly consistent with the Engelke & Allen (2018) results because of the new improved calculation method, although they do not differ by more than ~ 0.8 K for W5.

Before discussing the details and uncertainties involved with the continuum temperature values for the One Square Degree, we will explain why the aforementioned problem does not alter the results for OH column densities in W5 reported in Engelke & Allen (2019) in a non-negligible way. This argument is summarized in that paper

as well, and rests on the fact that Equation 4.1 depends specifically on the expression $T_{ex}/(T_{ex} - T_C)$. Since we determined T_{ex} for W5 based on our own estimated values of T_C, any systematic error in T_C is going to be similarly reflected in our estimated value of T_{ex}.

Thus we can roughly assume that if the values of T_C are systematically inaccurate by a factor of A, the T_{ex} values determined in Engelke & Allen (2018) will be systematically inaccurate by approximately the same factor A. Putting these new values into the factor F in Equation 4.1, where we define F as $T_{ex}/(T_{ex} - T_C)$, we have

$$F_{adjusted} = \frac{AT_{ex}}{AT_{ex} - AT_C} = \frac{T_{ex}}{T_{ex} - T_C} = F_{original}, \tag{4.3}$$

so that the resulting values of OH column density are negligibly influenced by any systematic error in the determination of T_C and T_{ex}. If the spectral index differs between one position and another in the W5 survey, then it is possible that T_C and T_{ex} will be off by slightly different factors; however, the spectral index between 408 MHz and 1420 MHz does not appear to vary by more than up to 10 percent. If we suppose that T_{ex} is off by a factor A and T_C is off by a factor B as a result of slightly different spectral indices where the observations were made, then we have

$$F_{adjusted} = \frac{AT_{ex}}{AT_{ex} - BT_C} = \frac{1}{1 - \frac{BT_C}{AT_{ex}}} \approx 1 + \frac{B}{A}\frac{T_C}{T_{ex}}, \tag{4.4}$$

whereas the first order Taylor approximation for the original unadjusted F is

$$F_{original} = \frac{T_{ex}}{T_{ex} - T_C} \approx 1 + \frac{T_C}{T_{ex}}. \tag{4.5}$$

Thus, with some algebra, we have

$$F_{adjusted} \approx \frac{B}{A} F_{original} + 1 - \frac{B}{A}. \tag{4.6}$$

If the spectral index ratio can be as great as 1:1.1, then B/A could be as large as 1.1; for a plausible value of $F = 5$, the resulting adjustment would be $F_{adjusted} \approx 1.08 F_{original}$. The resulting effect on the calculated column densities will be negligible compared to all other sources of uncertainty in that calculation.

However, we still wish to understand any systematic error sources and estimate the uncertainty in the values we are reporting for T_{ex}, since the T_{ex} values still have importance in themselves for modeling line excitation and physical conditions in the gas in W5 even if the calculations of column densities are not adversely affected. Moreover, the uncertainties involved in estimating T_C and T_{ex} are even more important for the One Square Degree region.

For the One Square Degree quiescent region continuum, we begin by noting that there is much less variation in the continuum temperature over the region than their is for the W5 field. Moreover, this continuum primarily originates from the diffuse component, rather than the source component, as categorized by e.g. Fürst et al.

(1990); Reich et al. (1997). There are a few features in the source component, although whether these features exist behind or in front of the OH features is important in determining whether or not to include them in the T_C estimate.

There may be no definitive way to be certain about how the source component should be interpreted. For the most part, with one noteworthy exception, it is not a major part of the continuum. Since our results for volume densities in this paper will be based on averaging over many observational results, it seems most sensible to consider only the diffuse component. However, we also note that there is uncertainty introduced by this assumption, so that we propose a range of possible T_C values instead of one single estimate.

From here, we take the logarithm of the smoothed diffuse component in the Effelsberg 1420 MHz Reich et al. (1997) and 2695 MHz data Fürst et al. (1990) and the smoothed 408 MHz value from the Stockert survey Haslam et al. (1982) (there is no source and diffuse component separation available in this survey but the source component is likely negligible). Then we perform a quadratic fit between the three values, and find the resulting predicted value at 1667 MHz based on the fit.

Regardless of how we choose to make use of the source and diffuse components, there remains the problem of how much of the continuum lies behind the OH features along the line of sight. Even the diffuse component could contain emission partly from behind and partly from in front of the OH. Then the true value of the continuum temperature behind the OH would perhaps be lower than that which we observe.

While we can estimate what fraction of the continuum lies behind the OH features in the Perseus Arm based on arguments from Galactic structure, there appears to be no way to ascertain an exact accurate value for T_C behind the OH. Instead, we propose a range of plausible values.

Estimating T_{ex} poses another problem. Even if not for the systematic error introduced in the T_{ex} estimates from W5, there is no reason to assume that T_{ex} should have the same value in W5 and in the One Square Degree. Again, a range of plausible values might be more reasonable than a single estimate. However, we do have the means to estimate how T_{ex} in the One Square Degree region relates to T_C in that region, because of a feature in the source component of the continuum at $l = 104.7°, b = 2.8°$.. This feature is listed as a probable HII region in Gregory et al. (1996). Since the OH observation in front of that coordinate in the One Square Degree survey contains no OH detection, while the corresponding CO observations does contain a detection in the Perseus Arm, we suppose that the explanation is an elevated T_C value behind that feature such that $T_C \approx T_{ex}$. In the One Square Degree region, we have no evidence that $T_{ex}^{65} - T_{ex}^{67}$ is as large as in W5; this difference probably results from differences in volume density, as will be discussed in Section 5.5. If we assume that the HII region is located behind the Perseus Arm OH feature, then we find that $T_{ex} - T_C \approx 1$ K in the One Square Degree region. We employ this difference for two out of the three plausible cases of F that we study in this paper; the third case is for the possibility that $T_{ex} - T_C$ is less than we believe, which although unlikely, would alter the results

and is therefore worth including in the range of possible parameter values.

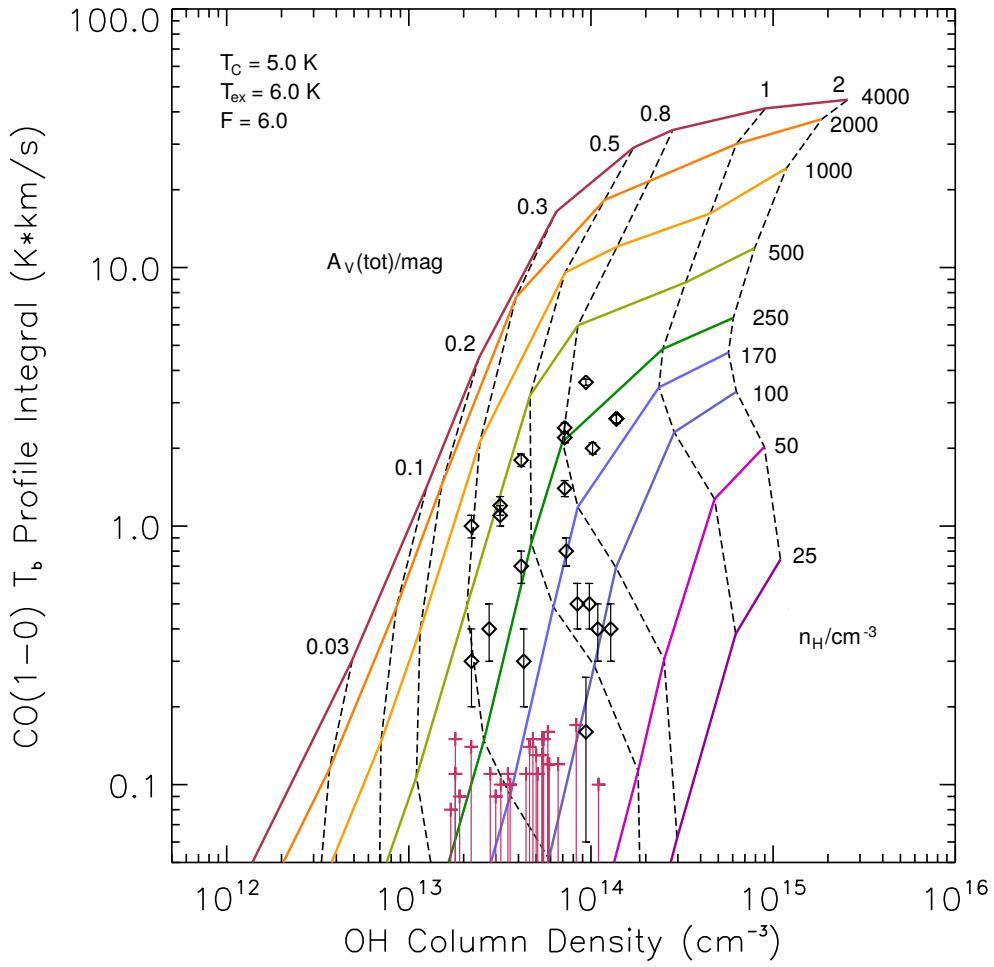

Figure 4.1: The predicted OH column densities and brightness temperatures of the CO(1-0) line as a function of the thickness of the cloud and the volume density of H nuclei in the quiescent One Square Degree region, for one set of possible values of T_C and T_{ex}. This figure is taken from Figure 4 in Busch et al. (2019). The colored contours indicate volume density of H nuclei, and the black dashed curves indicate thickness of the cloud in terms of visual extinction. OH column densities calculated for each of our OH observations (Busch et al. 2019) and the FCRAO Outer Galaxy CO data (Heyer et al. 1998) are plotted on the model curves. The data indicate that this region of the Perseus Arm exhibits low volume densities and low column densities, and that the volume densities are typically lower for CO-dark gas than for CO-bright gas. The model was run with three sets of input values of T_C and T_{ex}, and the factor $F = T_{ex}/(T_{ex} - T_C)$ representative of the plausible value range for this region. The plot shown here shows the results from one of these three runs, with T_C = 5.0 K and T_{ex}^{67} = 6.0 K, with results in the middle of the range from the three runs. Error bars from the noise level on the OH observations are not shown but would be comparable in size to the size of the data markings.

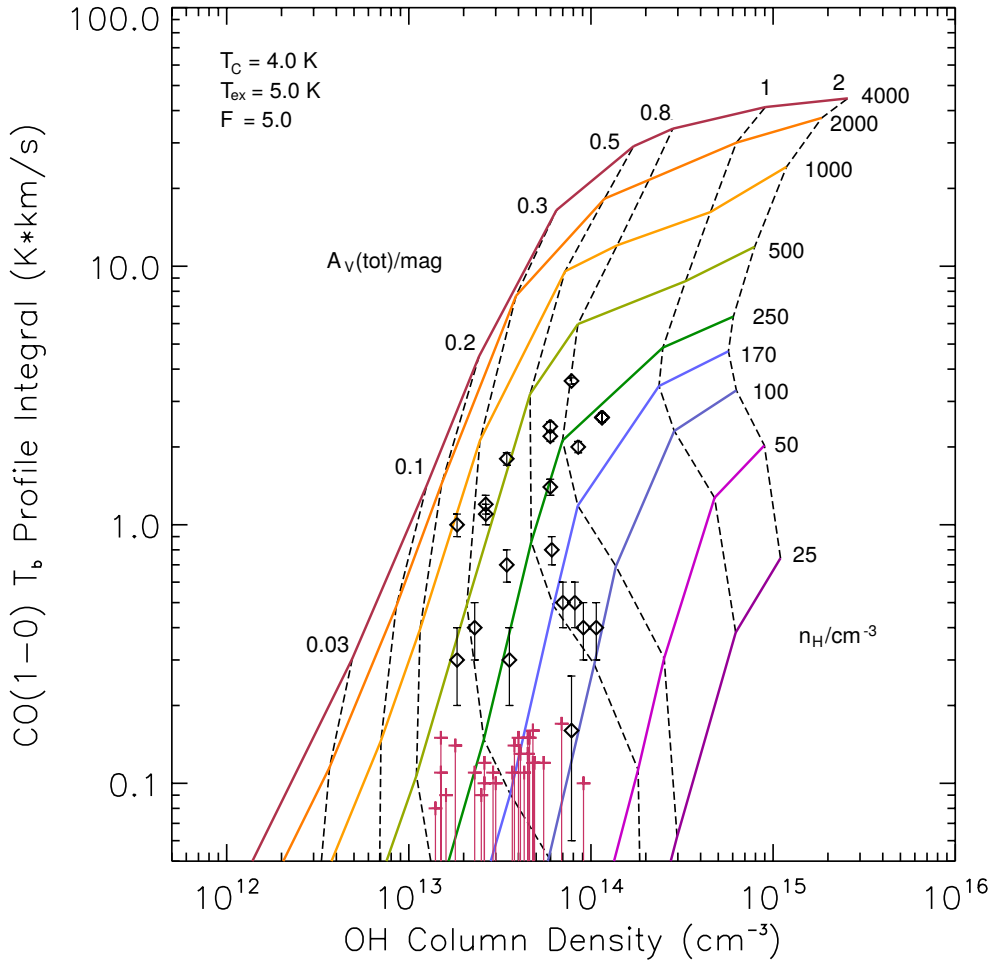

Figure 4.2: Results from the same model as plotted in Figure 4.1 are shown except with a different set of input parameters. This plot is useful mainly to indicate the level of uncertainty on the OH column density results, as it represents the low OH column density limit of the plausible range. The plot shown here displays the model results if $T_C = 4.0$ K and $T_{ex}^{67} = 5.0$ K. Note that the data points are all shifted to the left as compared to Figure 4.1.

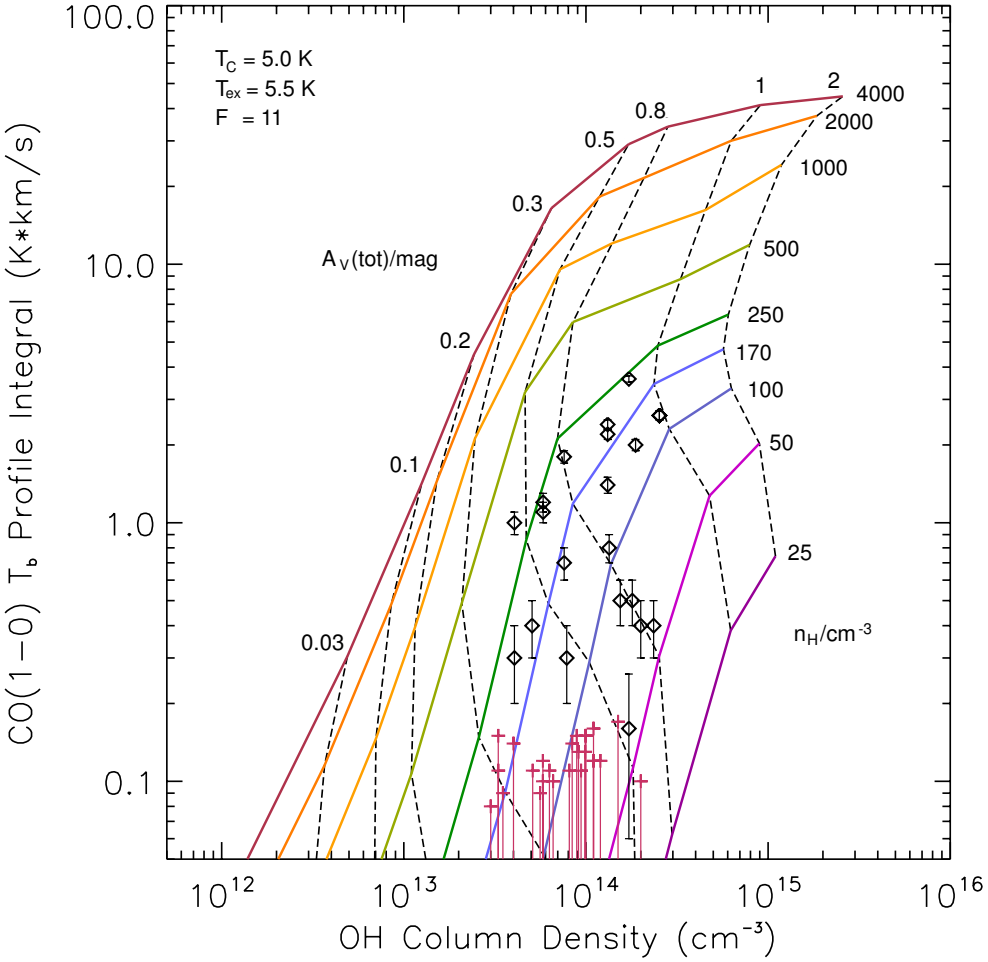

Figure 4.3: Results from the same model as plotted in Figure 4.1 are shown except with a different set of input parameters. This plot is useful mainly to indicate the level of uncertainty on the OH column density results, as it represents the high OH column density limit of the plausible range. The plot shown here shows the model results if $T_C = 5.0$ K and $T_{ex}^{67} = 5.5$ K. Note that the data points are all shifted to the right as compared to Figure 4.1.

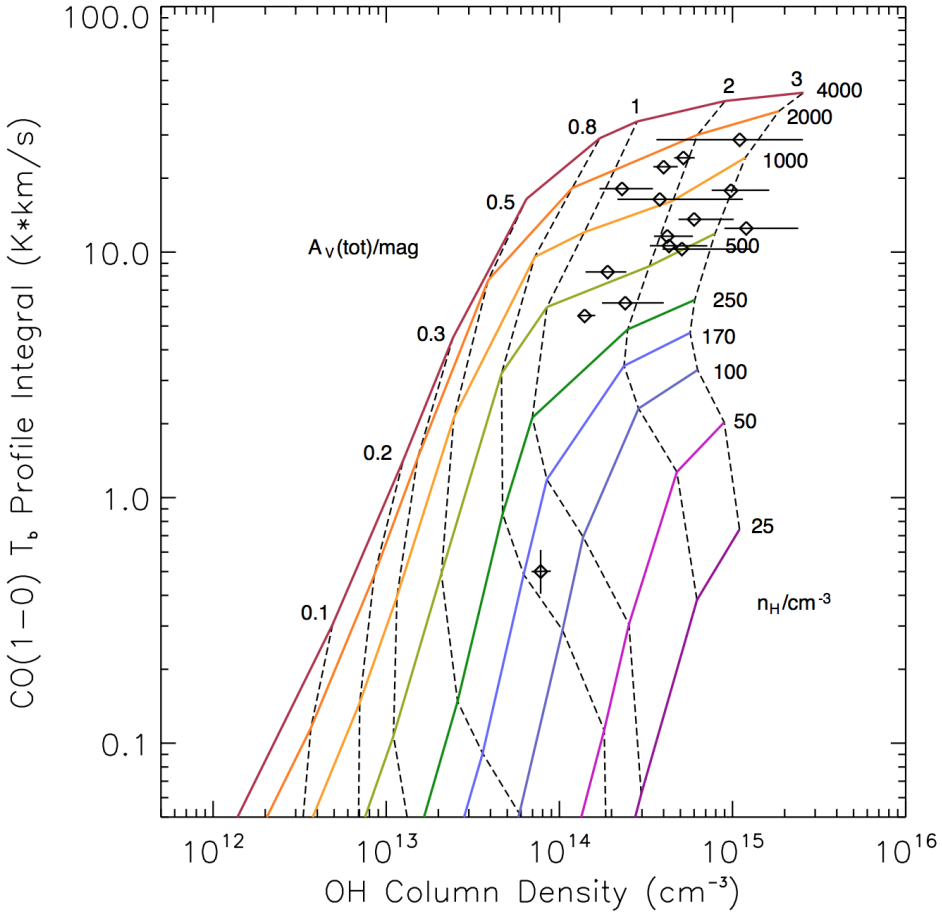

Figure 4.4: Predicted OH column densities and brightness temperatures of the CO(1-0) line as a function of the thickness of the cloud and the volume density of H nuclei in the W5 star forming region. Colored contours indicate volume density of H nuclei, and black dashed curves indicate thickness of the cloud in terms of visual extinction. OH column densities calculated for each of our OH observations (Engelke & Allen 2019) and the FCRAO Outer Galaxy CO data (Heyer et al. 1998) are plotted on the model curves. The horizontal error bars represent the uncertainty in the OH column density as described in Chapter 4, Engelke & Allen (2019); the vertical error bars are only shown for one data point and represent the uncertainty in CO profile integral; for the other data points, the vertical error bars would be smaller than the point size and are not shown. The data indicate that this star-forming region exhibits higher volume densities and column densities compared to the quiescent One Square Degree region.

Chapter 5

Estimating Volume Density and Kinetic Temperature from 18 cm OH Main Line Excitation

5.1 Introduction

In this chapter, we propose a new method to probe the physical conditions of molecular gas using OH 18 cm observations as well as a line excitation model. This method takes measured main line excitation temperatures as inputs and estimates volume density and kinetic temperature for gas in a particular region. The resulting volume density estimates are particularly sensitive to the difference in main line excitation temperatures, which is convenient considering that the difference in main line

excitation temperatures can be measured with more accuracy than the values of the excitation temperatures themselves. The volume density predicted for W5 using this method is consistent with the volume density predicted using the diffuse cloud model in Chapter 4. This method has promise to be applied to the study of physical conditions of molecular gas near other star-forming regions without reliance on ^{12}CO(1-0) data.

The logic of the method begins as follows. We have measured the excitation temperatures of the 18 cm main lines and measured the difference between those values, (Engelke & Allen 2018, 2019) with particular accuracy. In theory, the excitation temperature depends on the kinetic temperature, volume density, and the ambient radiation field incident on the gas, as some basic properties of the region. We can estimate the values of some of these parameters. In Chapter 4, we modeled the volume densities of gas in W5 and a quiescent region using inputs from OH and CO observations. The ambient radiation field can be estimated for a region based on knowledge of the sources and continuum in that region, and the Doppler width of the region is known from observed linewidths. Thus it should be possible to estimate the excitation temperatures by modeling the line excitation. Input parameters in the line excitation model would include the the volume density predicted by the diffuse cloud model (Busch et al. 2019; Neufeld & Wolfire 2016) and reasonable choices for kinetic temperature and ambient radiation. Of course, the resulting predictions for the excitation temperatures will be a range of possible values, since the input parameters

are merely uncertain estimates.

A reversal of the logic, however, turns out to be particularly fruitful. If the excitation temperatures depend on volume density, kinetic temperature, and ambient radiation, then volume density and kinetic temperature also depend on the excitation temperatures and ambient radiation. We can assume both the excitation temperatures and ambient radiation as given, and look for the volume density and kinetic temperature input parameters for which a line excitation model produces the desired excitation temperature values as outputs. Although the exact values of the excitation temperatures are uncertain to $\pm \sim 1K$, the difference in the excitation temperatures $\Delta T_{ex} = T_{ex}^{65} - T_{ex}^{67}$ is revealed more precisely by the continuum background method (Engelke & Allen 2018, 2019) to $\pm \sim 0.3K$. Analysis using the line excitation model code molpopCEP (Asensio Ramos & Elitzur 2018) demonstrates that the main line excitation temperature difference is particularly sensitive to molecular gas volume density. Hence we are able to estimate molecular gas volume density purely from OH observations for any region where it is possible to measure an 18 cm main line excitation temperature difference using the continuum background method. This technique could have future applications for determining volume densities of molecular gas traced by OH. It would be suitable for regions containing continua elevated several degrees above the sum of Galactic background and CMB continuum emission, as well as some variation in the continuum brightness over the survey region over several K.

5.2 The Line Excitation Model

We use the line excitation code molpopCEP (Asensio Ramos & Elitzur 2018) to predict excitation temperatures when provided input parameters about the conditions of the interstellar gas. The molpopCEP code performs a radiative transfer calculation that provides an exact solution for multi-level line emission from a slab. Physical conditions are set by input parameters which include gas kinetic temperature, volume density, molecular abundance, and the Doppler width of the slab. Optional input parameters include diluted blackbody radiation, dust radiation, and additional radiation from a file (Asensio Ramos & Elitzur 2018).

We assume a constant value for OH molecular abundance from Weselak et al. (2010) of 1×10^{-7}. We assume that the velocity widths of our detected OH lines are equivalent to the Doppler width of the slab, so that parameter is also fixed. We add a uniform blackbody temperature of 1.5 K above the cosmic microwave background, incident on the slab from the side in order to simulate the background continuum temperature in front of W5, and we do not add external radiation from a file. The internal dust temperature is set to 15 K, which is appropriate for the Perseus Arm (see e.g. Marsh et al. 2017), and the dust optical depth is set to 0.2. The Doppler width is set to 0.1 km/s. We vary the gas kinetic temperature and gas volume density in order to find combinations that yield results consistent with the measured excitation temperatures in Engelke & Allen (2018).

5.3 Numerical Results

A contour plot of results from the line excitation simulations is displayed in Figure 5.2. We find that the model predicts that $T_{ex}^{65} > T_{ex}^{67}$ for the majority of input parameter combinations, consistent with the results in Engelke & Allen (2018). Thus localized conditions leading to enhanced emission are not necessary to explain the measured difference in the main line excitation temperatures. The modeling does not only indicate that it is normal to find interstellar OH gas with $T_{ex}^{65} > T_{ex}^{67}$, but also allows us to predict the physical conditions in the W5 region where the Engelke & Allen (2018) excitation temperatures were measured. If we can reproduce the values of T_{ex}^{65} and T_{ex}^{67} measured in Engelke & Allen (2018), the input parameters that led to those results are a good estimate of the physical conditions in the region. We assume a line of sight cloud depth of 10^{18} cm (or 0.3 pc). A study varying the kinetic temperature and gas volume density input parameters using molpopCEP suggests that kinetic temperature of the gas is 57 $\pm$0.5 K, and the volume density of molecular gas is 425 $\pm$150 cm^{-3}. There is some uncertainty from the assumed input parameter values as well. As long as reasonable values are used for the assumed input parameters, the effects of on the results should be fairly minimal; the excitation temperatures predicted can change by approximately 0.1 to 0.2 K if the uniform 1.5 K blackbody background is set to zero, for example, which would introduce an uncertainty contribution in volume density of less than 50 cm^{-3} to be added in quadrature to the total uncertainty. The result is negligible on the final uncertainty estimates. One

effect that we have not considered as carefully is the effect of the collisional cross section values themselves on the resulting predictions. In this paper, we use the Offer et al. (1994) collisional cross sections for OH and H_2 collisions. However, newer, more accurate collisional cross section values could potentially affect the results of the line excitation simulation.

5.4 Comparison of Volume Density Predicted by the Two Models

In W5, it is possible to compare the volume densities predicted by the diffuse cloud model (see Chapter 4) to volume densities predicted by the line excitation code molpopCEP. Plotting the measured ΔT_{ex} and results of the line excitation modeling in Figure , we see that the volume density of gas is between 250 cm^{-3} and 575 cm^{-3}, or $\sim 425 \pm 150$ cm^{-3}. The diffuse cloud model gives the volume density parameter in terms of total nuclei of hydrogen, whereas molpopCEP gives the volume density in terms of gas particles. If the gas is primarily composed of molecular hydrogen, then the gas volume density should be approximately half of the density of H nuclei. The volume density of H nuclei in W5 predicted by the diffuse cloud model is 890 ± 130 cm^{-3}. Half of this value is 450 ± 70 cm^{-3}. Thus the molpopCEP density prediction of $\sim 425 \pm 150$ is entirely consistent with the volume densities predicted by the diffuse cloud model using a different set of inputs and assumptions.

5.5 Excitation Temperature Modeling as a Means of Estimating Gas Volume Density

These results suggest that measurements of the excitation temperatures and especially of the difference in main line excitation temperature $\Delta T_{ex} = T_{ex}^{65} - T_{ex}^{67}$ for the OH 18 cm transition could be used as a means to estimate gas volume density. This novel method for estimating gas volume density benefits from the fact that the only observations required are OH 18 cm observations; that is, unlike the diffuse cloud model in the previous chapter, no comparison to CO(1-0) data is required. We therefore have a method for estimating total gas volume density in molecular gas clouds that is applicable to CO-dark molecular gas, as long as OH signals are detected at both main lines.

Figure 5.3 displays ranges of predicted gas volume density as a function of the difference in main line excitation temperature using the molpopCEP code. The results are in the form of ranges rather than exact values because the gas volume density depends on the actual independent values of the excitation temperatures and not just their difference. The results in Figure 5.3 assume a range of possible excitation temperature values between 4 K and 7 K, and if that range were increased, the lengths of the error bars would increase as well. However, although the main line excitation

temperature difference is not sufficient information to exactly predict a single value for the gas column density, Figure 5.3 demonstrates that the main line excitation temperature difference alone does provide useful information about the gas volume density even so. The advantage of using the excitation temperature difference is that the uncertainty on the excitation temperature difference measured with the continuum background method is generally lower than the uncertainties on the individual T_{ex} values (see Chapter 4 for a discussion of the uncertainties involved in determining continuum temperature at 1667 MHz as well as the excitation temperatures derived from that information).

5.6 Future Work

Future studies are made possible by this method. Observing programs could include OH surveys with the Green Bank Telescope targeting star-forming regions and their edges and regions surrounding them, or other similar regions with elevated continuum in the background. The technique is suitable for regions that contain variations in continuum background of approximately 4 - 7 K, since this appears to be the range of excitation temperature values for W5 as well as some lower T_{ex} values such as those reported by Li et al. (2018). A wider range may be appropriate considering that conditions will vary in different regions of the ISM, but values reported by Li et al. (2018) provide a good starting benchmark when choosing observation targets.

Once observations are made, excitation temperatures may be estimated using methods similar to the continuum background method described in Chapter 2 (Engelke & Allen 2019). A good starting point for such a study could be to focus on the excitation temperature differences, rather than the individual excitation temperature values, and to determine the extent to which this information can constrain possible values of volume density of the gas in the region. Longer term future studies could focus on the values of the excitation temperatures themselves, since this provides more constrained estimates of physical conditions. These observations would require a fuller understanding of the continuum behind the gas clouds that is more difficult to obtain.

The line excitation modeling relies on values of collisional cross sections calculated by Offer et al. (1994). Newer calculations are currently in preparation, by a group including Paul Dagdigian and François Lique (private communication). When published, these updated collisional cross sections could be applied to the line excitation modeling, in order to improve the accuracy of the resulting gas volume density estimates.

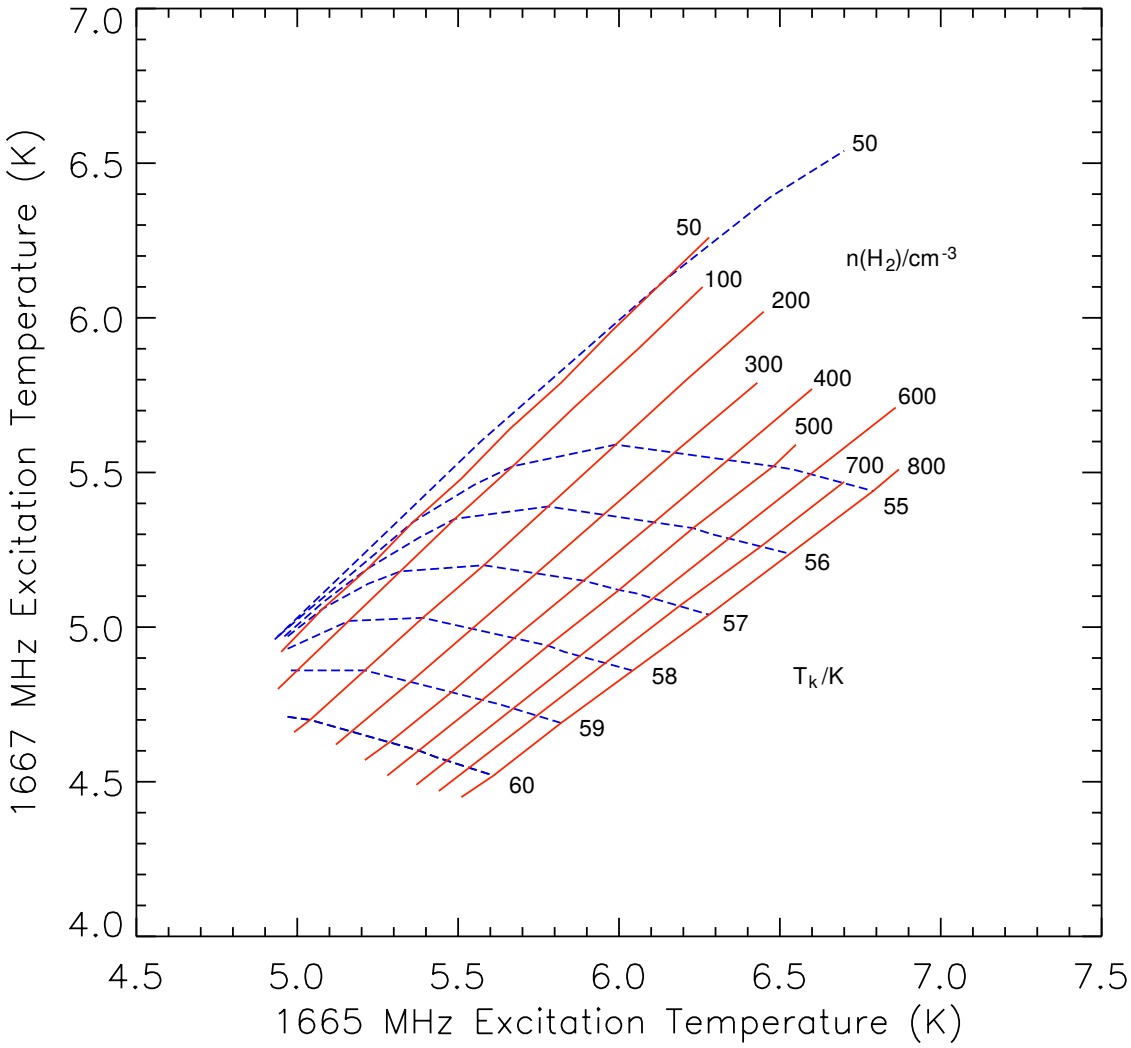

Figure 5.1: Results of the molpopCEP line excitation model for a range of volume density and kinetic temperature inputs, for a set of input parameters chosen for W5. Contours of constant volume density of gas particles are plotted in solid red, and contours of constant kinetic temperature are plotted in dashed blue. The 1665 and 1667 MHz line excitation temperatures are predicted by the code as outputs for the inputs provided; the x and y axes display these values. Input parameters for this run of molpopCEP were line of sight depth r = 1×10^{18} cm, OH abundance n_mol/n =1 $\times 10^{-7}$, velocity width of the slab = 0.1 km/s, diluted blackbody radiation temperature = 1.5 K, dilution factor W = 1, from the left, dust optical depth τ = 0.2, dust temperature = 15 K, set as internal. Changes in these inputs would lead to minor differences in the resulting excitation temperature values, but would be unlikely to change the values by more than order 0.1 to 0.2 K. Nevertheless, that uncertainty could be sufficient to alter the resulting volume density predictions by 200 cm^{-3}.

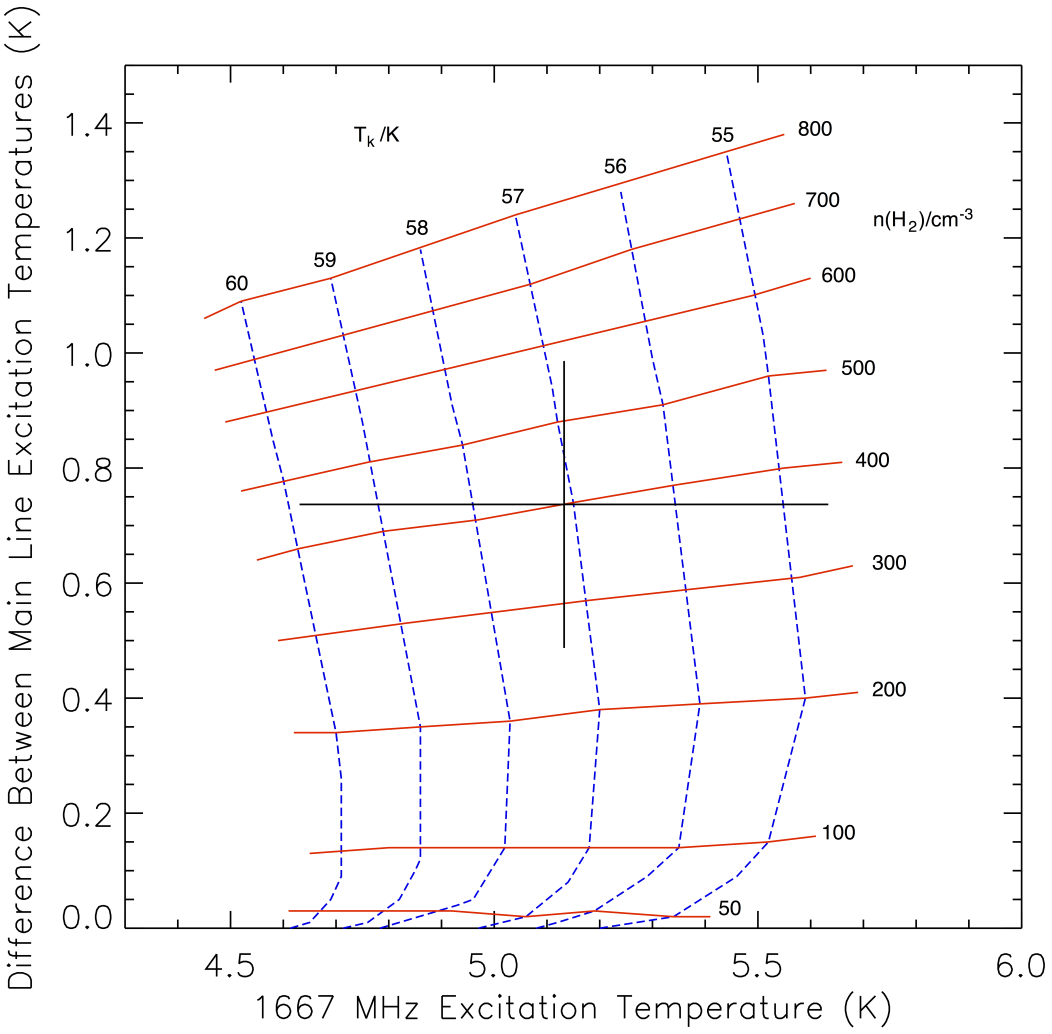

Figure 5.2: The same line excitation model results that are displayed in Figure **??**, but plotted for the main line excitation temperature difference $\Delta T_{ex} = T_{ex}^{65} - T_{ex}^{67}$ as a function of the excitation temperature at 1667 MHz. The measured value of T_{ex}^{67} and ΔT_{ex} is plotted on top of the model results, with error bars indicating the uncertainties assuming ± 0.5 K uncertainty for T_{ex} (see Chapter 4 and ± 0.25 K uncertainty for ΔT_{ex} (Engelke & Allen 2018, 2019). Plotting the model results in this way demonstrates that the contours of constant volume density are close to horizontal, which means that excitation temperature difference correlates fairly well with volume density. As a result, excitation temperature difference, which is easier to measure with higher accuracy than the individual excitation temperatures, could be a good observational indicator for volume density in molecular clouds near star-forming regions.

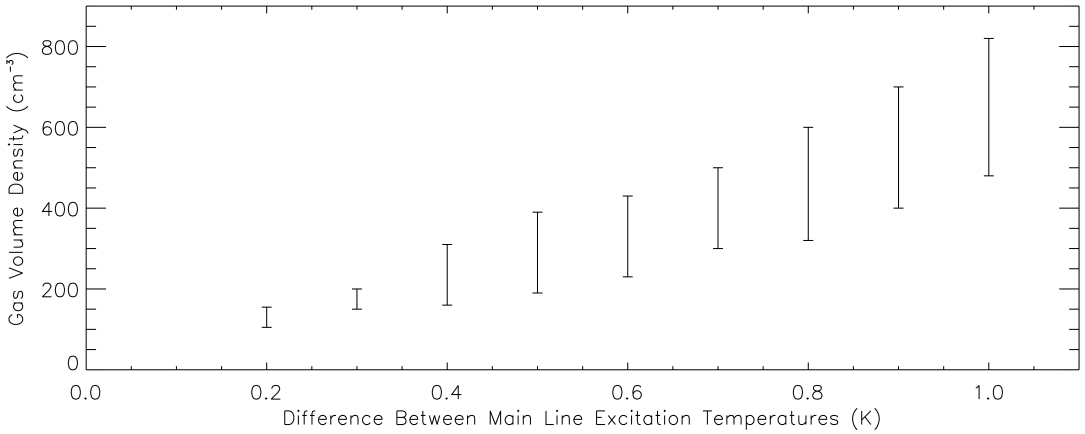

Figure 5.3: Predictions of gas volume density as a function of the difference in main line excitation temperature $\Delta T_{ex} = T_{ex}^{65} - T_{ex}^{67}$ using the molpopCEP code. Since column densities depend on the actual independent values of the main line excitation temperatures and not just on their difference, the error bars incorporate the range of possible values of volume density predicted for the corresponding difference in main line excitation temperatures within a range of 4K $< T_{ex} <$7 K for both main lines. The length of each error bar is dominated by this range of possible values, but also incorporates a minor amount of error resulting from uncertainty in that range of values. If the range of allowed excitation temperature values is expanded, the resulting range of possible predicted volume densities will also increase. However, we note that within some reasonable uncertainties in the exact value of the continuum and thus in the excitation temperature (in this case, a rather large and liberal uncertainty choice of $\pm$ 1.5 K), the continuum background method of observation combined with molpopCEP modeling can be useful as a means of estimating gas volume densities if the difference in main line excitation temperatures is known more accurately than the excitation temperature values themselves.

Chapter 6

Conclusions

Looking at the various results in this work on the whole, some major ideas become apparent. Work on OH as an alternate tracer for molecular gas supports the notion that OH is a viable tracer for molecular gas in the cold, diffuse interstellar medium. Moreover, OH appears to be a good tracer for CO-dark molecular gas. OH traces a larger component of the molecular ISM, while producing results in agreement with the CO distribution in denser regions such as the W5 star-forming region.

One major idea that can be gleaned from our work in W5 and comparison to the quiescent regions is that CO-dark molecular gas can plausibly be explained as a low volume density effect at large scales, in contrast to the view that CO-dark molecular gas is largely the result of chemical depletion of CO at the edges of molecular clouds. While chemical depletion of CO is probably an important effect at small scales on cloud edges and photo-dissociation regions in particular, these situations do not

account for the majority of the volume of the diffuse ISM. In fact, our observations are unable to resolve the size scales in which chemical depletion of CO is likely to occur. As such, the "CO-dim" portions of W5 in the W5 Green Bank Survey in this work might be evidence of chemical depletion of CO at the edges of clouds exposed to UV from O and B stars, which are, naturally, located in a star-forming region. However, all of the CO-dark molecular gas that we found by comparing our OH surveys to CO data occurred in the lowest density portions of the One Square Degree quiescent region, according to the diffuse cloud model, and none of them occurred in the W5 star-forming region. The result that the highest average density occurs in W5, intermediate density occurs in the CO-bright portions of the One Square Degree region, and the lowest density occurs in the CO-dark portions of the One Square Degree region makes a convincing case that lower volume density is correlated with CO-dark molecular gas. We can explain this finding in terms of the emissivity function below and above the critical density. Any future work on CO-dark molecular gas ought to consider the possibility that large reservoirs of CO-dark gas may in fact contain typical abundances of CO, which is simply not being detected as a result of low volume density on its excitation physics.

Another major idea supported by this work is that CO-dark molecular gas is probably located primarily outside of star-forming regions and denser nebulae, in the vast, diffuse interstellar medium. Although additional observations in other star-forming regions would help provide more data support, our results suggest that star-

forming regions such as W5 are already fairly well traced by CO, while quiescent regions are probably generally not traced nearly as thoroughly by CO as is typically assumed. One problem in observational astronomy is that observations tend to be pointed at specific known targets, and this means much of the space in between can be underrepresented in observational data in the literature. CO-dark molecular gas may occur mainly where the volume density of H_2 is low, despite the fact that CO could exist in abundance, rather than in star-forming regions of major nebula. Then there would be a natural bias in favor of observing regions that do not contain the majority of the CO-dark molecular gas. The historical impression that molecular gas is centered in dense clumps and star-forming regions is due in part to sensitivity limitations of old receivers; Turner (1979) reported that OH emission was located mainly in dense clumps, but the sensitivity in that work was an order of magnitude below ours; as such, it is unsurprising that the lower volume density diffuse molecular gas was not detected then. The use of ^{12}CO(1-0) as the molecular gas tracer of choice only cemented that impression, considering that it does not adequately trace the lower volume density molecular gas.

Looking to the future, observations targeting star-forming regions will still be important in order to test the picture of CO-dark molecular gas primarily existing outside of star-forming regions. However, it is even more important that future studies of CO-dark molecular gas include observations in locations that are not known to contain any specific observational targets. Quiescent regions towards the outer Galaxy

provide the best and most fruitful locations for surveys studying CO-dark molecular gas. The outer Galaxy provides conditions more amenable to OH emission surveys than does the inner Galaxy. Elevated continuum temperatures towards the inner Galaxy complicate analysis because OH is detected as absorption lines, which can be unreliable for calculating column densities. Accurate knowledge of T_C and T_{ex} become simultaneously more urgent and more difficult to discern towards the inner Galaxy, and kinematic distances are subject to ambiguity based on models of Galactic rotation. These complications are reduced or avoided in the outer Galaxy. On the other hand, it is still uncertain whether it is best to focus solely on the Galactic plane or if studies at higher and lower Galactic latitudes might be fruitful. Future surveys for OH emission should target a range of Galactic latitudes in order to determine how far above and below the plane OH emission is detected. Matching the range of latitudes to those containing CO detections would be counterproductive, considering the evidence that much of the diffuse, low volume density molecular ISM is CO-dark.

We suggest that the major difference between molecular gas clouds in a star-forming region and those in quiescent regions may have less to do with total quantity and mass of molecular gas, and more to do with density fluctuations within the clouds. Star-forming regions containing shock waves could exhibit regions of higher volume density as well as regions of lower volume density, whereas quiescent regions would contain more uniform volume density straddling the threshold for CO detection. Thus in star-forming regions, the majority of molecular gas would be found in denser

clumps and would be CO-bright, whereas in quiescent regions, some of the more diffuse parts of the cloud could cease to produce strong CO signals as a result of more uniform, generally lower volume densities. In both cases, structure is an important consideration, as is evident in the study of OH absorption and the low OH filling factor implied by comparing absorption and corresponding emission profiles. This hypothesis could be tested with further analysis, including a study focused on velocity dispersion. More observations in additional star-forming and quiescent regions may be needed for a comparative analysis of velocity dispersions, since such a study would require a large sample of OH detections in order to obtain high precision mean and standard deviations of velocity distributions for different types of regions.

Lastly, we propose a method to probe the physical conditions of molecular gas clouds near star-forming regions by measuring the OH 18 cm main line excitation temperatures and implementing a line excitation simulation. This technique warrants further exploration and study, and should be the subject of future work. Future observations could include surveys near the edges of other star-forming regions in order to perform the continuum background method of excitation temperature measurement. The release of updated OH to H_2 collisional cross section values should improve the accuracy of this method. This technique makes possible the study of physical conditions in molecular gas clouds with no reliance on CO observations.

Bibliography

Abdo, A. A., Ackermann, M., Ajello, M. et al. 2010 The Astrophysical Journal 710, 133

Allen, R. J., Atherton, P. D., & Tilanus, R. P. J. 1986 Nature 319, 296

Allen, R. J., Hogg, D. E., & Engelke, P. D. 2015 The Astronomical Journal 149, 123

Allen, R. J., Rodríguez, M. I., Black, J. H., & Booth, R. S. 2012 The Astronomical Journal 143, 97

Allen, R. J., Rodríguez, M. I., Black, J. H., & Booth, R. S. 2013 The Astronomical Journal 145, 85

Anderson, L. D., Bania, T. M., Jackson, J. M. et al. 2009 The Astrophysical Journal Supplement Series 181, 255

Asensio Ramos, A. & Elitzur, M. 2018 Astronomy and Astrophysics 616, A131

Becker, W. & Fenkart, R. 1971 Astronomy and Astrophysics Supplement Series 4, 241

BIBLIOGRAPHY

Bieging, J. H. & Crutcher, R. M. 1986 The Astrophysical Journal 310, 853

Bolatto, A., Wolfire, M., & Leroy, A. 2013 Annual Reviews of Astronomy and Astrophysics 51, 207

Brogan, C. L., Zauderer, B. A., Lazio, T. J. et al. 2005 The Astronomical Journal 130, 698

Busch, M. P., Allen, R. J., Engelke, P. D. et al. 2019 submitted to The Astrophysical Journal

Chauhan, N., Pandey, A. K., Ogura, K. et al. 2009 Monthly Notices of the Royal Astronomical Society 396, 964

Chauhan, N., Pandey, A. K., Ogura, K. et al. 2011 Monthly Notices of the Royal Astronomical Society 415, 1202

Clemens, D. P., Sanders, D. B., & Scoville, N. Z. 1988 The Astrophysical Journal 327, 139

Condon, J. J., Cotton, W. D., Greisen, E. W. et al. 1998 The Astronomical Journal 115, 1693

Crutcher, R. M. 1972 Ph.D. thesis, University of California, Los Angeles

Crutcher, R. M. 1973 The Astrophysical Journal 185, 857

Crutcher, R. M. 1977 The Astrophysical Journal 216, 308

BIBLIOGRAPHY

Crutcher, R. M. 1979 The Astronomical Journal 234, 881

Dame, T. M., Hartmann, D., & Thaddeus, P. 2001 The Astrophysical Journal 547, 729

Dame, T. M., Ungerechts, H., Cohen, R. S. et al. 1987 The Astrophysical Journal 322, 706

Dawson, J. R., Walsh, A. J., Jones, P. A. et al. 2014 Monthly Notices of the Royal Astronomical Society 439, 1596

Deharving, L., Zavagno, A., Anderson, L. D. et al. 2012 Astronomy and Astrophysics 546, A74

Deshpande, A. A. 2000 Monthly Notices of the Royal Astronomical Society 317, 199

Dickey, J. M., Crovisier, J., & Kazes, I. 1981 Astronomy and Astrophysics 98, 271

Draine, B. T. 1978 The Astrophysical Journal Supplement Series 36, 595

Elitzur, M. 1992 *Astronomical Masers Astrophysics and Space Science Library*, volume 170 Dordrecht: Kluwer

Engelke, P. D. & Allen, R. J. 2018 The Astrophysical Journal 858, 57

Engelke, P. D. & Allen, R. J. 2019 The Astrophysical Journal 874, 49

Faison, M. D. & Goss, W. M. 2001 The Astronomical Journal 121, 2706

BIBLIOGRAPHY

Frail, D. A., Wisberg, J. M., Cordes, J. M., & Mathers, C. 1994 The Astrophysical Journal 436, 144

Fürst, E., Reich, W., Reich, P., & Reif, K. 1990 Astronomy and Astrophysics Supplement Series 85, 691

Goss, W. M. 1968a The Astrophysical Journal Supplement Series 15, 131

Goss, W. M. 1968b The Astrophysical Journal Supplement Series 15, 131

Goss, W. M., Kalberla, P. M. W., & Dickel, H. R. 1984 Astronomy and Astrophysics 139, 317

Goss, W. M., Richards, A. M. S., Muxlow, T. W. B., & Thomasson, P. 2008 Monthly Notices of the Royal Astronomical Society 388, 165

Green, G. M., Schlafly, E. F., Finkbeiner, D. et al. 2018 Monthly Notices of the Royal Astronomical Society 478, 651

Gregory, P. C., Scott, W. K., Douglas, K., & Condon, J. J. 1996 The Astrophysical Journal Supplement Series 103, 427

Grenier, I. A., Casandjian, J.-M., & Terrier, R. 2005 Science 307, 1292

Guibert, J., Elitzur, M., & Nguyen-Q-Rieu 1978 Astronomy and Astrophysics 66, 395

Hachisuka, K., Brunthaler, A., Menten, K. M. et al. 2006 The Astrophysical Journal 645, 337

BIBLIOGRAPHY

Haslam, C. G., Salter, C. J., Stoffel, H., & Wilson, W. E. 1982 Astronomy and Astrophysics Supplement Series 47, 1

Heiles, C. E. 1968 The Astrophysical Journal 151, 919

Heiles, C. E. 1969 The Astrophysical Journal 157, 123

Heiles, C. E. & Gordon, M. A. 1975 The Astrophysical Journal 199, 361

Herzberg, G. 1950 *Molecular Spectra and Molecular Structure - Volume I - Spectra of Diatomic Molecules* Princeton: D. Van Nostrand Company, Inc.

Heyer, M. H., Brunt, C., Snell, R. L. et al. 1998 The Astrophysical Journal Supplement Series 115, 241

Higgs, L. A., Landecker, T. L., Asgekar, A. et al. 2005 The Astronomical Journal 129, 2750

Higgs, L. A. & Tapping, K. F. 2000 The Astronomical Journal 120, 2471

Hollenbach, D., Kaufman, M. J., Neufeld, D. et al. 2012 The Astrophysical Journal 754, 22

Karr, J. L. & Martin, P. G. 2003 The Astrophysical Journal 595, 900

Knapp, G. R. & Kerr, F. J. 1972 The Astronomical Journal 77, 649

Langer, W. D., Velusamy, T., Pineda, J. L. et al. 2014 Astronomy and Astrophysics 561A, 122L

BIBLIOGRAPHY

Lee, M.-Y., Stanimirovic, S., Murray, C. E. et al. 2015 The Astrophysical Journal 809, 56

Li, D., Tang, N., Nguyen, H. et al. 2018 The Astrophysical Journal Supplement Series 235, 1L

Liszt, H. & Lucas, R. 1996 Astronomy and Astrophysics 314, 817

Liszt, H. & Lucas, R. 2002 Astronomy and Astrophysics 391, 693

Lockett, P. & Elitzur, M. 2008 The Astrophysical Journal 667, 985

Lockett, P., Gauthier, E., & Elitzur, M. 1999 The Astrophysical Journal 511, 235

Manchester, R. N. & Gordon, M. A. 1971 The Astrophysical Journal 169, 507

Marscher, A. P., Moore, E. M., & Bania, T. M. 1993 The Astrophysical Journal 419, L101

Marsh, K. A., Whitworth, A. P., Lomax, O. et al. 2017 Monthly Notices of the Royal Astronomical Society 471, 2730

Massey, P., Johnson, K. E., & DeGioia-Eastwood, K. 1995 The Astrophysical Journal 454, 151

McGee, R. X., Robinson, B. J., Gardner, F. F., & Bolton, J. G. 1965 Nature 208, 1193

Miville-Deschênes, M.-A. & Lagache, G. 2005 The Astrophysical Journal Supplement Series 157, 302

Moffat, A. F. J. 1972 Astronomy and Astrophysics Supplement Series 7, 355

Moore, E. M. & Marscher, A. P. 1995 The Astrophysical Journal 452, 671

Neufeld, D., Kaufman, M., Goldsmith, P. et al. 2002 The Astrophysical Journal 580, 278

Neufeld, D. A. & Wolfire, M. G. 2016 The Astrophysical Journal 826, 12

Neufeld, D. A. & Wolfire, M. G. 2017 The Astrophysical Journal 845, 15

Nguyen, H., Dawson, J. R., Miville-Deschênes, M.-A. et al. 2018 The Astrophysical Journal 862, 49

Nguyen-Q-Rieu, Winberg, A., Guibert, J. et al. 1976 Astronomy and Astrophysics 46, 413

Nguyen-Q-Riu, Winnberg, A., Guibert, J. et al. 1976 Astronomy and Astrophysics 46, 413

Normandeau, M., Taylor, A. R., & Dewdney, P. E. 1997 The Astrophysical Journal Supplement Series 108, 279

Offer, A., van Hemert, M., & van Dishoeck, E. 1994 Journal of Chemical Physics 100, 362

BIBLIOGRAPHY

Paradis, D., Dobashi, K., Shimoikura, T. et al. 2012 Astronomy and Astrophysics Supplement Series 543, A103

Penzias, A. A. 1964 The Astronomical Journal 69, 146

Pineda, J. L., Langer, W. D., Velusamy, T., & Goldsmith, P. F. 2013 Astronomy and Astrophysics Supplement Series 554, A103

Planck Collaboration, Abergel, A., & Ade, P. A. R. 2014 Astronomy and Astrophysics Supplement Series 571, A11

Reich, P. & Reich, W. 1988 Astronomy and Astrophysics Supplement Series 74, 7

Reich, P., Reich, W., & Fürst, E. 1997 Astronomy and Astrophysics Supplement Series 126, 413

Reid, M. J. & Moran, J. M. 1981 Annual Reviews of Astronomy and Astrophysics 19, 231

Reynoso, E. M. & Goss, W. M. 2002 The Astrophysical Journal 575, 871

Rickard, L. J., Palmer, P., Morris, M. et al. 1975 The Astrophysical Journal Letters 199, L75

Rodríguez, M. I., Wiklind, T., Allen, R. J. et al. 2007 The Astrophysical Journal 663, 824

BIBLIOGRAPHY

Roy, N., Cheugalur, J. N., Dutta, P., & Bharadwaj, S. 2010 Monthly Notices of the Royal Astronomical Society 404, L45

Roy, N., Minter, A. H., Goss, W. M. et al. 2012 The Astrophysical Journal 749, 144

Rugel, M. R., Beuther, H., Bihr, S. et al. 2018 Astronomy and Astrophysics Supplement Series 618, A159

Sanders, D. B., Solomon, P. M., & Scoville, N. Z. 1984 The Astrophysical Journal 276, 182

Scoville, N. Z., Solomon, P. M., & Jefferts, K. B. 1974 The Astrophysical Journal 187, L63

Tang, N., Li, D., Heiles, C. et al. 2016 Astronomy and Astrophysics Supplement Series 593, A42

Tang, N., Li, D., Heiles, C. et al. 2017 The Astrophysical Journal 839, 8

Taylor, A. R., Gibson, S. J., Peracaula, M. et al. 2003 The Astronomical Journal 125, 3145

Tibaldo, L., Digel, S. W., Casandjian, J.-M. et al. 2015 The Astrophysical Journal 807, 161

Townes, C. H. 1957 Proceedings from 4th IAU Symposium, Symposium Number 4, ed. Hendrik Christoffel Van de Hulst, Cambridge University Press page 92

BIBLIOGRAPHY

Townes, C. H. & Schawlow, A. L. 1955 *Microwave Spectroscopy* New York: McGraw-Hill

Turner, B. E. 1973 The Astrophysical Journal 186, 357

Turner, B. E. 1979 Astronomy and Astrophysics Supplement Series 37, 1

Turner, B. E. & Heiles, C. 1971 The Astrophysical Journal 170, 453

Weaver, H., Williams, D. R. W., Dieter, N. H., & Lum, W. T. 1965 Nature 208, 29

Weinreb, S., Barrett, A. H., Meeks, M. L., & Henry, J. C. 1963 Nature 200, 829

Weselak, T., Galazutdinov, G., Beletsky, Y., & Krełowski, J. 2010 Monthly Notices of the Royal Astronomical Society 402, 1991

Wilson, R. W., Jefferts, K. B., & Penzias, A. A. 1970 The Astrophysical Journal 161, L43

Wilson, T., Rohlfs, K., & Hüttemeister, S. 2013 *Tools of Radio Astronomy* Heidelberg: Springer 6 edition

Wolfire, M. G., Hollenbach, D., & McKee, C. F. 2010 The Astrophysical Journal 716, 1191

Xu, D., Li, D., Yue, N., & Goldsmith, P. 2016 The Astrophysical Journal 819, 22

Xu, Y., Reid, M. J., Zheng, X. W. et al. 2006 Science 311, 54

Vita

Philip Engelke was born on December 26, 1990 in Boston, Massachusetts, and graduated from Newton North High School in Newton, Massachusetts in 2009. He received a B.S. degree in intensive physics from Yale University in 2013. In fall 2013, Philip began graduate school at the physics and astronomy department at Johns Hopkins University, where he began his research on OH as an alternate tracer for otherwise-hidden molecular gas in the Galaxy, and received an M.A. degree in physics and astronomy in 2015. Philip was awarded a Grote Reber Fellowship from the National Radio Astronomy Observatory in 2016, providing two years of funding for graduate work at the Domenici Science Operations Center in Socorro, New Mexico. Philip's time in New Mexico lasted from the end of 2016 to the end of 2018, after which he returned to Baltimore to finish his Ph.D. work.